University of Alberta

Buoyancy-driven convection in a ventilated porous medium

by

Mark Andrew Roes

A thesis submitted to the Faculty of Graduate Studies and Research
in partial fulfillment of the requirements for the degree of

Master of Science

Department of Mechanical Engineering

Spring 2014
Edmonton, Alberta

Abstract

Consider an open control volume consisting of a porous medium submerged in a surrounding ambient fluid of density ρ_a. The top and bottom of the control volume allow ambient fluid to enter the porous medium. Saline fluid of density $\rho_s > \rho_a$ is supplied at a constant rate of Q_o near the top of the control volume resulting in a descending plume that migrates downward through the porous medium entraining ambient fluid as it falls. Plume fluid discharges along the lower boundary where it drains into the surrounding external fluid through a series of small fissures of area A. The dense fluid accumulates along the lower boundary until a steady state in which the rate of draining is balanced by the influx from the plume. The resulting lower layer depth is h. The objective of this thesis is to develop a theoretical model to predict h and discuss the comparison of the model against experimental measurements of h.

Acknowledgements

I would like to take this opportunity to specially thank Dr. Morris Flynn for his patience and understanding throughout these past years. His guidance and mentorship have been invaluable influences on shaping me into the graduate I have become. I am proud to call him my mentor, and my friend. As well, I would like to thank Dr. Jerry Leonard for his supervision and experience.

I would like to extend my gratitude to Dr. Lorenz Sigurdson for the temporary accommodation of lab and work space. This thesis would not have been so easily obtainable without his facilities and equipment.

I would like to thank my wonderful, loving and supportive parents, Andy and Sylvia Roes. Through their efforts and sacrifice I have been able to achieve what most only dream of. I love you both very much.

Lastly, I would also like to show appreciation for my family and friends that have been through this experience with me.

Table of Contents

List of Tables

List of Figures

Nomenclature

ND signifies that the variable in question has no units. Units are presented in centrimetre-gram-second (CGS) due to the small length scales of experimental measurements considered in this study and not necessarily the applications described in chapter 1.

A	Exit area of the research box	[cm^2]
A_{slit}	Nozzle exit cross-sectional area	[cm^2]
A^*	Constant used in Cartesian filling box theory	[ND]
$\check{A}$	Constant used in Axisymmetric filling box theory . . .	[ND]
B^*	Constant used in Cartesian filling box theory	[ND]
$\check{B}$	Constant used in Axisymmetric filling box theory . . .	[ND]
b	Lower boundary thickness	[cm]
d	Lower boundary ventilation diameter	[cm]
d_{bead}	Porous medium bead diameter	[cm]
D	Solute diffusivity	[cm^2/s]
F_o	Buoyancy flux	[cm^4/s^3]
g	Acceleration due to gravity	[cm/s^2]
g'	Reduced gravity	[cm/s^2]

$\bar{g}'$	Average reduced gravity	[cm/s^2]
h	Interface height	[cm]
h_f	Height of the fluid in the overhead reservoir	[cm]
h_o	Initial interface height	[cm]
H	Total height of the research box	[cm]
k	Porous medium permeability	[cm^2]
k_f	Fissure permeability	[cm^2]
m	Best fit slope from equation 4.1	[ND]
m_c	Flow meter calibration: mass of the plastic bottle	[g]
m_t	Flow meter calibration: mass of the saline fluid and plastic bottle	[g]
M	Number of one-hole stoppers	[ND]
M^*	Momentum flux	[cm^4/s^2]
P	Fluid pressure	[g/cm-s^2]
Q	Volume flux of the plume	[cm^3/s]
Q_o	Source volume flux	[cm^3/s]
Q_{out}	Volume flux of the exiting fluid from the control volume	[cm^3/s]
$\dot{Q}_c$	Flow meter calibration volumetric flow rate	[cm^3/s]
r	Radial coordinate	[cm]
S	Solute concentration	[g/cm^3]
t	Time measured during draining flow experiments	[s]
t_c	Flow meter calibration: time interval	[s]

u	Vertical component of velocity	[cm/s]
u_r	Radial component of velocity	[cm/s]
v	Horizontal component of velocity	[cm/s]
W	Width of the research box	[cm]
x	Vertical coordinate	[cm]
x_o	Source term	[cm]
y	Horizontal coordinate	[cm]
Ra	Rayleigh number	[ND]
Re	Reynolds number	[ND]
β	Solute contraction coefficient	[cm^3/g]
Λ	Depth of the research box	[cm]
ϕ	Void fraction	[ND]
ρ	Density	[g/ cm^3]
ρ_a	Ambient density	[g/ cm^3]
ρ_s	Saline density	[g/ cm^3]
ρ_c	Flow meter calibration: saline density	[g/ cm^3]
η	Self-similar solution dependent variable	[ND]
ν	Kinematic viscosity	[cm^2/s]
ψ	Line source theory stream-function	[cm^2/s]
ψ_s	Point source theory stream-function	[cm^2/s]
ξ	Non-dimensional interface height	[ND]
τ	Draining	[ND]

Chapter 1

Introduction

1.1 Literature review

Understanding convection in porous media has been an area of fundamental and applied interest for many decades. This topic has been extensively investigated by many previous researchers such as Wooding (1963), Bear (1972), Scheidegger (1974), Bejan (1978) and Nield and Bejan (1992). Many variations of geometry, such as Cartesian and axisymmetric, and thermal forcing have been considered. When describing fluid flow through a porous medium, the seminal study was that presented by Darcy (1856) in which he concluded, that at low Reynolds number, the fluid velocity through a porous medium is linearly dependent on the permeability, which, as a measure of the ease with which fluid may pass through the medium in question, strongly depends on the geometric parameters such as average grain size. As with any porous media flow, convection is restricted by the fluid having to squeeze through narrow pores in which viscous effects play an important role.

Wooding (1963) studied steady vertical convection from a source of buoyancy in a saturated porous medium at high Rayleigh numbers. More

specifically he investigated a vertical two-dimensional Boussinesq flow in a homogenous porous medium resulting from a horizontal line source of heat at steady state. Boussinesq flow is where density differences are sufficiently small to be neglected everywhere except where density terms are multiplied by gravity. In this configuration Wooding (1962) determined that the governing equations were identical to those describing a plane laminar, though high Reynolds number, incompressible jet as presented by Schlichting (1933). According to Wooding's formulation, the Rayleigh number, Ra, is defined by

$$Ra = \frac{kg\beta(T - T_0)}{\nu\alpha} L\,, \tag{1.1}$$

where k the is permeability of the porous medium, g is the acceleration due to gravity, β is the thermal expansion coefficient, v is the kinematic viscosity of the fluid, α is the effective diffusivity of the fluid, T is the temperature of the fluid, T_0 is the temperature of the source and L is a vertical length scale. The Rayleigh number is the product of two non-dimensional numbers: the Grashof number and the Prandtl number. The resulting non-dimensional Rayleigh number is the ratio of buoyancy and viscosity forces multiplied by the ratio of momentum and thermal diffusivities. The Reynolds number is the ratio of inertial forces to viscous forces. The magnitude of Ra dictates the kind of convective regime that will arise in much the same way that the Reynolds number, Re, gives an indication of whether a prescribed flow will be laminar or turbulent.

A notable review of convection in porous medium is given by Nield and Bejan (1992). Among other ideas, they investigated sources of buoyancy, or heat, and the role that the source geometry has on the

subsequent evolution of the flow. More specifically, they examined two source geometries; a line source and a point source. Relationships for the streamfunction and the temperature distribution were given. From the streamfunction, relationships for the vertical and horizontal velocity field were solved for and presented as functions of vertical and horizontal position, kinematic heat flux and permeability. Nield and Bejan (1992) also report on double diffusive convection, where both density gradients and temperature gradients contribute to the overall buoyancy flux of a fluid in a porous medium. However, this thesis only considers single diffusive convection in which the buoyancy associated with temperature variations are assumed negligible because the system is isothermal.

A more general dynamical investigation of flow and reactions in permeable media is presented by Phillips (1991). Among many other topics, he considers draining flows that arise along the impermeable boundary of a porous medium. More specifically, he discusses hydraulically driven flow in a porous medium where the transport velocity of the flow can be expressed in terms of the (finite) hydraulic head difference, the aquifer length and the permeability of the porous medium in the direction of fluid flow. As we shall soon demonstrate, this line of inquiry can be adapted to the present study because the flows to be investigated here are likewise driven by density differences.

Investigations of the draining of viscous gravity currents have been presented by Acton et al. (2001), Pritchard et al. (2001) and Pritchard and Hogg (2002). They investigated viscous gravity currents propagating laterally over a permeable lower boundary. Acton et al. (2001) and Pritchard et al. (2001) presented similar expressions for the draining velocity through the boundary although Pritchard et al. (2001) assumed

that the lower boundary depth is much less than the height of the gravity current. As a result, the hydrostatic head of the fluid inside the lower boundary is neglected. Acton et al. (2001) note that the height of the draining gravity current can be expressed as

$$h = h_o e^{-(t/\tau)}, \tag{1.2}$$

where h is the height of the gravity current, h_o is the initial height of the gravity current, τ is a suitable time scale and t is time.

The above analysis was extended by Neufeld et al. (2009) who studied theoretically and experimentally the effect of a fissure on the storage capacity of a porous medium. In their study, a saturated semi-infinite porous medium was bounded from below by a horizontal impermeable layer of finite depth that contains a single line sink representing an isolated fissure (figure 1-1). The sink lies at some finite horizontal distance from the point of injection of a dense fluid, which flows as a gravity current along the base of the porous medium. Neufeld et al. (2009) give a relationship for the vertical Darcy velocity within the fissure from which a leakage flux was determined. Similar follow-up studies were performed by Vella et al. (2011) and Neufeld et al. (2011) in which they respectively consider line and point sinks, however these later studies do not consider the lower boundary depth when estimating the hydrostatic pressure of the dense fluid.

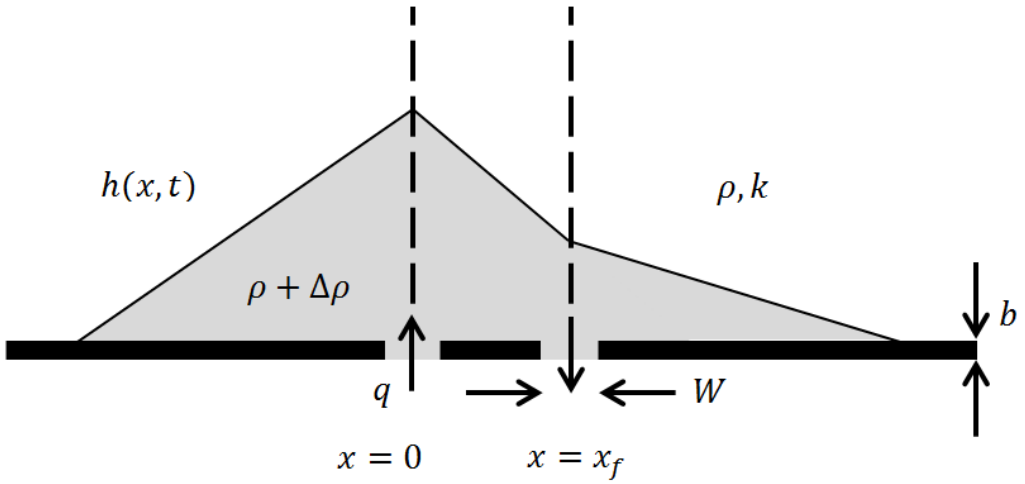

Figure 1-1: Gravity current of density $\rho + \Delta\rho$ supplied at a rate of q into a saturated porous medium of ambient fluid density ρ and permeability k. The fluid creates a gravity current of height h that is dependent on the lateral coordinate x and time t. The fluid drains through a semi-infinite fissure of width W and height b that is positioned at a finite distance x_f from the source. Image adapted from Neufeld et al. (2009).

Following the studies of Acton et al. (2001) and Pritchard et al. (2001), Vella et al. (2011) and Neufeld et al. (2011), we model the fluid velocity inside the leaky fissure v_f as

$$v_f = \frac{k_f}{\mu}\frac{\Delta\rho g(h+b)}{b}, \tag{1.3}$$

where μ is the dynamic viscosity of the fluid, $\Delta\rho$ is the density difference between the dense fluid entering the aquifer and that already present, b is the lower boundary depth, g is the acceleration due to gravity and k_f is the fissure permeability. In their study, Neufeld et al. (2009) measured k_f and made a comparison with Happel and Brenner's (1965) expression for k_f corresponding to a rectilinear fissure geometry. Happel and Brenner's (1965) formula can, incidentally, be derived directly from Darcy's Law, an approach that was earlier applied (for simpler geometries) by Bear (1972) and Scheidegger (1974). When investigating derivations of Darcy's law,

Bear (1972) and Scheidegger (1974) presented capillary models in which they considered bundles of straight, parallel capillaries of uniform diameter and developed a relationship for permeability in terms of capillary diameter. By relating the capillaries to fissures in an otherwise impermeable horizontal boundary, Bear's and Scheidegger's capillary model thereby gave a method for expressing the fissure permeability in terms of the fissure diameter, d, and porosity, ϕ. This capillary model thereby presented a method to express the fissure permeability in terms of the tube diameter d and the porosity ϕ.

Our study mimicked that of Neufeld et al. (2009) except that our source was located above the fissure (figure 1-1). Thus before the source fluid reaches the lower boundary of the porous medium, it forms a vertically descending plume that entrains outside ambient fluid which leads to an increase of plume volume flux in the direction of flow. A not dissimilar investigation, but devoid of a porous medium, was conducted by Linden et al. (1990) who examined the natural displacement ventilation of an open control volume. The experimental and theoretical study was divided into two complementary parts. First, Linden et al. (1990) studied the draining flow of a ventilated control volume initially at a uniform density. Due to hydrostatic forces, dense fluid flowed through the lower opening to be replaced by an equal volume of ambient fluid from outside the control volume which entered through the upper opening. An interface between the light and dense layers was thereby formed that progressively descended over time. The rate of descent of the interface decreased as the interface neared the bottom of the control volume. Linden et al. (1990) also investigated a "filling box" scenario, see figure 1-2, consisting of a

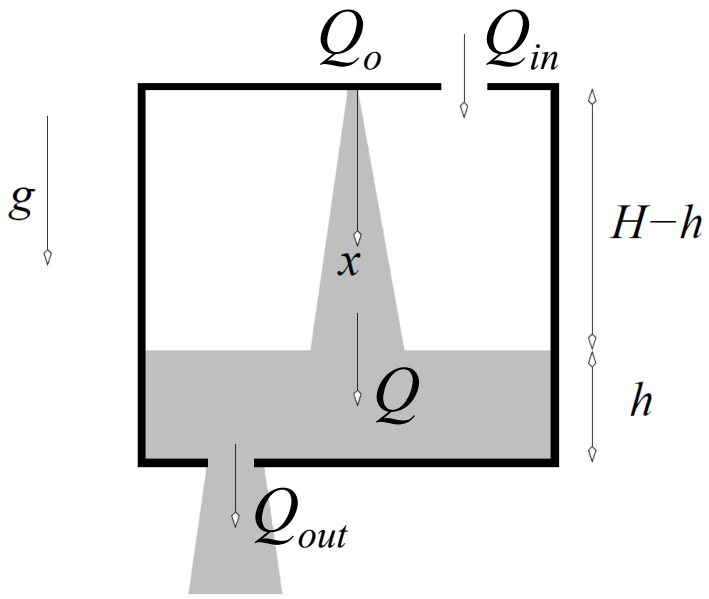

Figure 1-2: A ventilated filling box devoid of porous media.

ventilated control volume with openings again at the top and bottom of the box. Dense fluid was supplied through a nozzle of small cross sectional area at the top of the control volume which resulted in a descending turbulent plume that entrained external ambient fluid through engulfment as it fell. The openings along the top allowed fresh ambient fluid to enter the control volume to replenish the fluid entrained into the plume. The plume fluid migrated downward, collected along the lower boundary and continued to drain through the openings. Separating this dense fluid from the lighter ambient layer above was a sharp interface that moved upwards as more and more fluid was discharged by the plume along the lower boundary. At some critical vertical distance from the bottom boundary the volume flux of the fluid crossing the interface became equal to the volume flux of the dense fluid draining from the bottom of the volume. At this point, the interface elevation became independent of time, t.

As we shall see, many of the same qualitative features observed by Linden et al. also arise when the control volume contains a porous medium, however, important differences also exist, which we will elucidate in the pages below.

1.2 Applications

Convection in porous media can be seen in natural and industrial processes. Three notable examples are carbon sequestration, aerobic composting and grain aeration. These examples are considered below.

Subterranean carbon sequestration is the process by which supercritical carbon dioxide (sc-CO_2) is injected and stored in geological formations deep underground. The formations typically consist of aquifers or depleted oil and gas reservoirs. In the former case, the supercritical carbon dioxide is injected into the bottom of the aquifer, buoyant forces between the heavier brine, occupying the aquifer, and the lighter sc-CO_2 will result in a vertically-rising plume, as illustrated schematically in figure 1-3. This is the process by which the sc-CO_2 ascends through the porous rock, encountering areas of high and low permeability and which results in a local accumulation of sc-CO_2. Once the sc-CO_2 reaches a leaky horizontal boundary, it will begin to drain through the fissure. The volume flux through the fissure will be much less than the volume flux of the fluid reaching the boundary. Here, the sc-CO_2 will continue to accumulate until the hydrostatic force associated with the buoyant sc-CO_2 is counterbalanced by the drag force associated with the flow through the narrow fissure(s). An ideal aquifer is one that does not contain any fissures and is lined with highly impermeable rock, or cap rock, which prevents (or

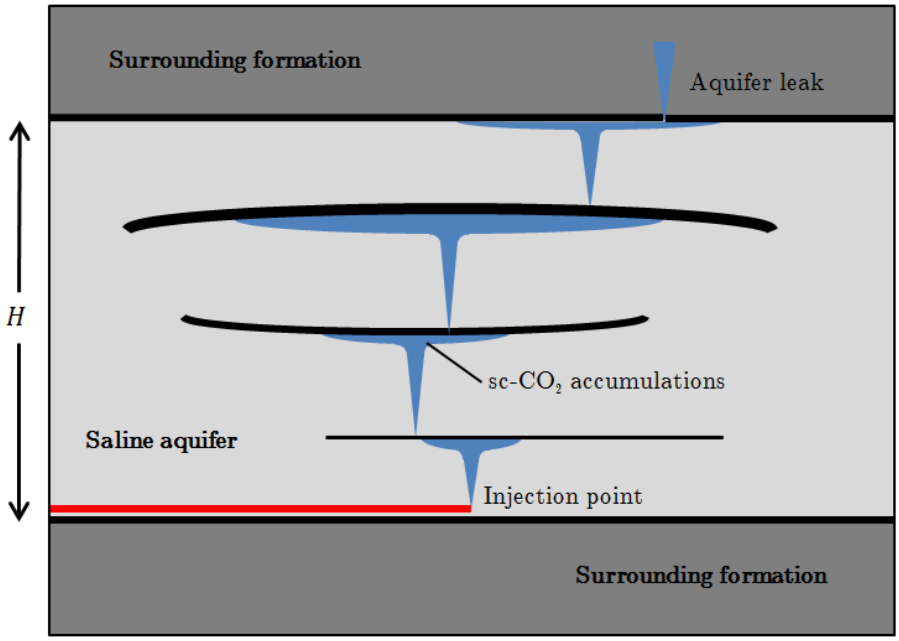

Figure 1-3: An ascending plume of sc-CO_2 through various geological strata.

so we hope) migration of sc-CO_2 to shallower formations. In this respect, aquifers are generally preferable to depleted reservoirs: Neuman and Witherspoon (1967) note that the cap rock surrounding an aquifer generally has a lower permeability than that of the cap rock surrounding an oil reservoir, and offers more resistance to the migration of sc-CO_2.

A major concern for private and government projects is assessing seal integrity. Neuman and Witherspoon (1967) studied experimental and analytical methods of evaluating the permeability of a slightly leaky cap rock with an infinite thickness. Wolff (1970) subsequently investigated the hydraulic diffusivity of a conforming bed and more recently Rowe and Nadarahah (1993) studied the hydraulic conductivity of aquitards. An aquitard is a zone that restricts groundwater flow from one aquifer to another. An application of the results presented in this thesis could be to estimate the draining and residence timescales of sc-CO_2 and compare them against timescales associated with dissolution and mineralization. A

prediction can then be made about the total volume for sc-CO_2 that will be permanently stored. In like fashion, the variation of the draining timescale with e.g. the injection flux into the aquifer can be estimated based on an extension of the ideas described below. Further understanding of the timescales of draining of sc-CO_2 from a leaky aquifer could prove beneficial when evaluating long term storage options and the risks with these options.

Aerobic composting consists of the exothermic microbial oxidation of the carbon within household and municipal wastes. The efficiency of the oxidation process is affected by parameters such as temperature, O_2 and CO_2 concentration and moisture content. The heat produced by chemical reactions will be more easily transferred to water molecules because water has a higher thermal conductivity than most of the other materials in the compost pile (Ahn et al. 2009). Thus a lower moisture content can cause larger temperature fluctuations of the compost pile. This can lead to adverse effects such as a reduction of a microorganism's ability to break down organic material. Trautmann (1996) suggests an optimum moisture content of $50 - 60\%$ because microbial decomposition will occur fastest in the thin liquid layers on the surface of the organic particles. A moisture content that exceeds 65% can reduce decomposition efficiency and increase odor production. Conversely moisture content below 30% can inhibit bacterial activity. Trautmann (1996) argues that decomposition will occur most rapidly in the thermophilic stage, where a temperature range of 40˚C to 60˚C is desired. Temperatures below this desired range will not destroy unwanted thermo-sensitive pathogens and other harmful bodies so that the resulting compost material will fail to meet regulatory standards. On the

other hand, temperatures that exceed the desired range will create an inhospitable environment such that beneficial microorganisms cannot survive. By definition O_2 is necessary for the respiration and metabolism of aerobic microorganisms. Should the O_2 concentration decrease and the CO_2 concentration increase, unwanted anaerobic activity can develop. Compost piles are often mechanically agitated or "turned over" to minimize the likelihood of initiating such anaerobic activity. When the temperature deviates from its peak value of 60˚C, it can be assumed that the oxygen concentration near the center of the pile is low enough to cause adverse effects. The compost material that is exposed to a peripheral boundary will be cooled by free and forced convection and may be less advanced in the composting cycle than material near the center. Mechanical turning helps to keep the compost pile at uniform temperatures and O_2 concentrations, however, near the center the effect of cooling from the exposed surface is comparatively small. As the microorganisms break down the organic material they consume O_2, release CO_2 and generate heat. The air within the compost pile, that contains high concentrations of CO_2, becomes warm and ascends through the compost pile (see figure 1-4). As the warm air rises, cool air from the peripheral boundary must replace it in a process known as displacement ventilation. It should be noted that O_2, CO_2 and heat are transported by both conduction and convection. However, due to the low thermal conductivity of soil and organic material, it can be assumed that convection will be the dominant mechanism of transport. Understanding the convection that occurs in the porous compost pile can help maintain desired temperature, moisture content and O_2 concentration; as well as limit the accumulation of CO_2 concentration as organic materials are broken down. Additionally, the size and shape of the

compost pile can be optimized to help maximize the efficiency of the decomposition cycle.

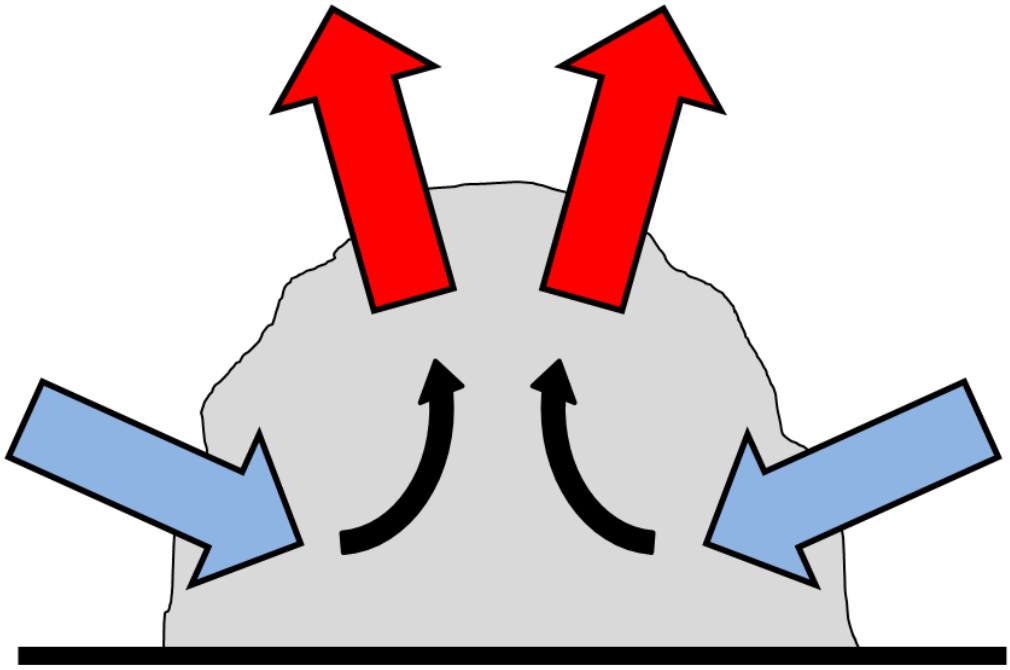

Figure 1-4: Internal convection in a compost pile. Heat generation in the compost pile warms the air in the pile and the buoyant air (red arrows) exits through the top of the pile. Cool, heavier air (blue arrows) enters the pile and replaces the air lost through the top.

Grain aeration is the process of moving air through a volume of stored grain to control temperature and moisture content and, by extension, the rate of spoilage, which is primarily due to insect activity and mold growth (Cloud and Morey 1991). When grain is stored, convection currents can develop and cause moisture condensation and areas of high and low temperature (Canadian Grain Commission 2013). A large temperature differential can cause stronger convection resulting in a greater effect of heating and condensation on the grain. Areas of higher temperatures promote spoilage while areas of high moisture content promote fungal growth which attracts insect infestations (Canadian Grain Commission 2013). A uniform temperature and moisture content are

achieved with the help of large perforated ducts placed beneath the stored grain that carry large volumes of air. During the fall and winter months when the ambient temperature is lower than that of the grain storages, maintaining a uniformly warm temperature throughout the stored grain can additionally protect the grain from frostbite and insect growth. The Canadian Grain Commission (2013) notes that to reduce fungal growth and prevent insect pest problems during fall storage, the temperature and moisture content must be below 18˚C and 14.5%, respectively. Results from this thesis might be extended to encompass grain aeration in which the ambient air temperature surrounding the grain storage is colder than of the grain temperature. The ducts beneath the stored grain provide warmer, lighter air and act as a line source of buoyancy. Plumes of warm air will ascend through the grain entraining cool air creating internal convection and maintaining optimal temperature and moisture content of the stored grain. Proper temperature control can help minimize losses within the grain storage. By applying the plume flux, Q, and reduced gravity, g', equations presented in §2, a better understanding of the plume can help optimize the configuration of ducts and maximize the volume of grain that can achieve optimal temperature and moisture content.

1.3 Present contribution

The objective of this thesis is to develop a model that would estimate the interface height h for a filling box flow scenario and compare the theoretical predictions against the experimental data that was collected. The research presented in this thesis is a fundamental study to better understand buoyant convection in a porous medium. When

considering the experimental design and development of theory in this thesis, Linden et al. (1990) was a major influence. However, there are many differences between experiments presented by Linden et al (1990) and our experiments. The focus here is on the addition of a homogeneous porous medium inside the ventilated control volume; this porous medium is absent in Linden et al.'s study. Additionally, the descending plume is laminar because the characteristic length scale, that is applied in defining the Reynolds number,

$$Re = fluid\ velocity * element\ diameter / kinematic\ viscosity\ ,$$

is consistent with the diameter of the individual elements comprising the porous medium. In general, this diameter is quite small. Consistent with our earlier remarks, the porous material reduces much of the chaotic mixing that would otherwise be associated with the descending plume. Also, the ambient stratification evolves more slowly than in the case of the free plume. Similar to the study of Linden et al. (1990), mass and buoyancy conservation can be applied to determine the steady state elevation, h, of the interface that separates the lower (dense) and upper (buoyant) layers. Here the dense lower layer consists of discharged plume fluid that has not yet drained from the control volume. The purpose of this study was to investigate the behavior of the interface height of the ventilated control volume when a porous medium is present and apply results discussed by Schlichting (1933), Wooding (1962), Linden et al (1990), Phillips (1991) and Nield and Bejan (1992) to characterize the variation of h with the outlet area A, total control volume height H, ambient density ρ_a, saline density ρ_s, source volume flux Q_o and porosity φ. In so doing, and consistent with the previous discussion, we hope to be

able to add valuable insight to the flow patterns of buoyant plumes discussed in the previous examples. Ultimately, then, this thesis is a fundamental study that is meant to lend generic insights that may be applied in a multifaceted way.

1.4 Thesis organization

Chapter 2 of this thesis explains the development of theory to estimate h as a function of various parameters. Chapter 3 describes the experimental instruments used and the experimental procedures followed to verify the theory. The post-processing algorithm required to analyze experimental images for this research is discussed in detail in chapter 4. Chapter 5 examines experimental results obtained from various draining flow experiments and filling box experiments. The theory from chapter 2 is compared with relevant filling box experiments and the similarities and differences are highlighted. Finally, in chapter 6 a series of conclusions are drawn and related to the applications discussed in chapter 1. Ideas for future work and present thoughts and ideas for subsequent research in this area are also presented.

Chapter 2

Theory

2.1 Filling box scenario

We begin by considering the motion of a negatively-buoyant line plume, of buoyancy flux F_o in an unbounded porous medium. The coordinate axes are oriented as in figure 2-1a, which indicates that the plume originates from an infinitesimally thin source. The flow is assumed to be Boussinesq so that density differences may be omitted except where they multiply gravitational acceleration. Likewise, the fluid dynamics of negative and positive sources of buoyancy will be similar. Accordingly, the governing equations encompass mass continuity, conservation of momentum in two directions, solute transport and a linear equation of state. They read

$$\frac{\partial u}{\partial x}+\frac{\partial v}{\partial y}=0, \tag{2.1}$$

$$\frac{1}{\rho_a}\frac{\partial P}{\partial x}+\frac{\nu}{k}u=\frac{g\rho}{\rho_a}, \tag{2.2}$$

$$\frac{1}{\rho_a}\frac{\partial P}{\partial y}+\frac{\nu}{k}v=0, \tag{2.3}$$

$$\left(u\frac{\partial S}{\partial x}+v\frac{\partial S}{\partial y}\right)=D\phi\left(\frac{\partial^2 S}{\partial x^2}+\frac{\partial^2 S}{\partial y^2}\right), \tag{2.4}$$

$$\rho=\rho_a(1+\beta S). \tag{2.5}$$

In the above equations, P is the fluid pressure, $\boldsymbol{u}=(u,v)$ is the transport velocity, ϕ is the void fraction, ν is the kinetmatic viscosity, S is the solute concentration, D is the solute diffusivity, β is the solute contraction coefficient, k is the permeability and ρ_a is the density of the ambient fluid. In (2.4), the porosity ϕ is required since molecular transport can only occur within the saturating fluid and not the porous medium. In computing the permeability k, we use the following relation suggested by Rumpf and Gupte (1971):

$$k=\frac{1}{5.6}d^2\phi^{5.5}. \tag{2.6}$$

where d denotes the mean diameter of the solid particles comprising the porous medium – see (3.2) of Acton et al. (2001). Moreover, ρ is the fluid density; when, as in the far-field the fluid does not contain any solute, $\rho=\rho_a$. When considering a thermal system, (2.4) is easily related to the equation of conservation of energy, or the heat equation. Here, (2.4) considers solute transport by advection (left hand side) and molecular transport, or diffusion (right hand side). Comparatively, the heat equation considers the heat transfer by convection and conduction.

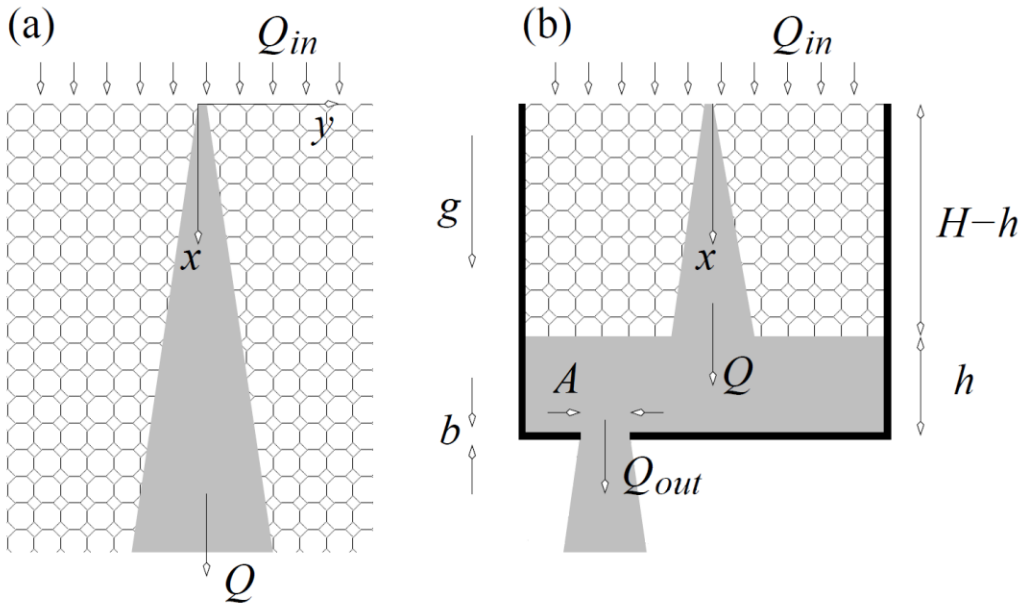

Figure 2-1: (a) Schematic of a two-dimensional Cartesian plume falling through an unbounded porous medium. (b) A ventilated filling box containing a negatively-buoyant plume in a "leaky" porous medium. The control volume height and width are H and W, respectively, where the control volume refers to the region enclosed by the thick solid lines.

Following the discussion of Phillips (1991), self-similar solutions to (2.1-2.5) are sought that respect the following boundary layer approximation such that variables change more significantly in the transverse direction than the longitudinal direction.

$$\left|\frac{\partial u}{\partial y}\right| \gg \left|\frac{\partial v}{\partial x}\right|, \qquad \text{and} \qquad \left|\frac{\partial^2 S}{\partial y^2}\right| \gg \left|\frac{\partial^2 S}{\partial x^2}\right|.$$

After some algebra, summarized in Appendix E.1†, it can be shown that the plume volume flux satisfies

$$Q = \left(\frac{36 D \phi F_o k x \Lambda^2}{\nu}\right)^{1/3}, \tag{2.7}$$

where Λ is the depth the line source extends into the page. Laminar entrainment into the plume causes the plume volume flux to increase

†: Material in Appendix E.1 follows Phillips (1991) discussion where material presented here follows from a non-trivial extension of Appendix E.1.

(relatively weakly) with depth as $x^{1/3}$. The entrainment leads to a corresponding dilution of the plume fluid; defining $g' \equiv F_o/Q$ as the average reduced gravity of the plume fluid at a particular elevation we find

$$g' = \left(\frac{F_o^2 \nu}{36 D \phi k x \Lambda^2}\right)^{1/3}. \tag{2.8}$$

In like fashion, it can be shown that the momentum flux, M^*, does not vary with the vertical coordinate, i.e. $M^* = F_o k/\nu$. Defining the mean vertical velocity, $\bar{u}$, as $\bar{u} = M^*/Q$ allows one to compute the Reynolds number, $Re = \bar{u} d_{bead}/\nu$, as a function of x. More specifically,

$$Re = \frac{d_{bead}}{\nu (36 D\phi)^{1/3}} \left(\frac{F_o k}{\nu \Lambda}\right)^{2/3} \frac{1}{x^{1/3}}. \tag{2.9}$$

As a plume descends through the porous medium, it entrains ambient fluid. Because of this, the volume flux, Q, of the plume increases as the vertical distance from the source increases. As ambient fluid is entrained into the plume, the reduced gravity of the plume decreases as does the plume's center velocity. The parameters Q and g' are modeled using (2.7) and (2.8) respectively. An estimate for Q, and g' can be made over the entire depth of the control volume which is shown in figure 2-2. The vertical-axis represents the non-dimensional distance from the source, 0 being the source and -1 being the bottom of the control volume. It is shown that there is an initial sharp decrease in g' and a sharp increase in Q over the first 20% of the total height and comparatively a gradual decrease thereafter.

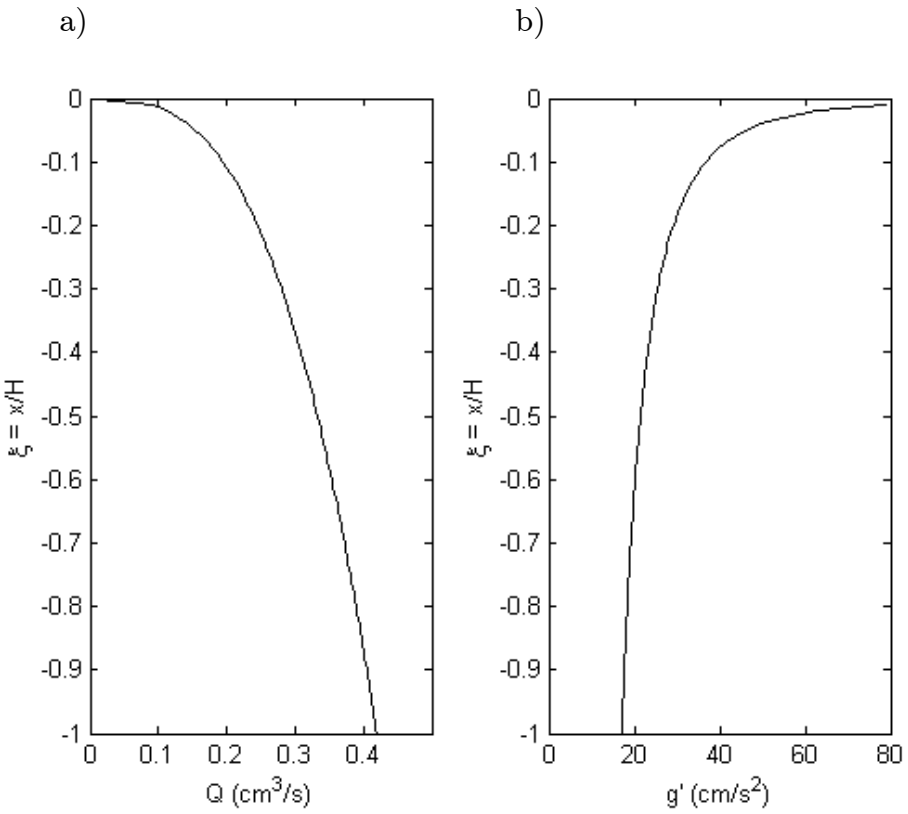

Figure 2-2: The effect entrainment of ambient fluid into the descending plume has on the volume flux, Q and the reduced gravity, g'. Here, as the plume falls: a) Q increases due to the entrained fluid which adds to the total amount of volume fluid in the plume; b) g' decreases because the entrained fluid density is less than the plume density.

Whereas the previous analysis makes no reference to lateral boundaries, it is of interest to examine the draining flow that develops when the negatively-buoyant plume is placed inside a fixed control volume, say of height H and width W. As shown by figure 2-1b, we consider a ventilated (or "leaky") control volume so that solute-bearing fluid may slowly drain through one or more discrete fissure(s) that appear along the bottom boundary of the control volume.

In this preliminary investigation, we consider steady conditions whereby $dh/dt = 0$ in which h is defined as in figure 2-1b. When $dh/dt = 0$, the volume fluxes Q_{in}, $Q|_{H-h}$ and Q_{out} must be equal where the latter is given by

$$Q_{out} = \frac{Ak_f \bar{g}'|_{H-h}}{\nu}\left(\frac{h+b}{b}\right), \tag{2.10}$$

(c.f. equation 2.1 of Neufeld, Vella and Huppert 2009 – see also Pritchard and Hogg 2002). Here k_f and b denote, respectively, the fissure permeability and lower boundary thickness. Conversely A denotes the fissure cross-sectional area. Finally $\bar{g}'|_{H-h}$ is determined from (2.8), i.e.

$$\bar{g}'|_{H-h} = \left[\frac{F_o^2 \nu}{36D\phi k(H-h)\Lambda^2}\right]^{1/3}. \tag{2.11}$$

Equating $Q|_{H-h}$ from (2.7) with Q_{out} from (2.10) indicates that

$$\left[\frac{36D\phi F_o k(H-h)\Lambda^2}{\nu}\right]^{1/3} = \frac{Ak_f}{\nu}\left(\frac{h+b}{b}\right)\left[\frac{F_o^2\nu}{36D\phi k(H-h)\Lambda^2}\right]^{1/3}. \tag{2.12}$$

Rearranging this result yields a cubic polynomial equation that must be solved for the interface height, $h = \xi H$, i.e.

$$\begin{aligned} 0 = {} & \left(\frac{A}{\Lambda b}\right)^3\left(\frac{k_f}{k}\right)^3\xi^3 + \left[\frac{3b}{H}\left(\frac{A}{\Lambda b}\right)^3\left(\frac{k_f}{k}\right)^3 - \frac{1}{Ra}\right]\xi^2 \\ & + \left[3\left(\frac{b}{H}\right)^2\left(\frac{A}{\Lambda b}\right)^3\left(\frac{k_f}{k}\right)^3 + \frac{2}{Ra}\right]\xi \\ & + \left(\frac{b}{H}\right)^3\left(\frac{A}{\Lambda b}\right)^3\left(\frac{k_f}{k}\right)^3 - \frac{1}{Ra}, \end{aligned} \tag{2.13}$$

where the Rayleigh number, Ra, is defined by

$$Ra = \frac{F_o k H}{(36D\phi)^2 \Lambda \nu}, \tag{2.14}$$

(c.f. Phillips 1991, equation 7.5.25). Note that, consistent with the related analysis of Linden et al. (1990), the lower layer depth is predicted to be independent of the width, W, of the filling box.

The above equations, and indeed the similarity solutions of (E.4), presume an ideal source with vanishingly small volume flux at the origin, $x = 0$. When this assumption cannot be justified i.e. the source volume flux, $Q_o > 0$, (2.7) must be modified by writing

$$Q = \left(\frac{36D\phi F_o k(x + x_o)\Lambda^2}{\nu}\right)^{1/3}, \tag{2.15}$$

where x_o is a length scale defined so that Q at $x = 0$ is equal to Q_o. We consider x_o to be a source term and is defined as

$$x_o = \frac{Q_o^3 \nu}{36D\phi F_o k\Lambda^2}. \tag{2.16}$$

Here Q_o is the source volume flux. In like fashion, the density of the lower layer comes from solving

$$\bar{g}'|_{H-h} = \left[\frac{F_o^2 \nu}{36D\phi k(H - h + x_o)\Lambda^2}\right]^{1/3}. \tag{2.17}$$

Thus the interface is determined not from (2.13) but rather from

$$\begin{aligned} 0 = \left(\frac{A}{\Lambda b}\right)^3 \left(\frac{k_f}{k}\right)^3 \xi^3 + \left[\frac{3b}{H}\left(\frac{A}{\Lambda b}\right)^3 \left(\frac{k_f}{k}\right)^3 - \frac{1}{Ra}\right]\xi^2 \\ + \left[3\left(\frac{b}{H}\right)^2 \left(\frac{A}{\Lambda b}\right)^3 \left(\frac{k_f}{k}\right)^3 + \frac{2}{Ra}\left(1 + \frac{x_o}{H}\right)\right]\xi \\ + \left(\frac{b}{H}\right)^3 \left(\frac{A}{\Lambda b}\right)^3 \left(\frac{k_f}{k}\right)^3 - \frac{1}{Ra}\left(1 + \frac{x_o}{H}\right)^2. \end{aligned} \tag{2.18}$$

In order for (2.18) to admit a physically-acceptable solution, at least one of the terms from the equation must be a negative number. We therefore require

$$\frac{3b}{H}\left(\frac{A}{\Lambda b}\right)^3\left(\frac{k_f}{k}\right)^3 < \frac{1}{Ra}, \tag{2.19}$$

and/or

$$\left(\frac{b}{H}\right)^3\left(\frac{A}{\Lambda b}\right)^3\left(\frac{k_f}{k}\right)^3 < \frac{1}{Ra}\left(1+\frac{x_o}{H}\right)^2. \tag{2.20}$$

Because $x_o > 0$ and b/H is typically less than unity, we expect (2.20) to be satisfied before (2.19). In instances where neither inequality is satisfied, $\xi = 0$, i.e. there is no accumulation of solute-bearing fluid along the bottom boundary.

Solutions to (2.18) are given in figure 2-3, which shows the variation of ξ with $A/(\Lambda b)$ and Ra for various k_f/k, b/H and x_o/H. In all four cases, ξ is predicted to decrease with Ra and the non-dimensional cross-sectional area of the fissure, $A/(\Lambda b)$. In panel (b), we imagine a scenario in which the fissure shape is modified leading to a fourfold decrease in the fissure permeability, k_f. There is therefore a greater resistance to flow through the fissure resulting in large values for ξ. Conversely, in panel (c), b/H is increased from 0.05 to 0.5; the corresponding increase to hydrostatic pressure yields a larger Q_{out} and smaller ξ. Finally, panel (d) considers an increase in the source volume flux, i.e. an increase in x_o, defined by (2.16). As a result of this extra volume of solute-bearing fluid supplied to the reservoir, ξ is larger than in the small x_o case.

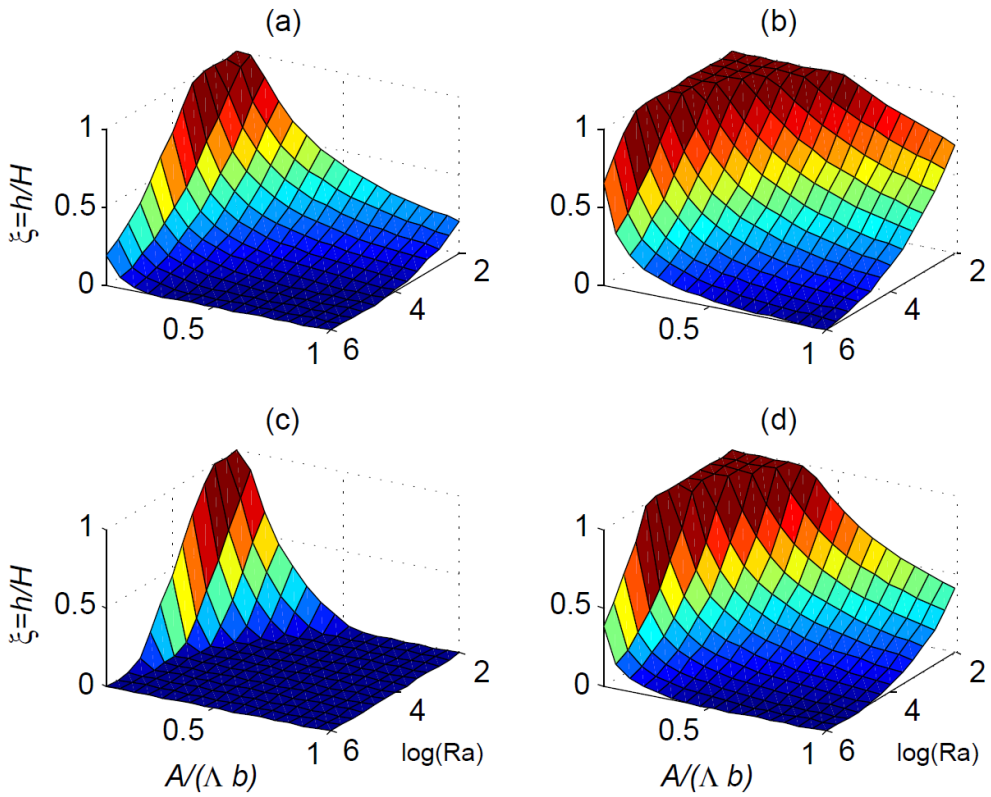

Figure 2-3: [color] Non-dimensional lower layer depth, $\xi = h/H$, vs. $A/(\Lambda b)$ and Ra as determined from the solution of (2.18). (a) $k_f/k = 1$, $b/H = 0{:}05$, $x_o/H = 0{:}5$; (b) $k_f/k = 0.25$, $b/H = 0{:}05$, $x_o/H = 0{:}5$; (c) $k_f/k = 1$, $b/H = 0{:}5$, $x_o/H = 0{:}5$; and (d) $k_f/k = 1$, $b/H = 0{:}05$, $x_o/H = 2{:}5$. Note that $\min[A/(\Lambda b)] = 0{:}05$, not 0.

A limitation of the preceding analysis is that it implicitly assumes that the fissure area and permeability are independent variables, when in fact k_f depends strongly on A. For the case of a circular fissure of diameter d_f, for example, Bear (1972) notes that

$$k_f = \phi \frac{d_f^2}{32}, \tag{2.21}$$

i.e. $k_f = A\phi/(8\pi)$. Figure 2-4 confirms that qualitatively similar results are obtained when $k_f = k_f(A)$.

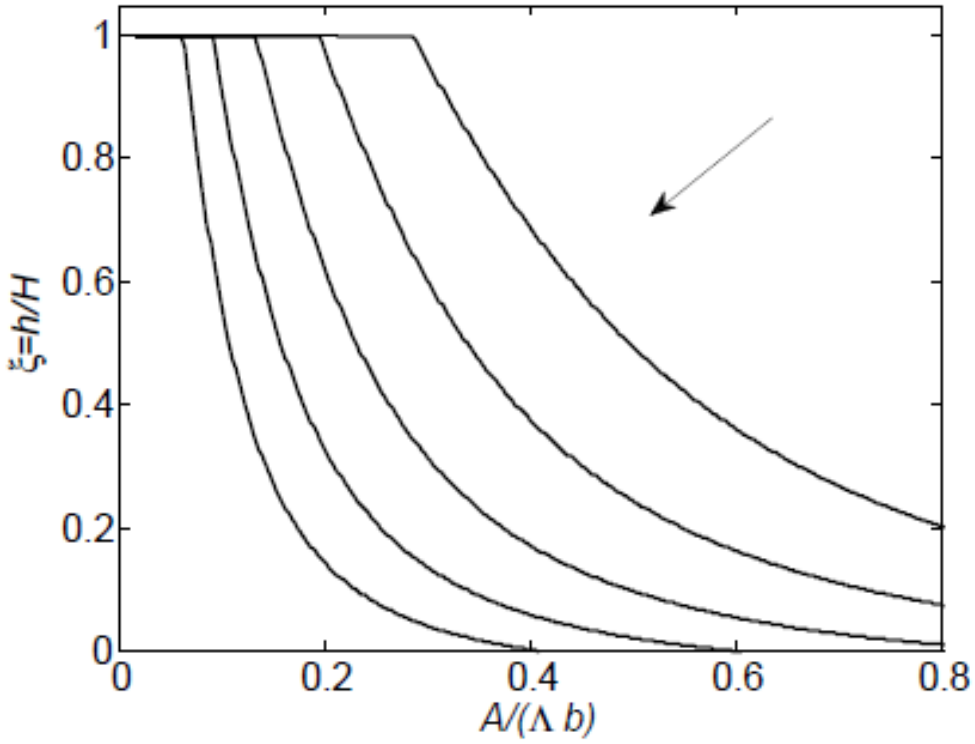

Figure 2-4: Non-dimensional lower layer depth, $\xi = h/H$, vs. $A/(\Lambda b)$ for $Ra = 10^2$, 10^3 … 10^6 (the arrow indicates the direction of increasing Ra). Here $b/H = 0.05$, $x_o/H = 0.5$ and k_f/k is determined using (2.21).

2.2 Draining flow scenario

Equation (2.10) gives an expression for Q_{out} under the assumption that Q_{out} is balanced by an equal influx due to the plume, i.e. Q_{H-h}. However, a separate category of the experiment may be performed (see figure 2-5) in which the plume is absent and we measure the draining of the dense layer in a process known as displacement ventilation (see Linden et al. 1990). In this circumstance, (2.10) remains valid, however, now it makes sense to equate this outflux to the time rate of change of the interface height.

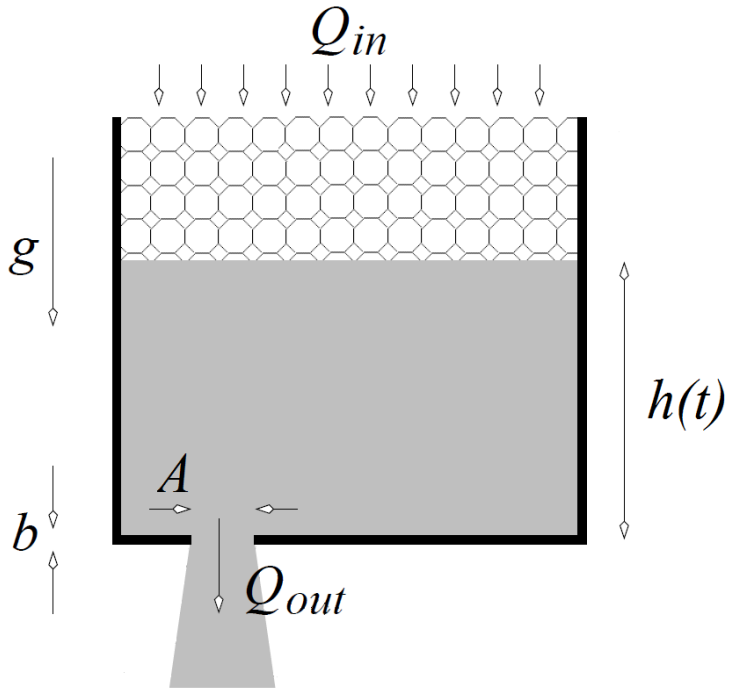

Figure 2-5: Draining flow scenario.

Accordingly, we write

$$Q_{out} = -\phi \Lambda \mathrm{W} \frac{dh}{dt}. \tag{2.22}$$

Replacing $\bar{g}'|_{H-h}$ with g' results in

$$-\phi \Lambda \mathrm{W} \frac{dh}{dt} = \frac{A k_f g'}{\nu} \left(\frac{h+b}{b} \right). \tag{2.23}$$

This substitution can be made because the density of the lower layer will be uniform in the absence of mixing. Separating variables and integrating (2.23) and using M drainage holes with a cross-sectional area $A = \pi d^2/4$ results in the following:

$$ln\left(\frac{h_o + b}{h + b} \right) = \frac{k_f}{\phi} \frac{M \pi d^2 g'}{4 \nu b W \Lambda} t\,. \tag{2.24}$$

From the point of view of the complementary laboratory experiments, k_f/ϕ is the only unknown parameter of (2.24). Thus as we further

document in §5.1, there is a direct way of experimentally estimating the fissure permeability, k_f.

Chapter 3

Experimental facility & procedures

This chapter will outline in detail the experimental facility and experimental procedures used when completing filling box and draining flow experiments. Below, §3.1 will discuss the experimental facility that was used and §3.2 will discuss the experimental procedures that were followed.

3.1 Experimental facility

3.1.1 Steel reservoir

The apparatus used to contain the fresh ambient fluid was a galvanized steel reservoir (figure 3-1) that was 122 cm in width, 122 cm in length and 181 cm in height which sat approximately 54 cm off of the laboratory floor. The reservoir was filled with roughly 2200 L of tap water. The water would be left overnight to reach room temperature of 20˚C. Each of the reservoir's vertical faces contained a clear acrylic window that measured 55

cm wide, 180 cm high and 1.26 cm thick. The free surface of the water was approximately 5 cm above the top of the research box, which is described in §3.1.3.

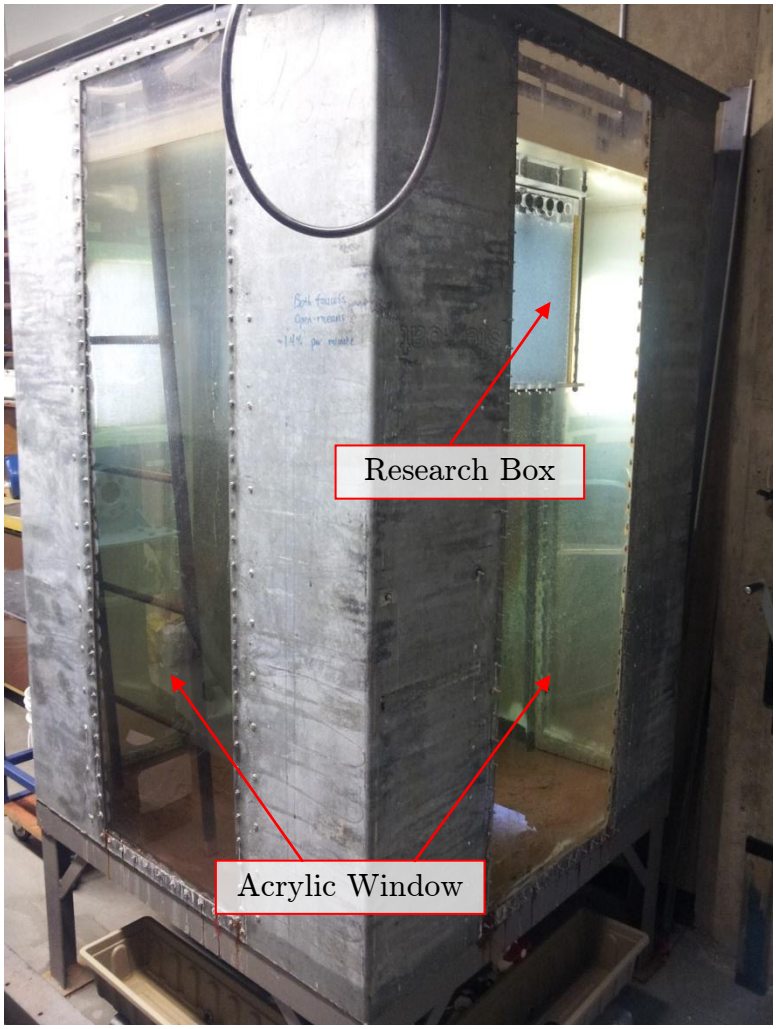

Figure 3-1: [color] Galvanized steel reservoir that contained the ambient fluid that the research box was submerged in.

3.1.2 Overhead reservoir

The overhead reservoir used to supply the dense saline fluid to the research box was a Gracious Living™ plastic storage container of approximate dimensions 59 cm long x 42 cm wide x 35cm high. It had an

approximate capacity of 65 litres. The overhead reservoir had a centered ½" ID male through-wall fitting (figure 3-2) on one endthat was located 2.54 cm from the bottom. This fitting was connected via ½" ID vinyl tubing to a ball valve which was used to turn the flow of dense fluid on or off. The same type of vinyl tubing was used to connect the ball valve to a maintenance valve that was used when disconnecting the overhead reservoir so that air would not enter the tube network. The maintenance

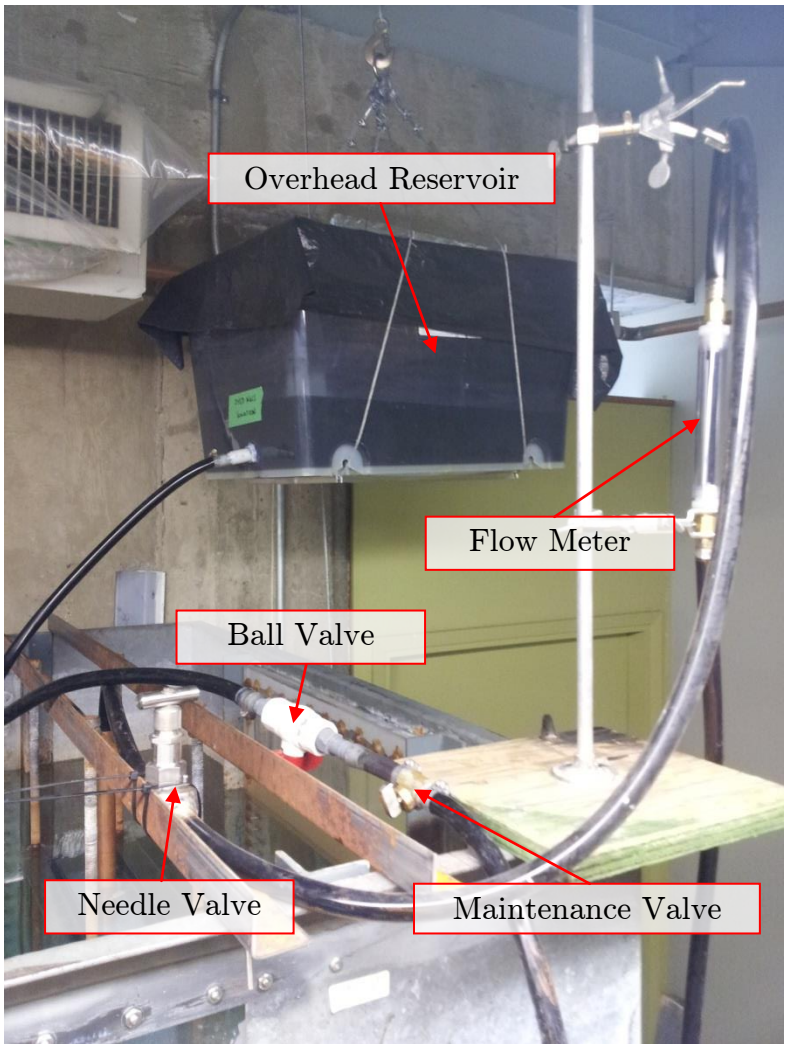

Figure 3-2: [color] The overhead reservoir that is firstly connected to a ball valve, then to a maintenance valve (which was only used when the overhead reservoir was disconnect to avoid air inside the tubing network), then to a flow meter, then to a needle valve and finally to the nozzle in the research box.

valve was connected to the flowmeter, which was used to measure the fluid flow rate. Measurements were based on readings made in a series of calibration experiments, which are described in more detail in Appendix B.3. The flow rate was controlled using a needle valve. Vinyl tubing was used to connect the needle valve to a nozzle (described below), that was inserted through the top plate of the research box. A ¾" ID copper tube of length 30 cm was used as conduit to provide rigidity to the vinyl tubing and nozzle. The copper tube was inserted through a hole in the top plate of the research box (see figure 3-5 below).

Figure 3-3 is a schematic of the order of equipment the saline fluid flowed through during a filling box experiment. Supplied by the overhead reservoir (§3.1.2) the saline fluid flowed through the tubing to the ball valve (§3.1.2) and through the flow meter (§3.1.2) where the flow rate

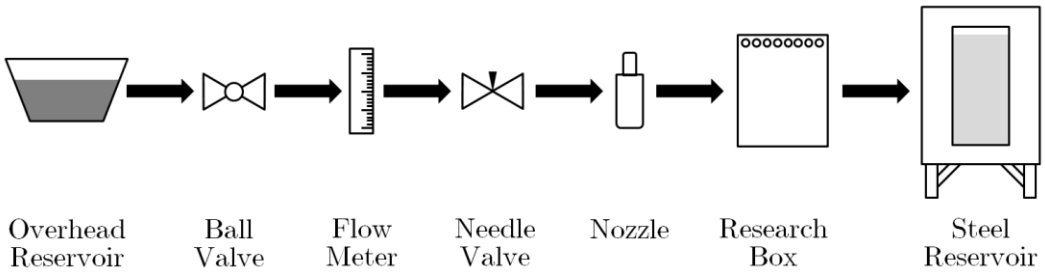

Figure 3-3: Flow direction of the saline fluid from the overhead reservoir.

was monitored. The fluid then passed through the needle valve (§3.1.2) and to the nozzle (§3.1.4) which was inside the research box (§3.1.3). The fluid descend through the research box and exited through the rubber stoppers (§3.1.3) and collected in the steel reservoir (§3.1.1).

3.1.3 Research box

The research box consisted of a clear acrylic box (figure 3-4) with internal dimensions 7.62 cm wide x 32.5 cm long x 40.6 cm high. The front and back sides had eight holes each that were 2.54 cm in diameter and were located 2.54 cm from the top edge. The hole centers were positioned 3.81 cm apart. To assist in measuring interface heights, the front right edge of the research box had a standard transparent plastic ruler mounted using double-sided adhesive tape. The bottom plate of the research box was 15.9 cm wide x 40.6 cm long x 1.26 cm thick and also contained eight holes that were 2.54 cm in diameter and positioned 3.81 cm apart. The top plate of the research box was 15.88 cm wide x 40.6 cm long x 0.95 cm thick and contained a 2.22 cm diameter hole in the center. On the underside of the top plate, strips of 1.27 cm wide closed-cell foam were used to create a tight seal when secured to the edges of the research box proper. The top and bottom plates contained four ½" guide holes in each corner of the plate. These allowed the research box to be suspended in the steel reservoir using four ½" galvanized steel threaded guide rods that were 75 cm in length (figure 3-5). The distance from the top of the research box to the bottom of the overheard reservoir was approximately 27 cm. An aluminum #40 mesh was cut to size and placed along the bottom of the research box in order to prevent the porous medium from draining out of the holes along the bottom boundary. This porous medium consisted of randomly packed spherical beads of uniform diameter. Two types of beads were used over the course of the experimental trials, i.e. Potters Industries A Series Premium 0.3 cm and 0.5 cm glass beads. Twelve #5-½ rubber stoppers from Fisher Scientific were used to externally plug the holes near

a) b)

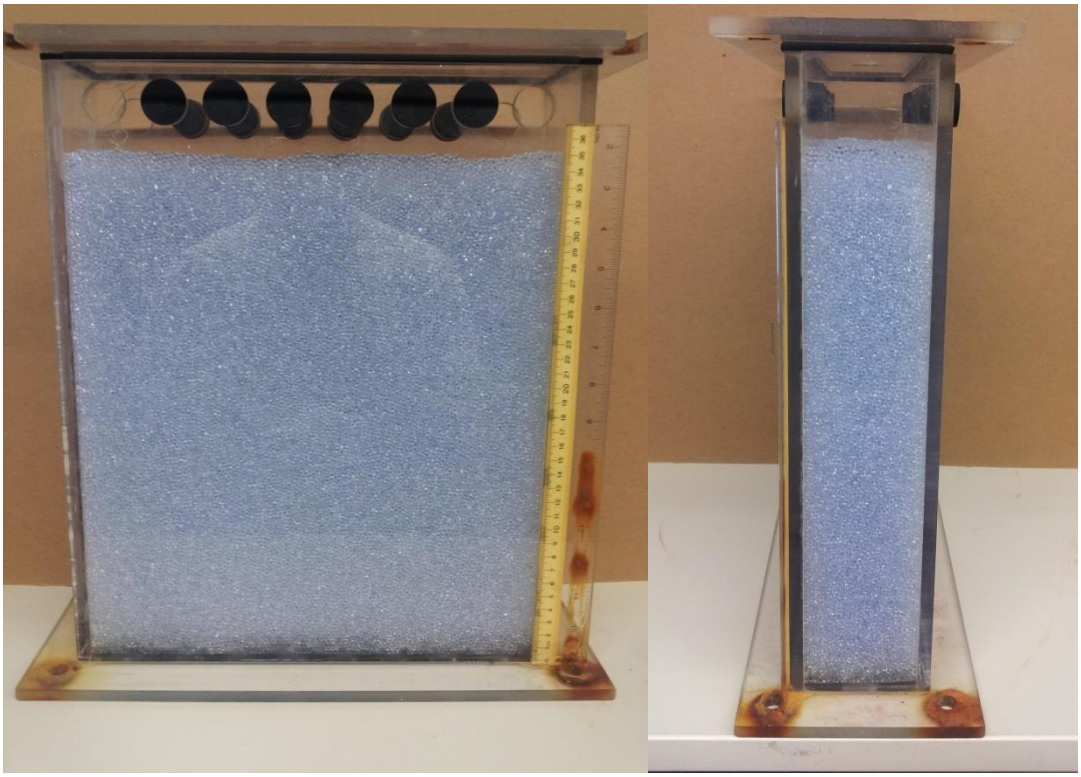

Figure 3-4: [color] The research box removed from the supports in the steel reservoir. The research box is seen from, a) the front, b) the right side.

the top, six per side (figure 3-4). This left a total of four holes open, which was sufficient to allow an easy flow of ambient fluid into the research box and, by extension, the porous medium. Where necessary, the same type of stoppers were used to plug the holes along the bottom plate. In this latter case, however, stoppers had to be cut to size because the full length stoppers protruded into the research box and were not then flush with the inside bottom boundary.

Figure 3-5: [color] A closeup of the research box submerged in the steel reservoir, supported by galvanized steel guide rods.

To allow for draining of the dense fluid, two additional sets of rubber stoppers were used (figure 3-6). The first set consisted of eight #5-½ rubber stoppers each with a hole of diameter 0.32 cm along the central axis. The second set consisted of eight #5-½ rubber stoppers each with a hole of diameter 0.48 cm along the central axis. Before drilling the holes with a hand-held power drill, the stoppers were frozen overnight so that they became rigid. The frozen stoppers resisted deformation and the holes

Figure 3-6: [color] Two rows of rubber one-hole stoppers used. The first row the stoppers have a hole diameter of 0.32 cm. The second row the stoppers have a hole diameter of 0.48 cm. The third row shows the ABS cylindrcal inserts used to further reduce the hole diameter to 0.14 cm.

that were drilled were as clean through and as circular as possible. For those experiments in which an even smaller diameter was required, we design a series of acrylonitrile butadiene styrene (ABS) plastic inserts, which were printed in 3D using an Object Eden350V printer. These inserts had a length of 2.0 cm, an inner diameter of 0.15 cm and an outer elected to diameter of 0.48 cm. They therefore snuggly fit into the second set of stoppers and also increased the effective depth of each stopper (figure 3-7). Because the ABS plastic absorbed water, the inner diameter of each insert constricted slightly to 0.14 cm.

a) b)

Figure 3-7: [color] The 0.48 cm diameter stoppers with the ABS cylindrical insert, a) outside of the stopper, b) inside of the stopper.

3.1.4 Nozzles

Three nozzles were designed for the experiments: an order-500-Re point source, an order-100-Re line source and an order-1-Re line source (Figure 3-8). These nozzles were composed to ABS plastic and were printed in 3D using an Object Eden350V printer. Detailed technical drawings and specifications for each appear in Appendix C.

The point source nozzle had a design that was similar to that presented by Hunt and Linden (2001) (see their figure 6). It was of cylindrical shape, had an internal diameter of 1.0 cm and was 5.0 cm in length. The bottom of the point source nozzle contained a hole that was 0.5 cm in diameter. Just above this hole was a fine #60 mesh used to filter any particles that may be present in the dense saline fluid.

The former line source nozzle, used for relatively large flow rates, was of a T-shape and spanned the width of the research box to act as close as possible to a purely two-dimensional source. The nozzle had an internal

diameter of 0.5 cm and was 7.1 cm in width. Along the bottom of the tube branch of the nozzle was a 0.1 cm slit from which saline fluid was discharged. Inside the nozzle was a plastic drinking straw cut to size and wrapped in aluminum meshing. The incoming saline fluid was spread evenly throughout the nozzle by the straw and meshing which resulted in a uniform line plume of saline fluid.

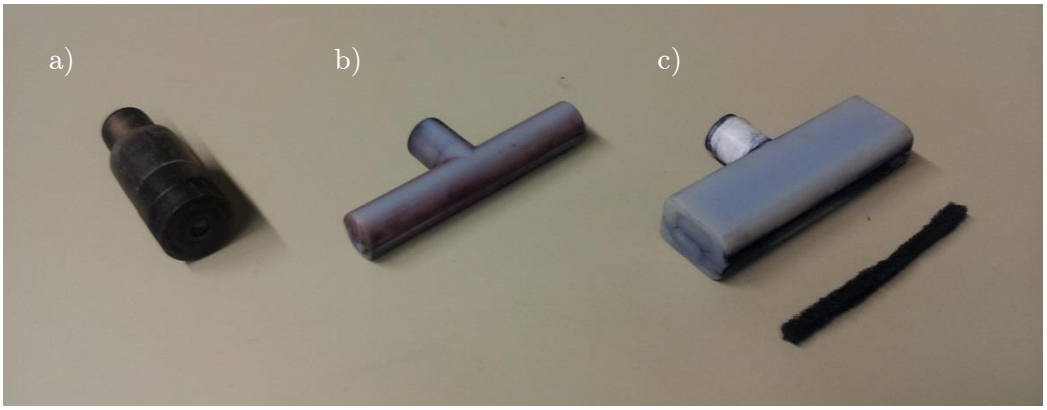

Figure 3-8: [color] The experimental nozzles used for a) order-500-Re point source, b) order-100-Re line source, c) order-1-Re line source.

The second line source nozzle, used for relatively small flow rates, was of a similar design to that described in the previous paragraph. It had an analogous T-shape and again, spanned the width of the research box. The internal structure was designed so that even at a low source volume flux, fluid was distributed along the width of the nozzle. The bottom of the nozzle had a 0.1 cm slit; the slit was flared to 0.4 cm so that exiting saline fluid would expand and further reduce its momentum. This slit was specifically designed to be 0.4 cm so that at a source volume flux of 0.1 mL/s, the source Reynolds number would be of order unity or less. Here the source Re is defined with specific reference to the dense fluid exiting the nozzle i.e.

$$Re = \frac{Q_o d_{bead}}{\nu A_{slit}}, \tag{3.1}$$

in which Q_o is the source volume flux, d_{bead} is the average diameter of the beads comprising the porous medium, ν is the kinematic viscosity and A_{slit} is the cross-sectional area of the slit in the nozzle. To solve issues of non-uniformity in the fluid plume, a small strip of foam was cut from a dish sponge and was inserted into the slit. This strip of sponge yielded a uniform plume at small Re. During experiments, the resulting line source plume was visually verified to be of uniform intensity across the width of the research box.

3.1.5 Optical equipment

Images of dyed dense fluid in the porous medium contained in the research box were taken using a Canon Rebel EOS T2i 18.0 megapixel digital camera with a 18-55 mm IS II zoom lens. The camera's optical settings were modified for low-light conditions. The aperture was set to 5.6, the shutter speed was set to 1/60 of a second and the ISO was set to 6400. The camera was mounted upon a Manfrotto 804RC2 Basic Pan Tilt Head which was itself mounted upon a Promaster Combi 25 tripod. So mounted, the camera was positioned 185 cm above the laboratory floor and 90 cm from the front window of steel reservoir (figure 3-9a). The back window of the steel reservoir was illuminated by an EIKI 3880 C overhead projector. The back window had a 48 cm wide and 61 cm tall piece of white sketching paper taped to its outside surfaces to diffuse the light provided

by the projector (figure 3-9b). During an experiment, the laboratory lights were turned off to reduce the glare from the windows of the steel reservoir.

a) b)

Figure 3-9: [color] Optical equipment used to capture images: a) Camera and tripod, b) Overhead projector.

3.2 Experimental procedures

3.2.1 Making the dense saline fluid

A batch of dense saline fluid was made by filling the overhead reservoir with approximately 45 L of fresh water. The reservoir was then left to sit for a minimum of 24 hours to allow the water to reach room temperature. The water was dyed using one ˜28.35g bottle of #078 navy and one-half ˜28.35g bottle of #150 jet black Procion MX Cold Water Dye. After mixing, a metric tape measure was inserted into the overhead reservoir to measure the resting fluid depth, h_f. From this measurement, an approximation of the volume of fluid was obtained from the following empirical equation:

$$V = 0.012h_f^3 + 0.096h_f^2 + 0.187h_f \tag{3.1}$$

(Because the side walls of the container were tapered, (3.1) was obtained by estimating the length and width of the overheard reservoir as a function of height). Once an estimate for the volume of dyed water was determined, the mass of crystalline salt (NaCl) required to make a solution of prescribed density was determined using the salt tables (Appendix B.4). The mass of salt was measured using a Detecto 5 kg scale with a resolution of 0.025 kg. The dyed saline solution was thoroughly mixed by hand with a paddle/stir stick for approximately 5 minutes. A sample of the dyed saline solution was then collected using a Braun Injekt 2mL syringe. The syringe was injected into an Anton Paar DMA 38 Densitometer and after a few minutes the density of the dyed saline solution was determined in g/cm^3 to four decimals places at a reference temperature of 20.0˚C (as measured by the densitometer). If the measured

density fell below the desired density, salt was added as necessary until the desired density was obtained. The container was then covered by laying a black plastic garbage bag over the top of the container like a blanket to minimize evaporation. The tank was then hoisted approximately 275 cm above the ground using a customized pulley and boat winch system so that fluid could gravity drain through the valves and flow meter described in §3.1.

3.2.2 Filling the steel reservoir

The steel reservoir was filled via two fresh water sources and took roughly 70 minutes to fill. Inevitably, the fresh water contained bubbles of dissolved gas, a problem that was especially evident during the spring months. As the steel reservoir was filled, the bubbles would rise to the free surface, collect along the bottom of the research box, or enter the research box through the draining holes. By extension the bubbles would enter the porous medium and become trapped in the pore space between adjacent beads. This had the consequence of reducing the void fraction of the porous medium. To avoid this undesirable effect, eight stoppers were inserted into the bottom of the research box before the water level in the steel reservoir reached the bottom of the research box. Once the water level in the steel reservoir reached 1-2 cm below the open holes at the top of the research box, filling was suspended for a minimum of 24 hours to allow the ambient fresh water to reach room temperature and to allow a majority of the bubbles to ascend to the free surface. One of the two hoses from the fresh water sources was then positioned at the top of the steel reservoir and filling was resumed while the ambient fluid entered the

research box and caused the porous medium to become fully saturated will fresh water. Filling was stopped once the free surface reached 4-5 cm above the research box. Finally, the water below the research box was manually agitated to clear away any bubbles that had accumulated along its underside. When there were no bubbles remaining, the eight stoppers were removed to be replaced by one-hole stoppers as described below.

3.2.3 Experimental preparation

An experiment was run by initially inserting the desired combination of one-hole and solid stoppers into the bottom of the research box. A batch of dyed saline solution having some prescribed density was then made following the procedure outlined above. The overhead projector was then turned on to provide back-illumination and the camera was positioned on the opposite (front) side of the tank. In using the camera, auto-focus was employed so that the tank and its contents were clearly in focus. The time controller was then set to a desired interval (i.e. 15s) and maximum number of images (i.e. 200). The time interval was chosen so that for a draining flow experiment, discussed below, each subsequent image would capture minor changes in the depth and intensity of the dense layer over the entire experiment but not exceed the maximum number of images that had been manually set. For a filling box experiment, again discussed below, the time interval was chosen so that the height and density of the dense layer would have sufficient time to develop between consecutive frames yet prevent the total experimental run time from exceeding 5 hours. After the time controller was set, preparation was completed and an experiment was ready to begin.

3.2.4 Draining flow experiments

A draining flow experiment was completed by the following steps. After preparation, discussed above, laboratory lights were turned off and a reference image was taken. The reference image was used for image processing and will be discussed in more detail in §4. Thereafter, the research box was filled with saline water of prescribed density via a long plastic tube that was connected to the overheard reservoir. The plastic tube was inserted into the porous media until resistance from the porous media prevented the tube from being any further inserted. It was important that the end of the tube very nearly reached the bottom of the research box so that, upon filling, the dyed saline solution entrained a minimum amount of ambient fluid. The ball valve was then turned on and the research box filled with dyed saline solution until depth of the lower dense layer reached approximately 31 cm. The volume flux of draining fluid was much smaller than the volume flux of fluid being supplied to the dense layer. As a result, dense fluid was allowed to drain from the research box as it was being filled. The inlet tube was then removed from the porous medium and the 6' aluminum ladder that was used to alter parameters of the research box (stopper configurations, etc.) was removed from the line-of-sight of the camera. After the inlet tube was removed, the interface was not perfectly horizontal. As a result, the dense layer was left to stabilize for approximately 15-30 seconds or until the descending interface reached approximately 30 cm before the time controller was started and photographs began to be recorded. Therefore the draining flow experiment was left running as images were taken at the specified time interval. Once the maximum number of images was exceeded or the

interface height fell below 7-8 cm, the experiment was terminated and the resulting data analyzed.

3.2.5 Filling box experiments

A filling box experiment was performed by first inserting the copper tube, which housed the vinyl tubing and nozzle, through the top plate until the nozzle tip was approximately 32-33 cm (depending on the type of nozzle) from the bottom of the research box. The top plate was connected to the research box and the nozzle was positioned to properly span the width of the research box. The nuts on the guide rods were tightened to firmly secure the top plate in place (figure 3-4). The time controller was then set to a prescribed delay time (i.e. 10 minutes) and interval time (i.e. 45 minutes). The former parameter is the amount of time that elapses after the time controller is started before an image is taken. Once the nozzle was positioned correctly, the laboratory lights were turned off and a reference image was taken. The flow-control valve was then adjusted until the flow meter read the desired source volume flux (calibration data is given in Appendix B.3). The interface height was visually monitored until it appeared to become constant, which typically took about 30-60 minutes depending on the combination of experimental parameters. The time controller was then started, which allowed for an additional, say, 10 mins to elapse before an experimental image was recorded. (The extra time ensured that results were not biased by the experimenter's imprecise assessment of when steady state had been reached). The configuration of stoppers was altered manually by adding or removing them as required. Thereafter, the above procedure was repeated and a second experimental

image was taken. This process was continued until all planned stopper configurations had been exhausted. The first configuration used eight one-hole stoppers. The second used six one-hole and two solid stoppers. The third used four one-hole and four solid stoppers. The fourth and final configuration used two one-hole and six solid stoppers. Throughout the course of the filling box experiment, the flow meter was periodically monitored and the source volume flux kept at a constant value by making (minor) adjustments to the flow control valve as necessary.

Chapter 4

Image processing

The basic image-processing sequence for an experiment consisted of the following: once an experimental image was taken, it had to be analyzed to determine the position of the horizontal interface that separated the light upper and dense lower layers. Because this interface itself had some finite thickness, a precise determination of this position was not always straightforward to achieve. By utilizing the image processing capabilities of MATLAB, a consistent and unbiased estimate of the interface height was obtained for numerous images taken over the course of an experiment. The MATLAB algorithm used for image-processing can be separated into three essential steps: alteration, estimation and detection. Each step represents a distinct sub-routine. The MATLAB algorithm was used to analyze images from the filling box and draining flow experiments. From here forward, an image that contains a dense lower layer will be referred to as an experimental image. Conversely, an image from the laboratory in which no lower layer is present shall be referred to as a reference image. The reference image needs to be "blank", where the porous medium is saturated by ambient fluid only. Reasoning for this is given below.

The following images, shown in figure 4-1, were taken from a filling box experiment. One image, figure 4-1c, will be used in the following discussion as a canonical example to demonstrate how each sub-routine modified and analyzed experimental images. The final result of the sub- routines was an accurate estimate for the interface height. A flow chart outlining the steps and sub-routines of the image processing is shown in figure 4-2.

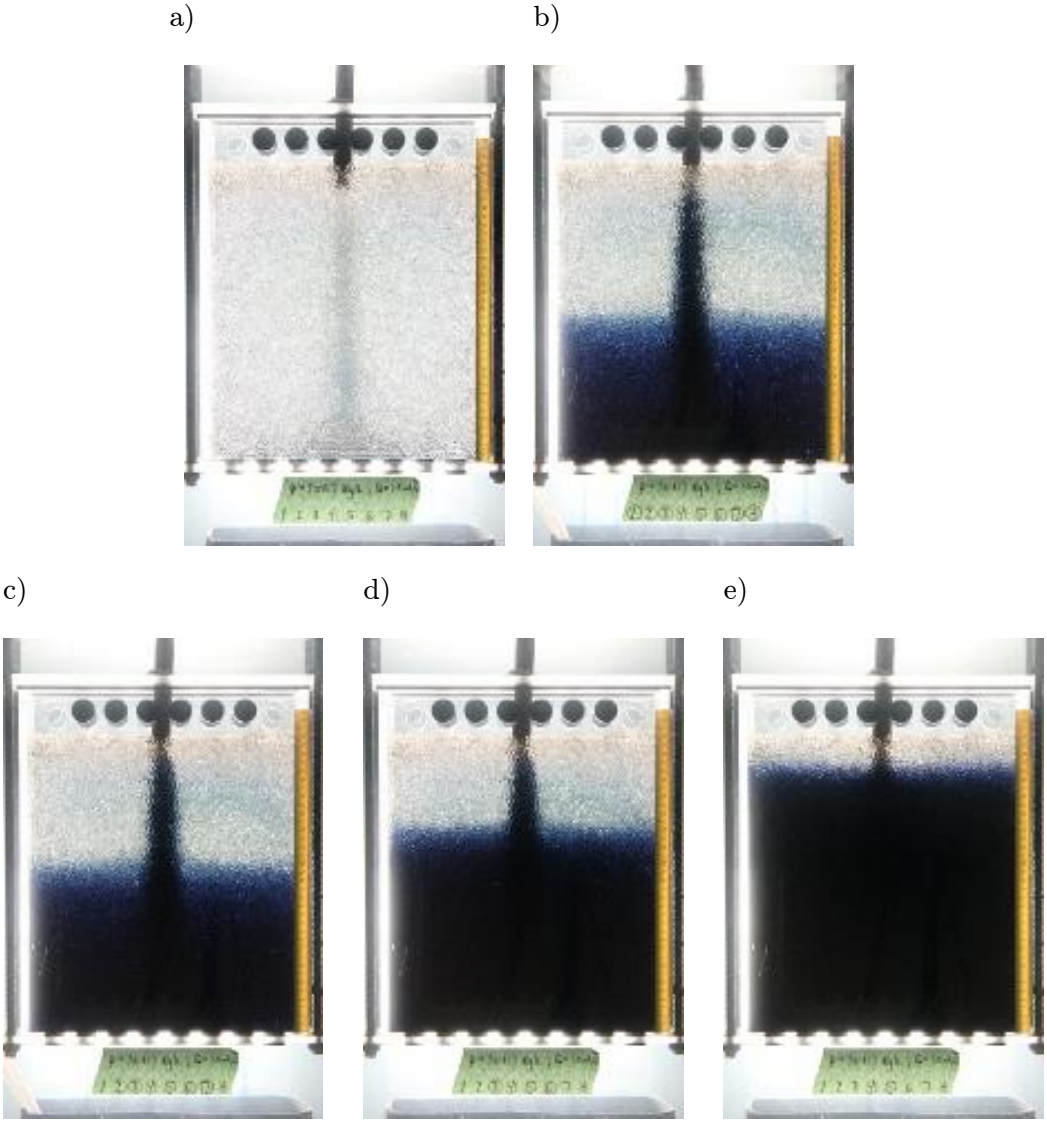

Figure 4-1: [color] Images taken during the course of a filling box experiment; a) before dense fluid flows into the tank, also known as the reference image, b) after 45 minutes has elapsed, c) after 90 minutes has elapsed, d) after 145 minutes has elapsed and e) after 190 minutes has elapsed. Experimental parameters are as follows: $g' = 42.02$ g/cm^3, $Q_o = 1.5$ mL/s and $d = 0.32$ cm.

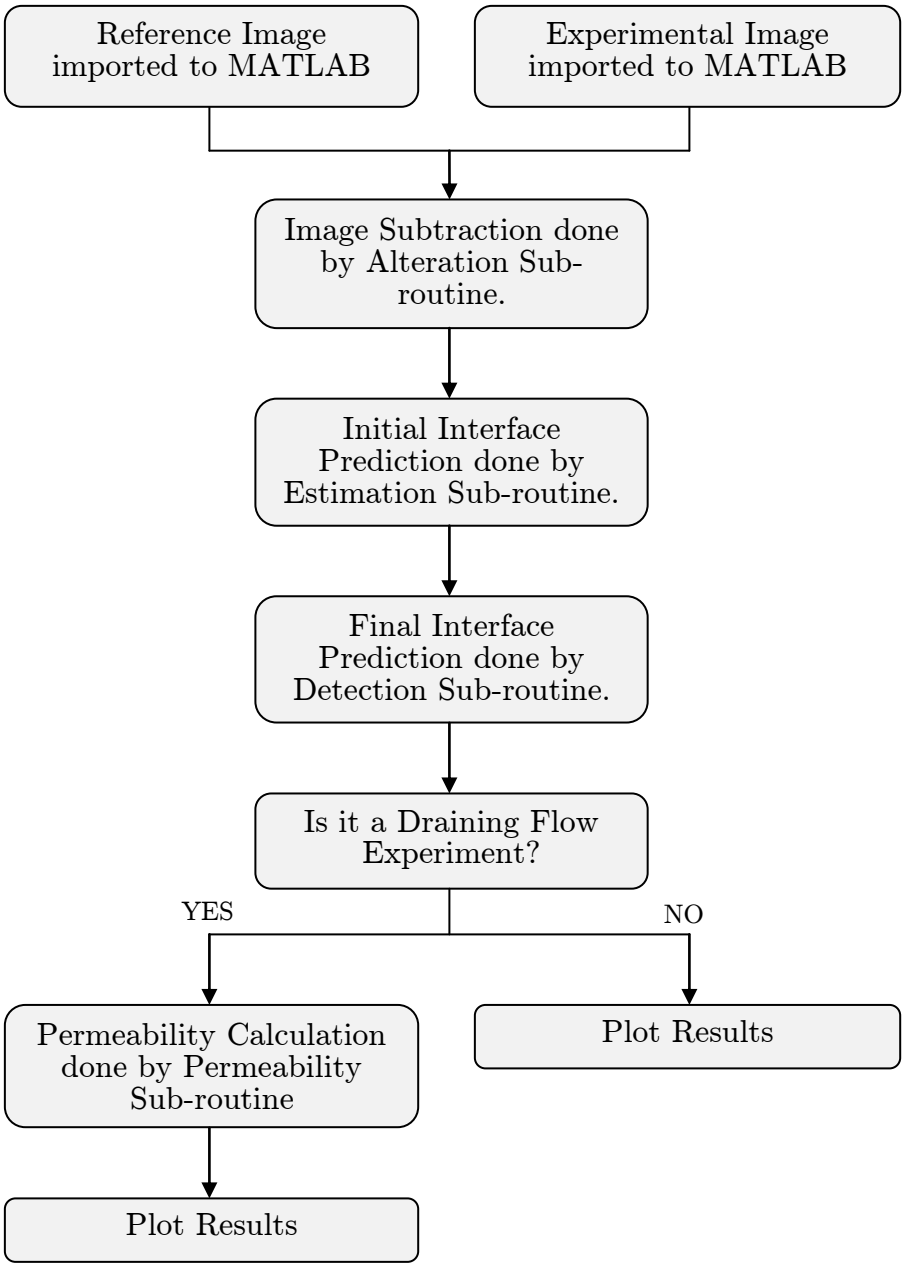

Figure 4-2: A flow chart describing the steps required to produce an estimate of the interface height.

4.1 Alteration sub-routine

The alteration sub-routine first imports a JPEG image into MATLAB. By default, MATLAB stores this image as a matrix where the image height and width (in pixels) correspond, respectively, to the rows and columns of the matrix. Because each image was 5184 pixels high and 3456 pixels wide, matrices were resized to 25% of their original size, which decreases the required computational resources and increases the speed at which frames could be processed. Also, at maximum camera zoom, all five of the images discussed previously contained irrelevant data (i.e. guide rods, copper conduit, stoppers, etc…) at the top and bottom of the image. Cropping

Figure 4-3: [color] A cropped and resized figure 4-1c that only contains information relevant to the determination of the interface height.

was therefore performed to eliminate these regions. Note that the center of the image, where the interface was obscured by the descending plume was also eliminated from the analysis. For future reference, the altered image (figure 4-3) was then saved in JPEG file format.

4.2 Estimation sub-routine

The estimation sub-routine imports resized and cropped experimental and reference images, then estimates the associated interface positions. This was achieved by first converting the interface image and the reference image to gray scale using the built-in MATLAB function rgb2gray. Each matrix element corresponded to the intensity of the associated pixel,

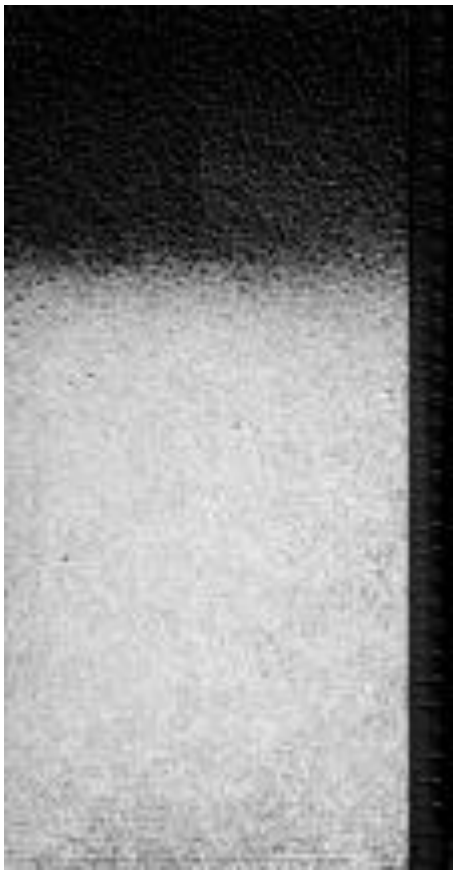

Figure 4-4: The result of an experimental image matrix being subtracted from a reference image matrix, known as a subtracted image.

ranging in integer values between 0 (black) and 255 (white). To minimize truncation errors during the image analyses, each matrix element was then converted to a double-precision floating point number value between 0 and 1. The matrix was then subtracted from that associated with the reference image and the result was stored in a new subtracted image matrix (figure 4-4). This subtraction step highlights those features that change between the initial instant, $t = 0$, and the time at which the image in question was taken. In particular, any features that remained the same are cancelled out and appear black whereas altered features appear white or gray. By this rationale, subtraction should only lead to positive intensity values ranging

a) b)

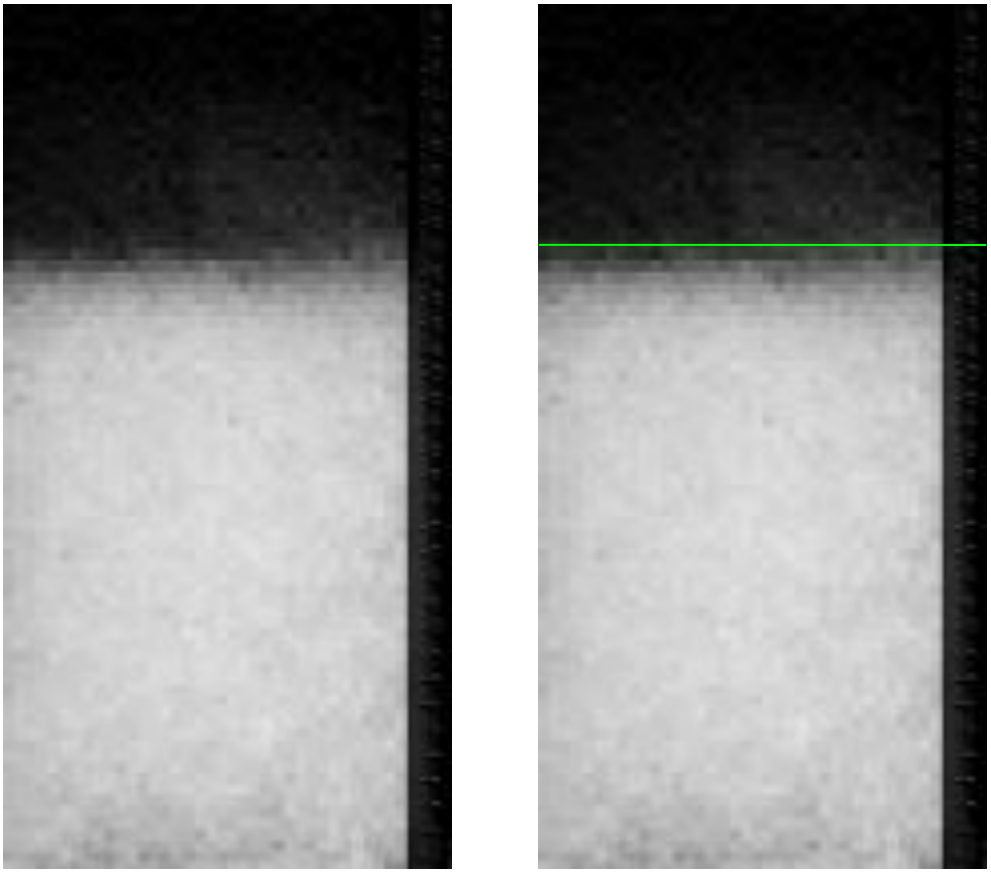

Figure 4-5: [color] The 'pixilated' image a) without an estimated interface height, b) with an estimated interface height shown by the green line. Signal noise (and also the fine details of the porous medium) evident in Figure 4-3 is less apparent.

between 0 and 1. However, small movements in the position of the research box e.g. when the stopper configuration was altered, caused a slight misalignment between the interface image and the reference image. As a result, elements in the subtracted matrix could become very slightly negative corresponding to signal noise, which had to be minimized so as to not significantly affect the overall analyses. Thus, the subtracted image was broken into blocks measuring 10 pixels by 10 pixels where the block intensity was the arithmetic average of its 100 constituent pixels (figure 4-5a). Averaging in this way minimized the influence of random perturbations whether of positive or negative sign. Thereafter, the arithmetic average of all the blocks in a row spanning the subtracted image was stored in a column vector. Because the interface height was approximately horizontal, row-averaging can be used to characterize the stratification of color intensity (and by extension, the stratification of density) that developed inside the research box. The column vector containing the row-averaged intensity values was then analyzed to ascertain the largest contrast between consecutive vector entries. This largest contrast provides an initial estimate of the position of the interface, which can be seen by the green line of figure 4-5b.

4.3 Detection sub-routine

The detection sub-routine took the previous estimate for h and returned a more precise estimate for the interface height. This was accomplished by analyzing the original, non-pixilated subtracted image and creating a new column vector of length 301 containing the row-average pixel intensity of 150 rows above and 150 rows below the initial estimate for h. The data in

this new column vector were then plotted against the normalized column vector index, in which 0 is the first index in the column vector and -1 is the last index. A 10^{th} degree polynomial was curve fitted to the data using MATLAB's built-in function polyfit (figure 4-6). The degree of the polynomial was chosen to be 10 because it was the lowest value that best represented the intensity data. No statistical analysis was performed when comparing the best fit curve to the intensity data.

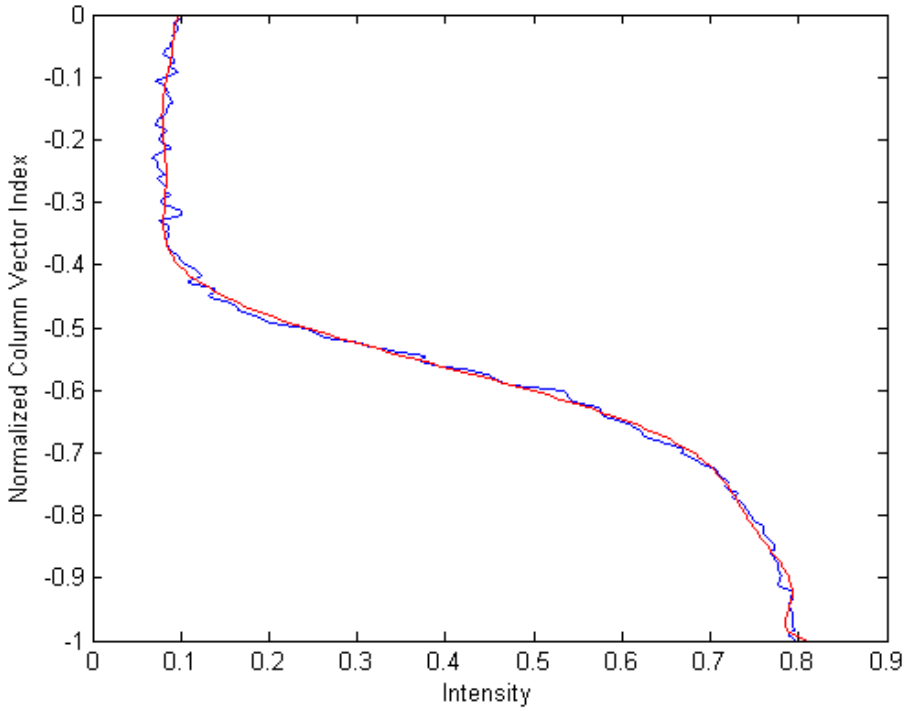

Figure 4-6: [color] The raw intensity data of figure 4-1c from the column vector calculated by the detection sub-routine versus non-dimensional image height x/H. Overlapped is a 10^{th} degree polynomial best fit curve.

From this polynomial, the column index associated with the maximum gradient of intensity was found and assigned the associated vertical position as the refined estimate for the interface height — see figure 4-7. From images such as this, the user can view both estimated interface values and can compare the red line against the ruler, which is

also evident on the right-hand side of the image. The point of intersection between the red line and the ruler was then recorded as the interface height for that experiment.

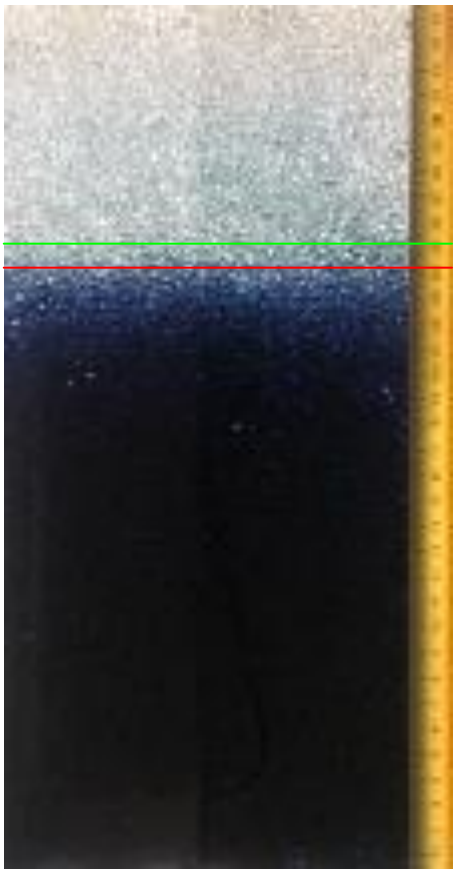

Figure 4-7: [color] The initial estimate for the interface height from the estimation sub-routine is shown by the green line. The estimate by the detection sub-routine is shown by the refined red line.

4.4 Fissure permeability sub-routine

When a draining flow experiment was completed, there were hundreds of images to analyze, many more than in the case of the filling box flow experiments. The four routines described previously were run for each image of the data set and the interface height was recorded into a column

vector. The column vector was then plotted against the time, $\hat{t}$, at which the image was taken. A representative example is given in figure 4-8, which considers the following experimental parameters: $g' = 51.84$ cm/s^2, $M = 8$ and $\Delta t = 12$ s. Using data such as those that appear in figure 4-8, (2.24) can be used to estimate the fissure permeability, k_f, or, more particularly, k_f/ϕ where ϕ is the porosity. First the data were

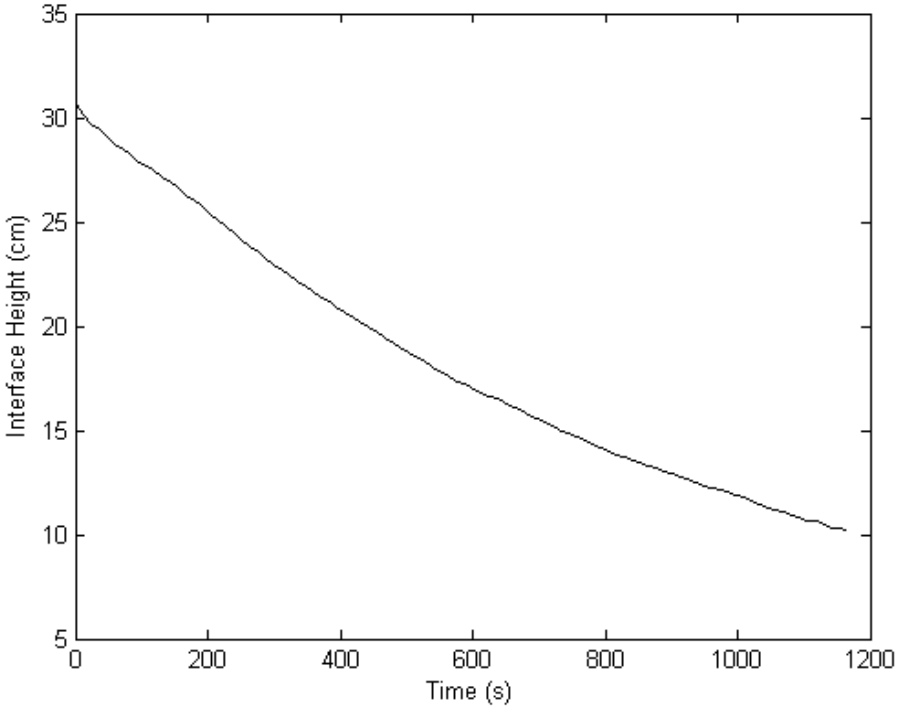

Figure 4-8: The descending interface height over time for $g' = 51.84$ cm/s^2, $M = 8$, $\Delta t = 12$ s and $d = 0.14$ cm.

plotted as in figure 4-9; MATLAB was then used to compute the slope, m, of the corresponding best fit line. With the numerical value of m known, k_f/ϕ was found as follows:

$$\frac{k_f}{\phi} = m * \frac{4\nu b W \Lambda}{M \pi d^2 g'}. \tag{4.1}$$

When applying (2.24) and (4.1) to determine k_f/ϕ, restricted attention was to the interval 10 cm $\leq h \leq$ 30 cm, or equivalently $0 \leq \ln[(h_o + b)/(h + b)] \leq 1$. Over this range, and consistent with (2.24) and Action et al. (2001), the data from an approximately a straight line when plotted as in figure 4-9. For data outside of the aforementioned interval, i.e. $h \leq 10$ cm, the fluid dynamics of the draining flow may become more complicated than predicted by a simple hydrostatic draining law. Indeed, it was not unusual for the data to exhibit some deviation from the straight line behavior as the depth of the lower layer became very small.

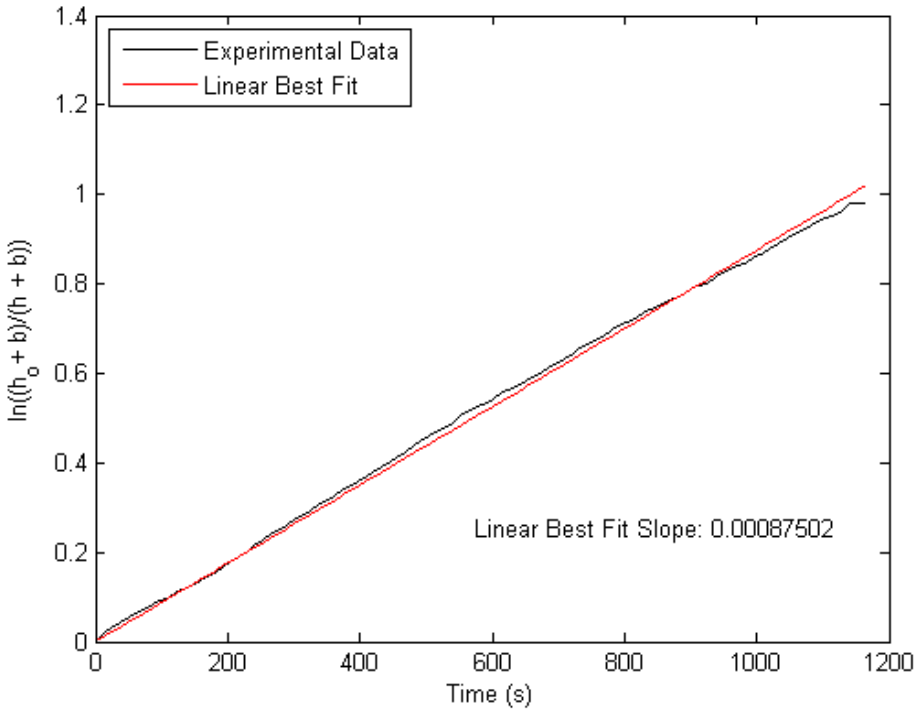

Figure 4-9: [color] The natural logarithm of interface height against time for $g' = 51.84$ cm/s^2, $M = 8$, $\Delta t = 12$ s and $d = 0.14$ cm. The best fit slope is displayed on the plot with a R^2 value of 0.99.

Chapter 5

Results & discussion

The data collected from experiments is presented and discussed below in three distinct sections. The first contains the results and discussion pertaining to the determination of the fissure permeability, k_f, from the draining flow experiments. The second and third will contain the results and discussion of filling box experiments using a line source of order-1 Re and order-100 Re respectively. The focus of §5.2.1 and §5.2.2 will be only on the data collected from filling box experiments using a (Cartesian) line source. Analogue results using a point source and yielding an axisymmetric plume are reported upon in Appendix A.2. Note that Darcy's law neglects fluid inertia and is therefore strictly valid only in the limit $Re \to 0$, which is, needless to say, impossible to achieve experimentally.

There are specific variables that remain constant throughout the following sections, such as measured parameters that describe the geometry of the research box and properties of the fluid, and parameters referenced from literature. Measured parameters include: the width of the research box W of 32.5 cm, the depth of the research box Λ of 7.62 cm and

the ambient fluid density ρ_a of 0.9982 g/cm^3. Referenced parameters from the literature consist of the solute diffusivity D of 2.5 x 10^{-5} cm^2/s (Linden, 1999) and kinematic viscosity ν of 0.01 cm^2/s (Kundu, 1991). The porosity, ϕ, of the medium could not be measured directly and so, for calculation purposes, an average of 0.425 was used based on the range $(0.38 - 0.47)$ of values given by Happel and Brenner (1965). This range is pertinent to the case of randomly packed spheres inside a control volume whose characteristic horizontal length is much larger than the (uniform) sphere radius. Using the average value for ϕ, the permeability of the porous medium, k, was calculated using (2.6).

5.1 Draining flow: determination of k_f/ϕ

The resistance to outflow exerted by the rubber stoppers is characterized by the fissure permeability, k_f, and needs to be determined in order to predict the interface height using (2.18). It was initially hypothesized that k_f would depend on the reduced gravity g', number of one-hole stoppers M, stopper hole diameter d and porosity ϕ. However, because ϕ could not be determined directly, the ratio of k_f/ϕ was measured from experiments to avoid a compounding of laboratory uncertainties. This ratio was determined from data sets collected from numerous draining flow experiments.

The first set of draining flow experiments used four values for g': 12.57$\pm$0.01 cm/s^2, 32.20$\pm$0.01 cm/s^2, 51.84$\pm$0.01 cm/s^2 and 71.47$\pm$0.01

cm/s^2. It also used one-hole stoppers with a hole diameter d of 0.48 cm and four configurations for the number, M, of one-hole stoppers, i.e. 2, 4, 6 and 8. The sub-routine described in §4.4 was applied to the measured data so as to populate a table of k_f/ϕ values; these are presented graphically as a surface plot in figure 5-1. The relationship for k_f in (2.21) given by Bear (1972) states that k_f is independent of g' and M. This prediction is contradicted by the data of figure 5-1, however. From the experimental data it can be seen that k_f/ϕ decreases as either g' or M is increased. Such discrepancies can be attributed to the assumption made by Bear that the flow is fully developed which is not the case here due to the short length of the stoppers employed. The second set of experiments used the same values of g' and M as the first. Here, however, a smaller stopper diameter d of 0.32 cm was used; the values of k_f/ϕ determined from the same sub-routine are shown in figure 5-2. Interestingly, despite the decrease in d, the quantitative behavior of k_f/ϕ in figure 5-2 is similar to that of figure 5-1.

The third set of experiments used $d = 0.14$ cm and the same values of g' as the previous two, however because the first and second set of experiments took an extensive amount of time to complete, only one value of M was considered. Moreover, because the time required to complete an experiment substantially increased as M approached 2, we elected to focus on the bookend opposite case of $M = 8$. An additional benefit of focusing on the $M = 8$ case is that k_f/ϕ exhibits a weaker dependence on M when

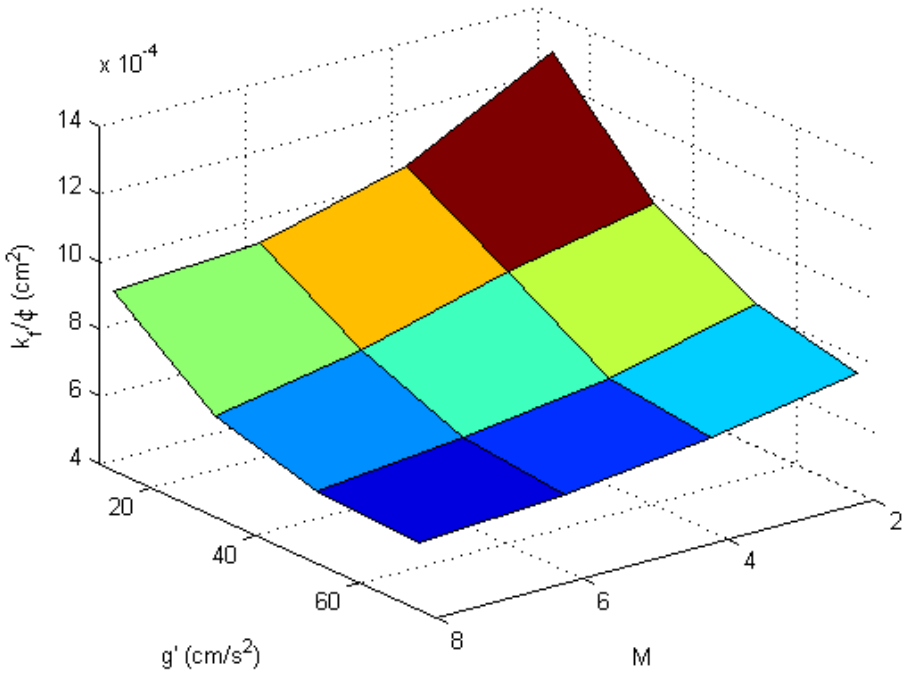

Figure 5-1: [color] Surface plot of k_f/ϕ values with respect to g' and M for $d = 0.48$ cm. Note that the minimum z-axis value is 4 x 10^{-4} cm^2, not 0.

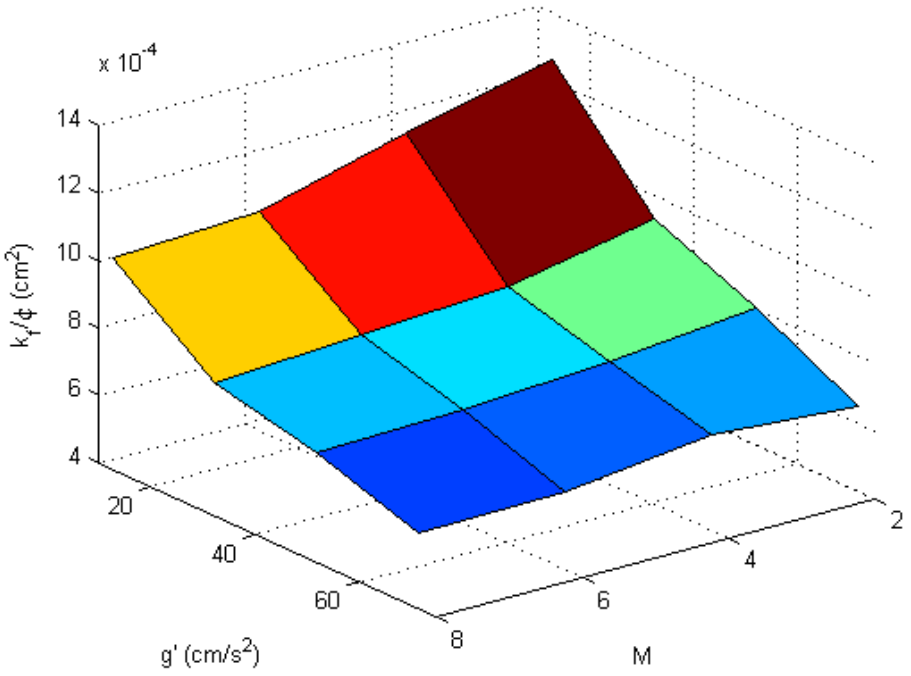

Figure 5-2: [color] As in figure 5-1 but with $d = 0.32$ cm.

$M = 8$ as compared to when $M = 2$ — see figures 5-1 and 5-2. The associated experimental data when M = 8 is shown in table 5-1.

Table 5-1: Values of k_f/ϕ ($\times 10^{-4}\ cm^2$) for $d = 0.14$ cm and various g'.

	M
	8
$g'(cm/s^2)$	
7.66	10.36
32.20	7.60
51.84	6.87
71.47	6.51

When a single value of M is chosen, i.e. $M = 8$, and k_f/ϕ from the above three data sets is compared against g' as in figure 5-3, it can be seen that the data points lie within experimental error of one another. (Note that a detailed error analysis in included in Appendix B.2). The error bars shown in figure 5-3 are based on the uncertainties of h and are used rather than standard deviation because a small number of data points were collected. On this basis, it can be concluded that k_f/ϕ has a insignificant dependence on d. Conversely, the variation of k_f/ϕ with the reduced gravity cannot be omitted. Once the descending plume reaches the lower boundary, the flow through the porous medium shifts to internal flow through M number of cylinders. If the flow were fully-developed, it would be described by the following equation (Poiseuille eq.):

$$v_f = \frac{d^2}{32}\frac{\Delta P}{\mu b} = \frac{d^2}{32}\frac{\Delta \rho g(h+b)}{\mu b}. \tag{5.1}$$

Equation (5.1) can be directly related to (1.3) where we see that $k_f = d^2/32$ which is consistent with (2.21). However, because the depth of the

lower boundary is quite small ($0.07 \leq d/b \leq 0.34$), the flow in the stoppers will never become fully developed. As a result, entrance and exit effects associated with flow through the stoppers cannot be neglected in relation to the skin friction associated with internal flow. Because entrance and exit losses increase with the fluid velocity, which is itself related to g', we would expect to observe a drop in the fissure permeability as the reduced

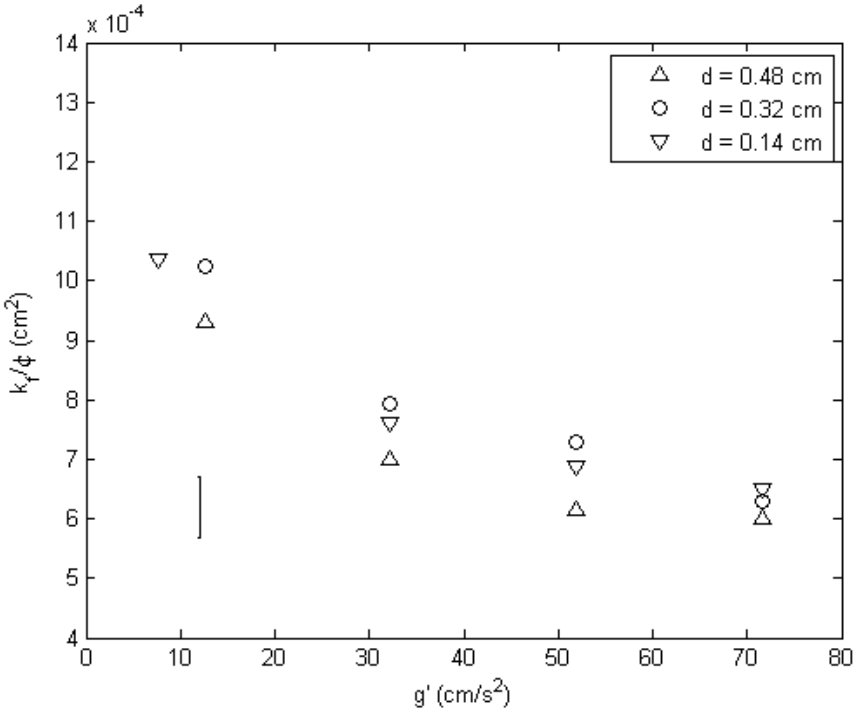

Figure 5-3: The values of k_f/ϕ from figure 5-1, 5-2 and table 5-1 for $M = 8$ with respect to g'. The representative error bar is shown in the lower left hand corner.

gravity is increased. This prediction is consistent with the trends exhibited in figures 5-1 and 5-2 and table 5-1. It is also consistent with Holford and Hunt (2001), who studied contracting flow through a sharp-edged vertical opening and found that viscous dissipation increased with g'.

Given the (not unexpected) shortcomings of (1.3) and (5.1), an expression for k_f/ϕ that better respects the experimental geometry (lack of fully-developed flow through the stoppers, etc.) remains to be

determined. For the purposes of making a comparison with the theory of §2, it is advantageous to consider the smallest value of d. For this reason, we shall focus specifically on that data presented in table 5-1 in deriving an empirical relationship that quantifies the variation of k_f/ϕ with g'. Because k_f/ϕ varies so weakly with d, not dissimilar results would have

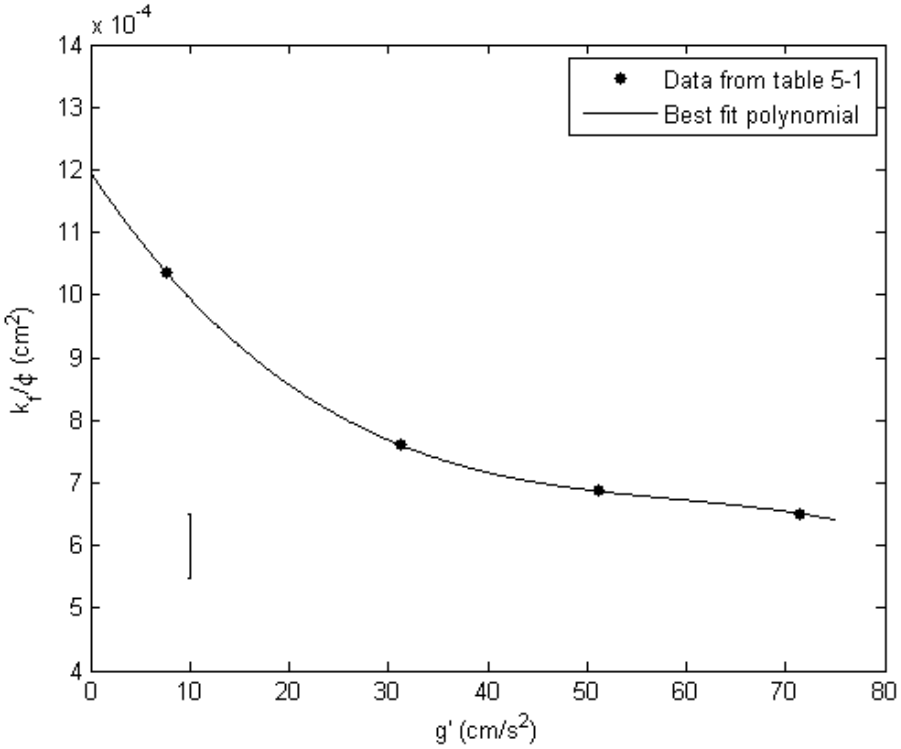

Figure 5-4: A best fit polynomial applied to the data from table 5-1 with experimental parameters: $M = 8$, $d = 0.14$ cm and $d_{bead} = 0.3$ cm. The representative error bar is shown in the lower left hand corner.

been achieved if we had instead chosen one of the other data sets from figure 5-3. The data from table 5-1 was plotted against g' and the results are shown in figure 5-4, which also includes a third-order polynomial best fit. The equation reads

$$\frac{k_f}{\phi} = -2.11 \times 10^{-9} \frac{s^6}{cm} (g')^3 + 3.73 \times 10^{-7} s^4 (g')^2 - 2.35 \times 10^{-5} s^2 cm (g') + 1.20 \times 10^{-3} cm^2. \quad (5.2)$$

Again, (5.2) is consistent with the findings of Holford and Hunt (2001) in which k_f/ϕ decreases as g' increases.

In the context of the filling box equations, (5.2), (2.17) and (2.18) are coupled, non-linear equations and solutions are obtained via an iterative process.

5.2 Filling box flow

5.2.1 Order-1-*Re* line source

With an estimate, k_f/ϕ, obtained from draining flow data, it is possible to compare the predictions of (2.18) against laboratory data from filling box experiments. It should be recalled, however, that (2.18) is derived in the limit $Re \to 0$ and so we should expect (and observe) relatively poor agreement if the source volumetric flow rate is too large. Thus for the purposes of comparing theory and experiment, we focus on experiments performed with the order-1-Re line source discussed in §3.1.4 and shown in figure 3-8c using dimensional variables, $Q_o = 0.1$ mL/s. By consequence, the majority of the fluid within the descending plume, say at the level of the interface, is fluid that was entrained from the ambient. Stated differently and for low Re flow, we sought to minimize the inertia of the plume, so that the source term, x_o, in (2.16) is approximately less than or equal to H, the total height of the research box. In addition, we consider a

vent diameter, d, of 0.14 cm and a bead diameter, d_{bead}, of 0.3 cm. The small vent diameter is chosen so that the contaminated plume fluid will not immediately drain out of the bottom of the research box.

It is now possible to solve (2.18) and make a prediction of the non-dimensional interface height $\xi = h/H$ for a prescribed g'. In contrast to §5.1, the filling box experiments considered the following three values of the fluid reduced gravity, g', at the nozzle souce: 12.57 cm/s^2, 42.02 cm/s^2 and 71.47 cm/s^2. However, from figure 2-2 it is shown that g' is a function of the vertical coordinate x insofar as g' decreases with x due to entrainment. To correctly predict ξ, iterations of (2.17) and (2.18) must be made to determine g' at the appropriate value of the interface height h. As part of this iterative scheme, k_f has to be calculated from the empirical equation (5.2), which predicts a greater resistance to flow for larger lower layer densities. Ultimately, we converge to a value for h where the hydrostatic force associated with the dense lower layer is balanced by the drag force associated with the flow through the (narrow) openings. The qualitative behavior of the so-plotted solutions agrees with intuition: as g' increases, the buoyancy flux F_o, and by extension Ra, which is defined by (2.14), also increases. The greater driving force results in an outflux of dense fluid from the research box.

Having a theoretical prediction for ξ, a comparison against experimental data can be drawn. The experimental images analyzed by the sub-routines in §4 produced values of ξ which can be seen in figure 5-5. It is apparent that the same qualitative behavior is observed in either case.

Thus, ξ decreases as either the number of one-hole stoppers M (by extension, the non-dimensional cross-sectional vent area) or g' increase. However, consistent with the predictions of (2.18), the reduction in ξ from the increase of vent area is much larger than the reduction from the

a)

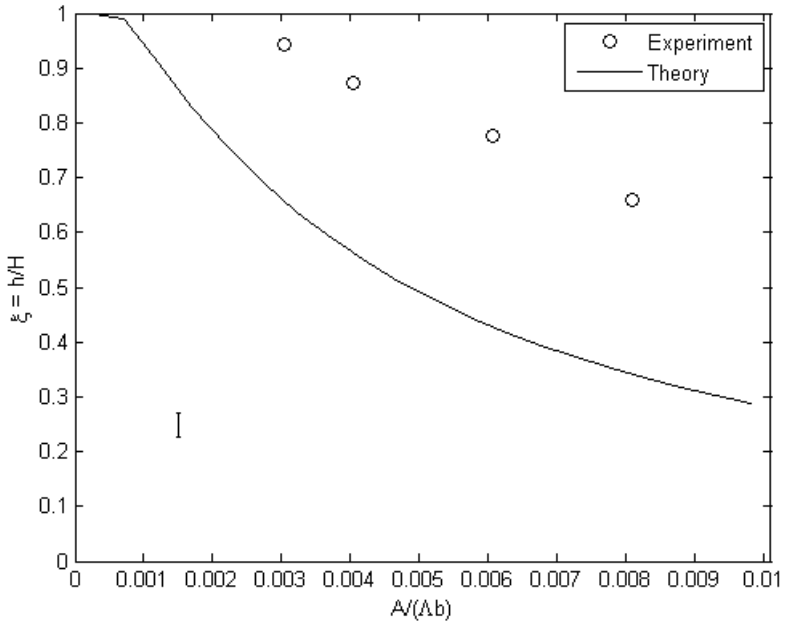

b)

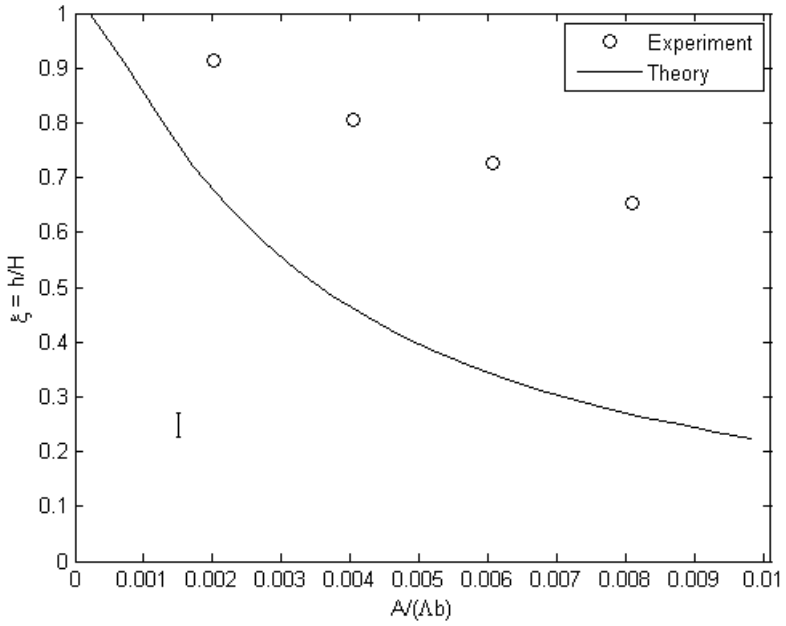

c)

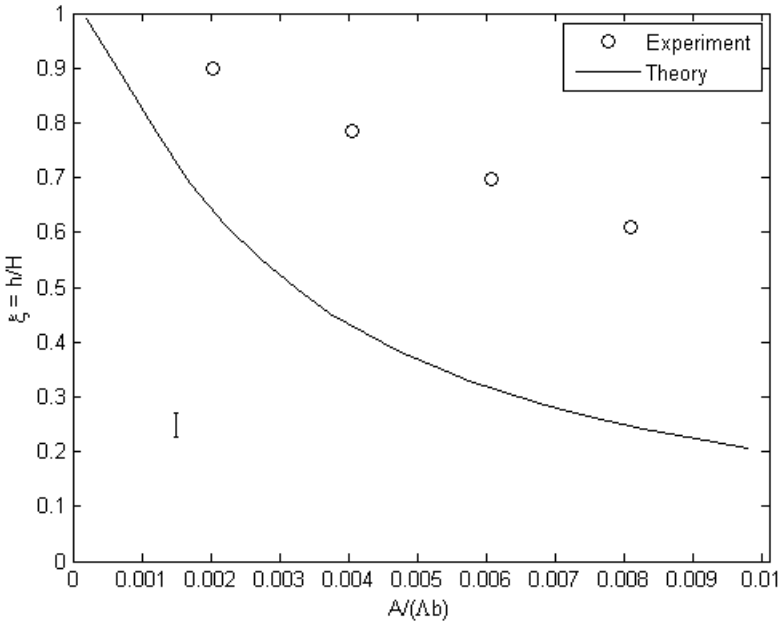

Figure 5-5: Comparison between the predictions of (2.18) and the experiment data of table B-1. Parameters are as follows: Q_o = 0.1 mL/s, d_{bead} = 0.3 cm, d = 0.14 cm and b = 2.0 cm. Each image has a different g' where (a) g' = 12.57 cm/s^2; (b) g' = 42.02 cm/s^2; and (c) g' = 71.47 cm/s^2. The representative error bars are shown in the lower left hand corner.

increase in g'. Interestingly, if we compare the influence that g' and M have on ξ against the influence they exert on k_f/ϕ, it can be noted that their comparative importance is reversed. This suggests that even though ξ and k_f/ϕ are related, i.e. as quantified by (2.18), the relationship is not one that can be trivially characterized. Returning to figure 5-5, there is good qualitative agreement between experiment and theory, however, the quantitative agreement is not especially robust, i.e. measured values for ξ are approximately twice as large as their theoretical counterparts. One possible explanation could be an under-prediction of entrainment by (2.15). Such an under-prediction would over-predict the reduced gravity g' of the lower layer, resulting in a theoretical lower layer depth that is being smaller than what is observed in the laboratory.

To verify whether the g' predictions made by (2.17) are accurate, fluid samples (1,2 and 3) were taken from inside the dense lower layer at a vertical position of 12 cm, 18 cm and 24 cm, respectively, during a filling box experiment for which $g' = 71.47$ g/cm^3, $M = 2$ and $h = 26.5$ cm. However, the most and least reliable parameters of (2.17) are the buoyancy flux, F_o, and the porosity, ϕ, respectively. The range of ϕ values for randomly packed spheres, given by Happen and Brenner (1965), are considered and two predictions for the reduced gravity g' using (2.17) were made. These predictions were compared against the measurements taken and the results of this comparison are shown in table 5.2. Here, the measured values of g' are approximately $23 - 35\%$ of the values predicted by our model, depending on the uncertainty of ϕ.

Table 5-2: Comparison of the predicted g' by (2.17) for two values of ϕ and the measured g' at a specific vertical height. Here the interface height $h = 26.5$ cm (i.e. $\xi = h/H = 0.828$) and the source conditions are: $g' = 71.47$ cm/s^2 and $Q_o = 0.1$ mL/s where $d = 0.14$ cm and $d_{bead} = 0.3$ cm.

Sample	x/H	$g'_{theory}(cm/s^2)$ $\phi = 0.38$	$g'_{theory}(cm/s^2)$ $\phi = 0.47$	$g'_{meas}\ (cm/s^2)$
1	0.26	37.14	24.31	8.74
2	0.45	37.14	24.31	8.45
3	0.63	37.14	24.31	8.06

In principle, there are several ways that the gap exhibited by the data of table 5-2 can be closed. Firstly, the model of §2 only considers entrainment from diffusion i.e. due to molecular processes. In fact, it is likely that entrainment into the plume is also influenced by convective motions and these can be included, in the model equations of §2 by replacing the Darcy equation with the Darcy-Forcheimer equation. In this

case the inertia terms are not neglected and plume entrainment is due both to this inertial contribution as well as molecular diffusion effects. The difficulty with this approach is that the terms in question are non-linear and we are therefore unaware of any closed form solution (self-similar or otherwise) to replace equations such as (2.7) or (2.15). Conversely, one could try to curtail convection in the experiments e.g. by the addition of glycerol to increase the viscosity of the ambient and plume fluids. However, this is impractical given the large volumes of fluid that are used in the present experiments.

5.2.2 Order-100-Re line source

The previous section considered a filling box flow where the source Reynolds number was deliberately minimized, however there are instances (see §1) where it is unreasonable to neglect fluid inertia from the start. Complementing the analysis of §5.2.1, the data presented here was obtained using an order-100-Re line source, discussed in §3.1.4 and shown in figure 3.8b. To represent high Re flow, source volume fluxes of 1.0 mL/s and 2.0 mL/s were used as compared to the lower value of 0.1 mL/s examined previously. Also, although we consider the same values of g' as before, attention is now restricted to a larger bead diameter, i.e. $d_{bead} =$ 0.5 cm. To accommodate for the increase in source volume flux, experiments were completed using a larger vent diameter where either $d =$ 0.32 cm or $d = 0.48$ cm ($b = 1.4$ cm in either case). The source Re associated with Q_o of 1.0 mL/s and 2.0 mL/s was, respectively, approximately 70 and 140. It is important to note that Re decreases as x

increases, — see (2.9). In high Re flow the inertia from the plume causes more entrainment from advection than it does from diffusion. Analogously, $x_o/H \geq 1$ whereas for low Re flow $x_o/H < 1$. A comparison of x_o/H for low and high Re can be seen in table 5-3. In this case, the disparities evident in figure 5-5 would be exacerbated suggesting, consistent with the limitations of Darcy's law, that (2.18) cannot be applied with confidence in explaining the details of the experimental data. Rather, our goal is to present these data without comparison to theory and to look to see whether similar qualitative trends to those seen in the low Re case are evident.

Table 5-3: Comparison of the calculated source term x_o/H for various source Re and g'. Here, $H = 32.0$ cm.

	Re		
$g'\ (cm/s^2)$	**1.06**	**70.4**	**141**
12.57	0.0747	2.78	11.1
42.02	0.0231	0.831	3.31
71.47	0.0136	0.488	1.94

The experimental data is presented in figure 5-6, in which we consider both vent diameters of 0.32 cm and 0.48 cm. Again, it is shown that for both values of d the same qualitative trends exist in which the non-dimensional interface height $\xi = h/H$ decreases as the non-dimensional exit area $A/(\Lambda b)$ increases. Figure 5-6 demonstrates that ξ generally increases with Q_o. At steady state, the volume of exiting fluid must, by extension, be larger to accommodate for the larger Q_o and as a result, the interface height must increase to provide the extra hydrostatic force that

a)

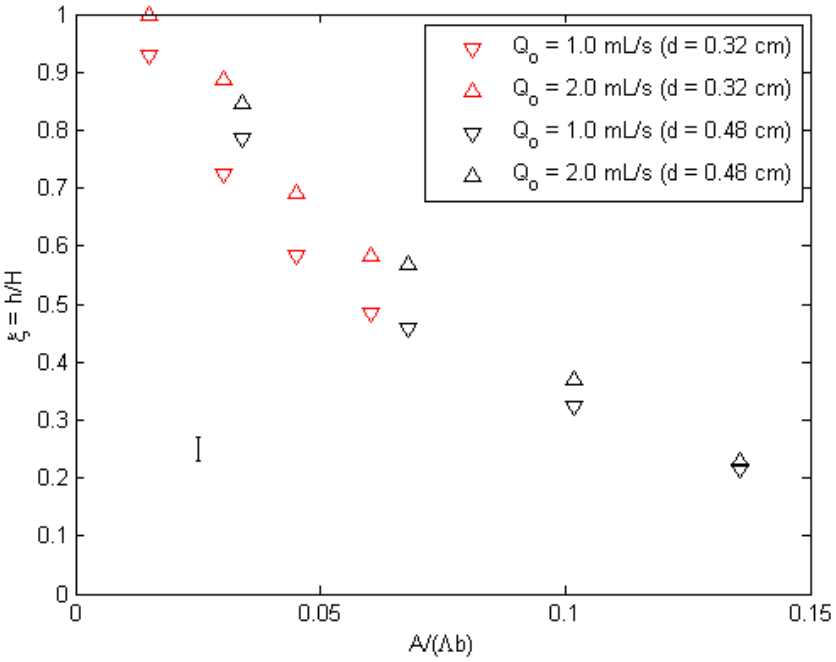
Q0 = 1.0 mL/s (d = 0.32 cm)
Q0 = 2.0 mL/s (d = 0.32 cm)
Q0 = 1.0 mL/s (d = 0.48 cm)
Q0 = 2.0 mL/s (d = 0.48 cm)
ξ = h/H
A/(Λb)
0
0.1
0.2
0.3
0.4
0.5
0.6
0.7
0.8
0.9
1
0.05
0.15

b)

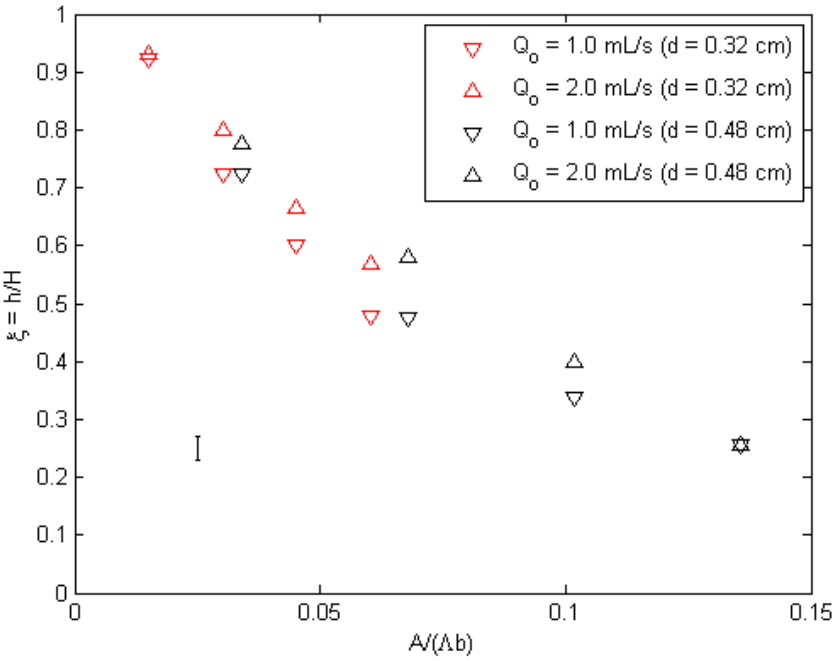
Q0 = 1.0 mL/s (d = 0.32 cm)
Q0 = 2.0 mL/s (d = 0.32 cm)
Q0 = 1.0 mL/s (d = 0.48 cm)
Q0 = 2.0 mL/s (d = 0.48 cm)
ξ = h/H
A/(Λb)
0
0.1
0.2
0.3
0.4
0.5
0.6
0.7
0.8
0.9
1
0.05
0.15

c)

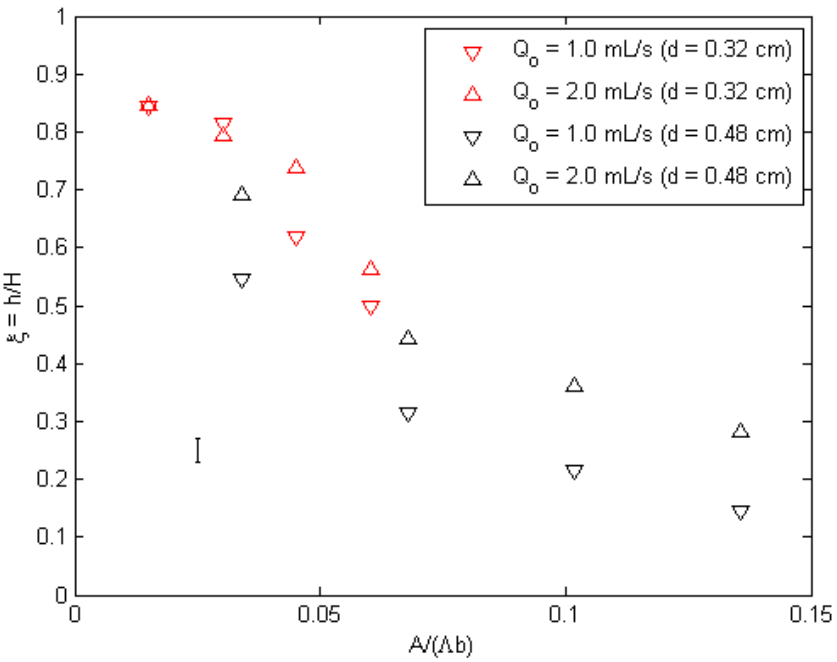

Figure 5-6: [color] Filling box experimental data for an order-100-Re line source compared against two values of Q_o and two values of d for the following experimental parameters: d_{bead} = 0.5 cm and b = 1.4 cm. Each image corresponds to a different g' where (a) g' = 12.57 cm/s^2; (b) g' = 42.02 cm/s^2; and (c) g' = 71.47 cm/s^2. The representative error bars are shown in the lower left hand corner.

is required to increase the amount of fluid draining from the bottom of the research box. However as Q_o becomes vanishingly small, the influence slight variations of Q_o have on the hydrostatic force become insignificant. If we compare the data for d = 0.32 cm against the data for d = 0.48 cm for each respective g', the effect of the difference on ξ is negligible. In figure 5-6, it is shown that d seems to have an extremely weak effect, which is consistent with figure 5-3. Overall, the qualitative trends exhibited in §5.2.2 are similar to those in §5.2.1 where ξ decreases as g' or M increases. Additionally, ξ increases as Q_o increases, which is evident in the discussion of point source results in Appendix A.2.

Chapter 6

Conclusions

6.1 Summary of present contribution

Convection in a porous media has been extensively studied, however complete understanding of this area has yet to be achieved. Wooding (1962) investigated a vertical two-dimensional Boussinesq flow in a homogenous porous medium at large Rayleigh numbers. Bejan (1978) and Nield and Bejan (1992) discussed line and point sources of buoyancy in a porous medium. Bear (1972) and Scheidegger (1974) investigated flow through a porous medium, where among other ideas, they considered variations of Darcy's law (i.e. the capillary tube model, fissure model, hydraulic radius model) when determining permeability. Happel and Brenner (1965) discussed the theory behind, and developed a relationship for, the volume flux at low Reynolds number through ducts of various geometry. More recently Phillips (1991) discussed hydraulically driven flow in a porous medium where the transport velocity can be expressed in terms of the hydraulic head difference. Phillips (1991) presented a relationship for the draining velocity which was expanded upon by Acton et al. (2001) and Pritchard et al. (2001). Building upon the work done by

Acton et al. (2001), Neufeld et al. (2009) presented the relationship quantified by (1.3), which prescribes the velocity of a fluid draining through a fissure, or crack. Guided by the work of Phillips (1991), Nield and Bejan (1992), Acton et al. (2001) and Neufeld et al. (2009) the theory presented in §2 was developed. A connection is made between the volume flux, of strength Q_o, at which a buoyant fluid, of density ρ_s, is supplied to a ventilated porous medium, of porosity ϕ and permeability k, in which the hydrostatic forces cause the fluid to drain from the porous medium through a fissure or crack, of cross-sectional A.

The main objective of this study was to determine a theoretical model that can predict the interface height h for a filling box flow scenario. This objective was completed and good qualitative, yet poor quatitative, agreement between theory and experimental data was observed. Initially, the model developed in §2 was compared against novel experimental data. However, (2.18) contained two unknown parameters: fissure permeability k_f and interface height h. In order to solve (2.18) for h, we had to determine k_f for the fissures (one-hole stoppers) used in our experiments. Section 2.3 presents an argument that supports the application of the draining law (1.3) to our measured data. From this observation we derived (4.2) for the ratio k_f/ϕ that was applied to data collected in the laboratory in §5.1 and an equation for k_f/ϕ was developed, (5.2), as a function of g'. In §5.1 the results of draining flow experiments are presented and after applying (2.24), k_f/ϕ was determined for each value of vent diameter d; corresponding results are shown

graphically in figures 5-1 and 5-2 and in tabular form in table 5-1. It is then shown that k_f/ϕ is a much stronger function of reduced gravity g' rather than d. The variation of k_f/ϕ with g' is given by (5.2) for $M = 8$ and $d = 0.14$ cm; when combined with (2.18) one can derive predictions for h. These are compared against experimental measurement in figure 5-6. In §5.2.1 the filling box data that had been collected for $Re \leq 1$ is discussed, and in figure 5-6 it is shown that the qualitative agreement between theory and experiment was good. However, quantitatively the measured values of h were approximately twice that of the predicted h as seen in figure 5-5. One explanation of the discrepancy between theory and experiment is that (2.18) under-predicts the volume of ambient fluid that is entrained into the plume. Specifically, (2.18) neglects entrainment from advection i.e. it considers diffusive transport only. As a result of under-predicting entrainment, the lower layer is predicted to be more dense than what is anticipated on the basis of the model equations of §2. To verify this explanation, measurements of g' were made from fluid samples taken from within the dense layer during a particular filling box experiment. It is shown in table 5-2 that the measured values of g' are approximately $23 - 35\%$ that of that predicted from (2.17), based on the uncertainty in the porosity ϕ, suggesting that the under-prediction of entrainment is indeed evident. One expects this discrepancy to be further exaggerated for still larger Re as with the experimental data of §5.2.2 (figure 5-7). For this reason, we omit a direct comparison with theory and instead focus on the qualitative trends of the data so as to compare these against the trends evident at lower Re. As is shown in figure 5-6 and 5-7, similar behavior is

noted e.g. h is a decreasing function of increasing g' and increasing $A/(\Lambda b)$ in either circumstance.

6.2 Outlook and future work

With an improved understanding of the fluid mechanics regarding Boussinesq convective flow in a ventilated porous medium, the results presented in §5 can be better related to the applications discussed in §1. Applying (2.18) to a leaky aquifer could relate the thickness of a light layer of sc-CO_2 that has accumulated along the upper boundary to the rate at which the sc-CO_2 drains through a fissure. Comparisons can be made of the residence timescale against those associated with dissolution and/or mineralization, which in turn may provide information regarding the volume of sc-CO_2 that will become permanently trapped underground. We can also use (2.7) and (2.18) to estimate the volume flux of oxygen-rich air into a compost pile that is needed to maintain optimal temperature, humidity and oxygen concentrations so thermophillic bacteria can operate at maximum efficiency. However, this estimation is dependent on the rising warm air that exits, or 'drains', through the top and the sides of the pile. Here, the source of buoyancy, or warm air, is not a discrete source. Instead, heat is generated throughout the compost pile. Problems of buoyant convection also arise in other contexts and in this sense, our analysis provides a starting point for how one might analyze heat and moisture transfer processes in these settings, especially when the outflow of buoyant fluid is somehow impeded.

While the ideas and results discussed in this thesis give insight into the fluid mechanics of convection in a ventilated porous medium, there are

some improvements that could be made. When developing our theory, the non-linear Forcheimer terms that account for inertial effects, were neglected. Unfortunately the extremely small Re required, to neglect entrainment from advection, cannot be easily replicated in a laboratory setting. Future work could consider the non-linear advection terms and, although an analytical solution may not be easily obtained, numerical modeling could be used to solve the suitably modified governing equations. Additionally, some of the equipment, such as the steel tank in §3.1.1, used in the experiments, was aged showing rust and leaks. A new steel tank could help reduce the particulates in the ambient fluid as well as improve the efficiency of experiments. Lastly, and even though this thesis is intended to be a fundamental (and idealized) study, future work could explore the impact of a spatially-variable permeability k and/or porosity ϕ which is more indicative of non-ideal aquifer or compost pile.

References

Acton, James A., Herbert E. Huppert and M. Grae Worster, "Two-dimensional viscous gravity currents flowing over a deep porous medium." *Journal of Fluid Mechanics* 440 (2001): 359-380.

Ahn, H. K., T. J. Sauer, T. L. Richard and T. D. Glanville, "Determination of thermal properties of composting bulking materials." *Bioresource Technology* 100 (2009): 3974-3981.

Bear, Jacob. *Dynamics of fluids in porous media*. New York: American Elsevier Pub. Co., 1972. 764.

Bejan, Adrian. "Natural Convection In An Infinite Porous Medium With A Concentrated Heat Source." *Journal of Fluid Mechanics* 89.01 (1978): 97-107.

Canadian Grain Commission. "Monitoring grain temperature and aerating grain." *Service Canada*. Web. 24 Jan. 2014. <http://www.grainscanada.gc.ca/storage-entrepose/mta-stv-eng.htm>.

Cloud, Harold A., and R. Vance Morey. "Management of Stored Grain With Aeration." *University of Minnesota Extension*. N.p., n.d.

Web. 6 Aug. 2013. <http://www.extension.umn.edu/distribution/cropsystems/dc1327.html>.

Darcy, Henry. *Les fointaines publiques de la ville de Dijon.* Paris: Dalmont. 1856

Happel, John, and Howard Brenner. *Low Reynolds number hydrodynamics, with special applications to particulate media.* Englewood Cliffs, N.J.: Prentice-Hall, 1965. 553.

Haynes, William M. *CRC Handbook of Chemistry and Physics.* 92 ed. New York: CRC Press, 2011. 2656.

Holford, Joanne M., and Gary R. Hunt. "The dependence of the discharge coefficient on density contrast – experimental measurements." *14th Australian Fluid Mechanics Conference.* December 10-14, 2001.

Hunt, G. R., and P. F. Linden. "Steady-state flows in an enclosure ventilated by buoyancy forces assisted by wind." *Journal of Fluid Mechanics* 426 (2001): 355-386.

Kaye, N. B., M. R. Flynn, M. J. Cook, and Y. Ji. "The role of diffusion on the interface thickness in a ventilated filling box." *Journal of Fluid Mechanics* 652 (2010): 195-205.

Kundu, Pijush K., *Fluid Mechanics.* 2 ed. Oxford: Academic Press Inc., 1991. 628.

Linden, P. F., G. F. Lane-Serff, and D. A. Smeed. "Emptying Filling Boxes: The Fluid Mechanics Of Natural Ventilation." *Journal of*

Fluid Mechanics 212.-1 (1990): 309-335.

Neufeld, J. A. , D. Vella, and H. E. Huppert. "The effect of a fissure on storage in a porous medium." *Journal of Fluid Mechanics* 639 (2009): 239-259.

Neufeld, J. A., D. Vella, H. E. Huppert, and J. R. Lister. "Leakage from gravity currents in a porous medium. Part 1. A localized sink." *Journal of Fluid Mechanics* 666 (2011): 391-413.

Neuman, Schlomo P., and Paul A. Witherspoon. "Field Dermination of the Hydraulic Properties of Leaky Multiple Aquifer Systems." *Water Resources Research* 8.5 (1972): 1284-1298.

Nield, Donald A., and Adrian Bejan. *Convection in porous media*. New York: Springer-Verlag, 1992.

Phillips, O. M. *Flow and Recations in Permeable Rocks*. Cambridge: Cambridge University Press, 1991.

Pritchard, David, Andrew W. Woods, and Andrew J. Hogg, "On the slow draining of a gravity current moving through a layered permeable medium." *Journal of Fluid Mechanics* 444 (2001): 23-47.

Pritchard, David, and Andrew J. Hogg, "Draining viscous gravity currents in a vertical fracture." *Journal of Fluid Mechanics* 459 (2002): 207-216.

Rowe, R. Kerry, and Prebaharan Nadarajah. "Evaluation Of The Hydraulic Conductivity Of Aquitards." *Canadian Geotechnical Journal* 30.5 (1993): 781-800.

Scheidegger, Adrian E. *The physics of flow through porous media*. 3 ed. Toronto: University of Toronto Press, 1974. 353

Schlichting, Hermann. "Laminare Strahlausbreitung." *Zeitschrift für Angewandte Mathematik und Mechanik* 13.4 (1933): 260-263.

Schlichting, Hermann, and K. Gersten. *Boundary-layer theory*. 8., rev. and enl. ed. Berlin. 1974

Trautmann, Nancy. "Compost Physics - Cornell Composting." *CORNELL Composting*. N.p., n.d. Web. 6 Aug. 2013. <http://compost.css.cornell.edu/physics.html>.

Vella, D., J. A. Neufeld, H. E. Huppert, and J. R. Lister. "Leakage from gravity currents in a porous medium. Part 2. A line sink." *Journal of Fluid Mechanics* 666 (2011): 414-427.

Wooding, R. A. "Convection In A Saturated Porous Medium At Large Rayleigh Number Or Peclet Number." *Journal of Fluid Mechanics* 15.04 (1963): 527-544.

Wolff, R.G. "Field and laboratory determination of the hydraulic diffusivity of a confining bed." *Water Resources Research* 6.1 (1970): 194-203.

Appendix A

Point source

A.1 Theory

The results of §2 can be readily extended to the case of a (negatively-buoyant) axisymmetric plume issuing from a point source. From the analytical details of Appendix E.2, we find that the plume volume flux is in this case given by

$$Q = 8\pi D\phi x\,. \tag{A.1}$$

In contrast to (2.7), the volume flux defined above (i) does not depend on the buoyancy flux, permeability or kinematic viscosity, and, (ii) varies linearly with x. The significance of these observations will become apparent below. Where (A.1) describes an ideal plume such that $Q \to 0$ as $x \to 0$, it is again helpful to consider a non-ideal plume with finite source volume flux, $Q_o > 0$. Thus (A.1) is replaced with

$$Q = 8\pi D\phi(x + x_o)\,, \qquad \text{where} \qquad x_o = \frac{Q_o}{8\pi D\phi}\,. \tag{A.2}$$

Here, (A.2) is similar to the expression given by Nield and Bejan (1992) for a point source of buoyancy. Interestingly, the momentum flux, M^*, is unchanged from the previous geometry, i.e. $M^* = F_o k/\nu$ so that

$$Re = \frac{F_o k \bar{d}}{8\pi D \phi \nu^2 (x + x_o)}, \tag{A.3}$$

Using (A.2) it is straightforward to derive the analogue (2.8), which reads

$$\bar{g}' = \frac{F_o}{8\pi D \phi (x + x_o)}. \tag{A.4}$$

By extension,

$$\bar{g}'|_{H-h} = \frac{F_o}{8\pi D \phi (H - h + x_o)}. \tag{A.5}$$

This latter expression is to be applied in (2.10). Indeed, when (2.10), (A.2) and (A.5) are combined, the following (implicit) expression for the non-dimensional interface thickness, ξ, is obtained:

$$\begin{aligned} 0 = \frac{1}{Ra}\xi^2 - \left[\frac{b}{H}\left(\frac{k_f}{k}\right)\left(\frac{A}{b^2}\right) + \frac{2}{Ra}\left(1 + \frac{x_o}{H}\right)\right]\xi - \left(\frac{b}{h}\right)^2 \left(\frac{k_f}{k}\right)\left(\frac{A}{b^2}\right) \\ + \frac{1}{Ra}\left(1 + \frac{x_o}{H}\right)^2, \end{aligned} \tag{A.6}$$

where the Rayleigh number is now defined as

$$Ra = \frac{F_o k}{(8\pi D \phi)^2 \nu}. \tag{A.7}$$

As compared to the right-hand side of (2.18), that of (A.6) is a quadratic, not a cubic, polynomial and one in which no reference to Λ is made. Note, moreover, that each term from (A.6) is proportional to k^{-1}. Consequently, and in contrast to the solutions of figure 2-2, ξ is not expected to vary with the permeability of the reservoir. This is consistent with the

observation that the plume volume flux given by either (A.1) or (A.2) is likewise independent of k.

Solutions of (A.6) are presented in figure A-1 where, as in figure 2-2, we consider two different values for each of k_f/k, b/H and x_o/H.

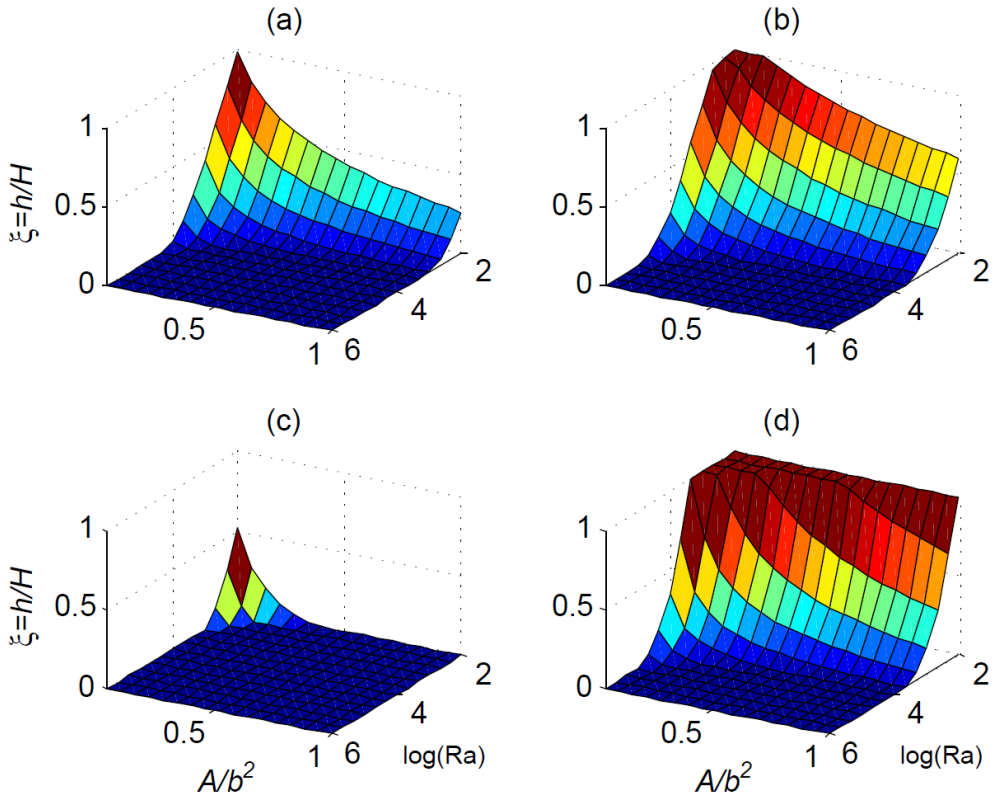

Figure A-1: [color] Non-dimensional lower layer depth, $\xi = h/H$, vs. A/b^2 and Ra as determined from the solution of (G.6). (a) $k_f/k = 1$, $b/H = 0{:}05$, $x_o/H = 0{:}5$; (b) $k_f/k = 0.25$, $b/H = 0{:}05$, $x_o/H = 0{:}5$; (c) $k_f/k = 1$, $b/H = 0{:}25$, $x_o/H = 0{:}5$; and (d) $k_f/k = 1$, $b/H = 0{:}05$, $x_o/H = 2{:}5$. Note that $\min[A/b^2] = 0{:}05$, not 0.

The variation of ξ with these parameters is qualitatively similar to figure 2-2 observed in the line source case in §2. In particular, figure A-1 shows that ξ is a decreasing function of Ra and the non-dimensional fissure area, which is here denoted by A/b^2.

A.2 Discussion

In contrast to the material in §5.2, the experiments discussed in this section were completed using an order-500-Re point source nozzle, shown in figure 3-8a and discussed in §3.1.4. Similar to §5.2.2 our focus will be on the qualitative trends rather than a direct comparison with theory because there were two main reservations (theoretical and experimental) that developed during the collection of the axisymmetric data. The first was an intuitional concern which arises from the expression for the plume volume flux, Q. In particular, (A.2) is independent of the permeability k. If we consider an impermeable medium, (2.7) predicts that Q for a line source would equal zero, but for a point source (A.2) would estimate a non-zero plume volume flux. The second reservation is related to the aspect ratio of the research box, in which the depth Λ was an order of magnitude smaller than the width W. Therefore entrainment into the nominally axisymmetric plume may not be uniform in the radial direction. Additionally, the geometry of the research box could have an impact on the measured results. Here, increasing Λ so that the box depth is comparable to its width, W, would decrease the amount of light from the overhead projector that penetrates through the porous medium. In the absence of such addition light, one would expect a lower image quality, which would compromise the accuracy which we can experimentally estimate the interface height, h.

The filling box experiments using the order-500-Re point source considered multiple values of the source volume flux Q_o and the reduced

gravity g'. For Q_o, the values were: 1.0 mL/s, 1.5 mL/s, 2.0 mL/s and 2.5 mL/s; and for g' the values were: 12.58 cm/s^2, 27.29 cm/s^2, 42.02 cm/s^2, 56.75 cm/s^2 and 71.47 cm/s^2. Other experimental parameters include: a vent diameter d of 0.32 cm and a lower boundary thickness b of 1.4 cm. The same four values of the number of open stoppers M were used: 2, 4, 6 and 8. Shown in figure A-2 is the non-dimensional interface height $\xi = h/H$ plotted against the non-dimensional exit area $A/(\Lambda b)$. It is seen that the same qualitative trends that are observed in figures 5-5 and 5-6 are indeed evident. Thus, as $A/(\Lambda b)$ increases, ξ decreases. It is also apparent, most especially from figure A-2e, that as Q_o increases, ξ increases which is consistent with figure 5-7.

a)

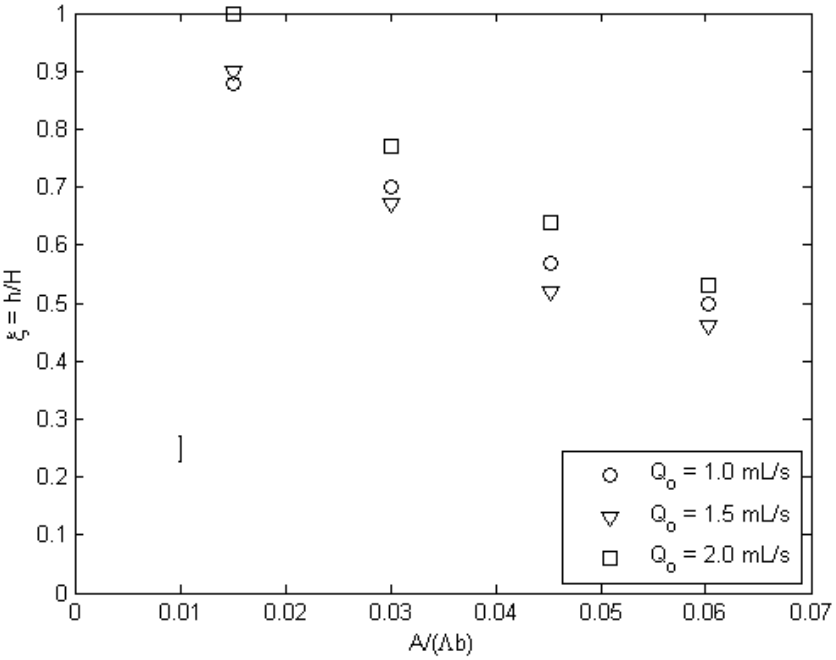

b)

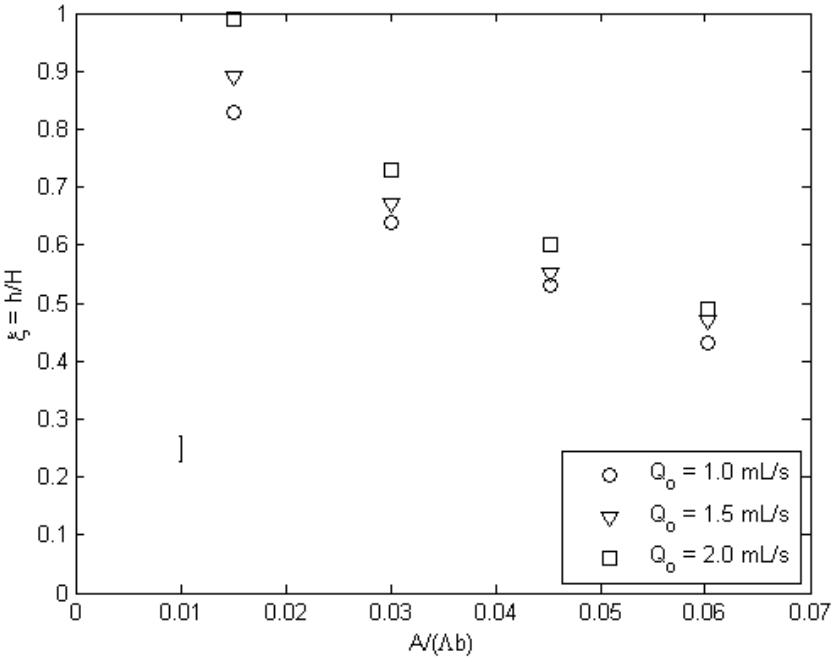
ξ = h/H
A/(Λb)
Q_o = 1.0 mL/s
Q_o = 1.5 mL/s
Q_o = 2.0 mL/s

c)

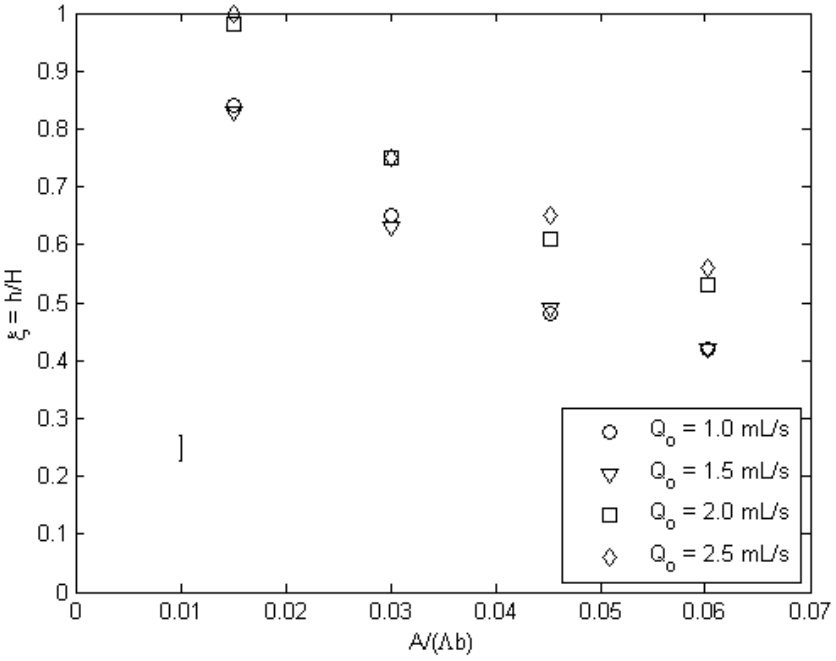
ξ = h/H
A/(Λb)
Q_o = 1.0 mL/s
Q_o = 1.5 mL/s
Q_o = 2.0 mL/s
Q_o = 2.5 mL/s

d)

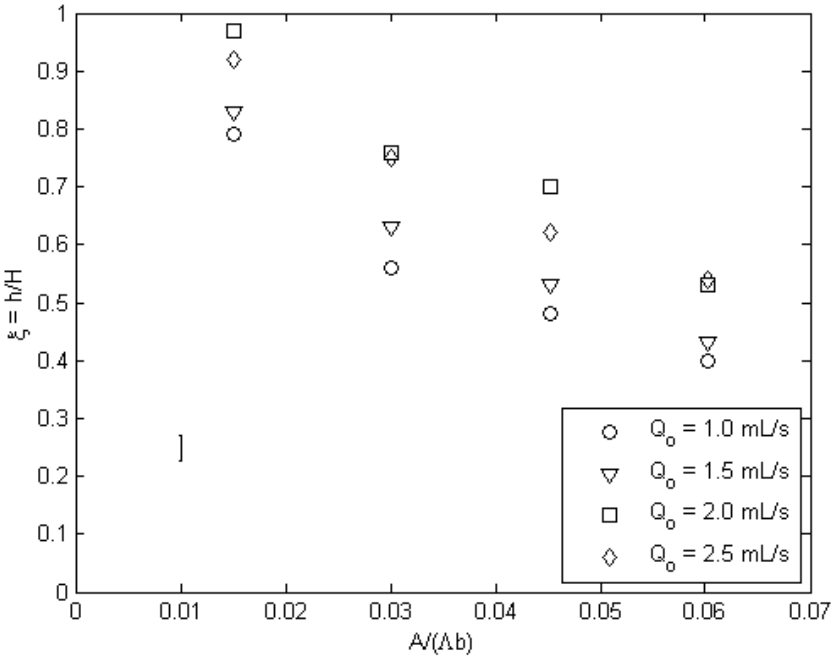

e)

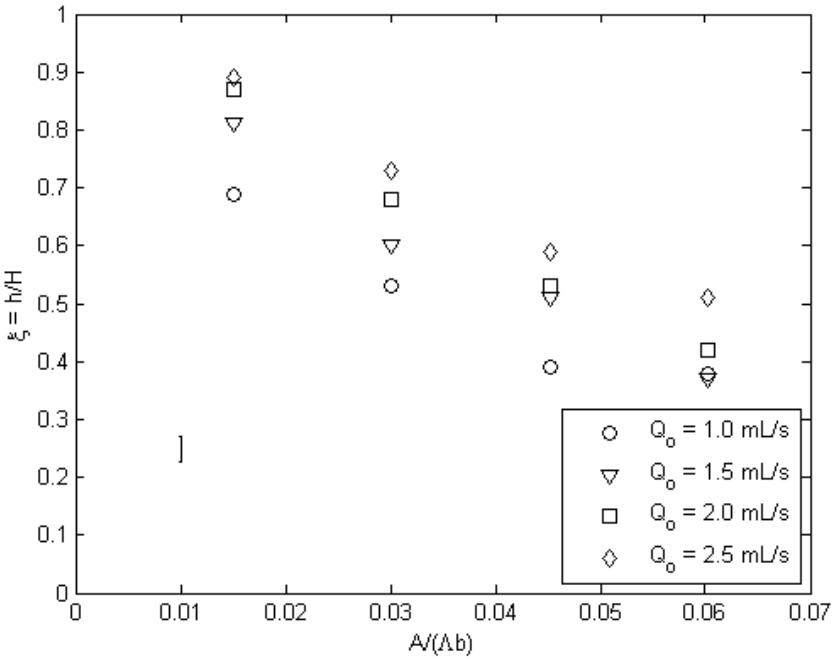

Figure A-2: Filling box experimental data for an order-500-Re point source for various Q_o . Other parameters are as follows: d_{bead} = 0.5 cm, d = 0.32 cm and b = 1.4 cm. Each image corresponds to a different g' where (a) g' = 12.57 cm/s^2; (b) g' = 27.29 cm/s^2; (c) g' = 42.02 cm/s^2; (d) g' = 56.75 cm/s^2; and (e) g' = 71.47 cm/s^2. The representative error bars are shown in the lower left hand corner.

Appendix B

Data, error, calibration & salt table

B.1 Data

In this section all of the data that has been collected experimentally will be presented in graphical and tabular form. The draining flow data in §B.1.1 is shown in graphical form since the data were collected against resulting in large data sets that are impractical to describe in tabular format. Conversely, tables are used to present the filling box data from §B.1.2

B.1.1 Draining flow

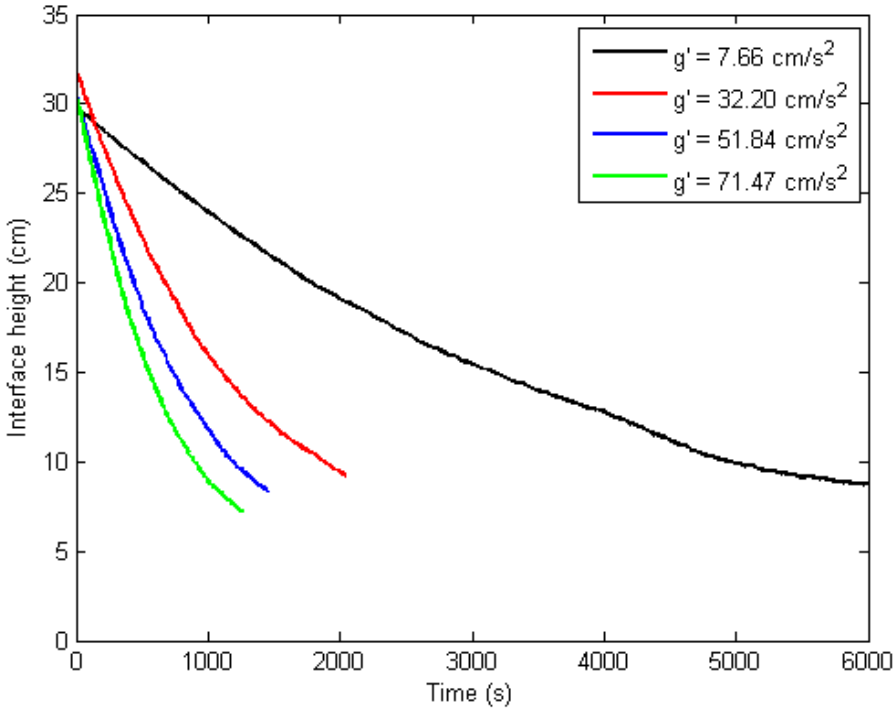

Figure B-1: [color] The draining flow data corresponding to a vent diameter d of 0.14 cm for multiple values of reduced gravity g' where the number of open vents M is 8.

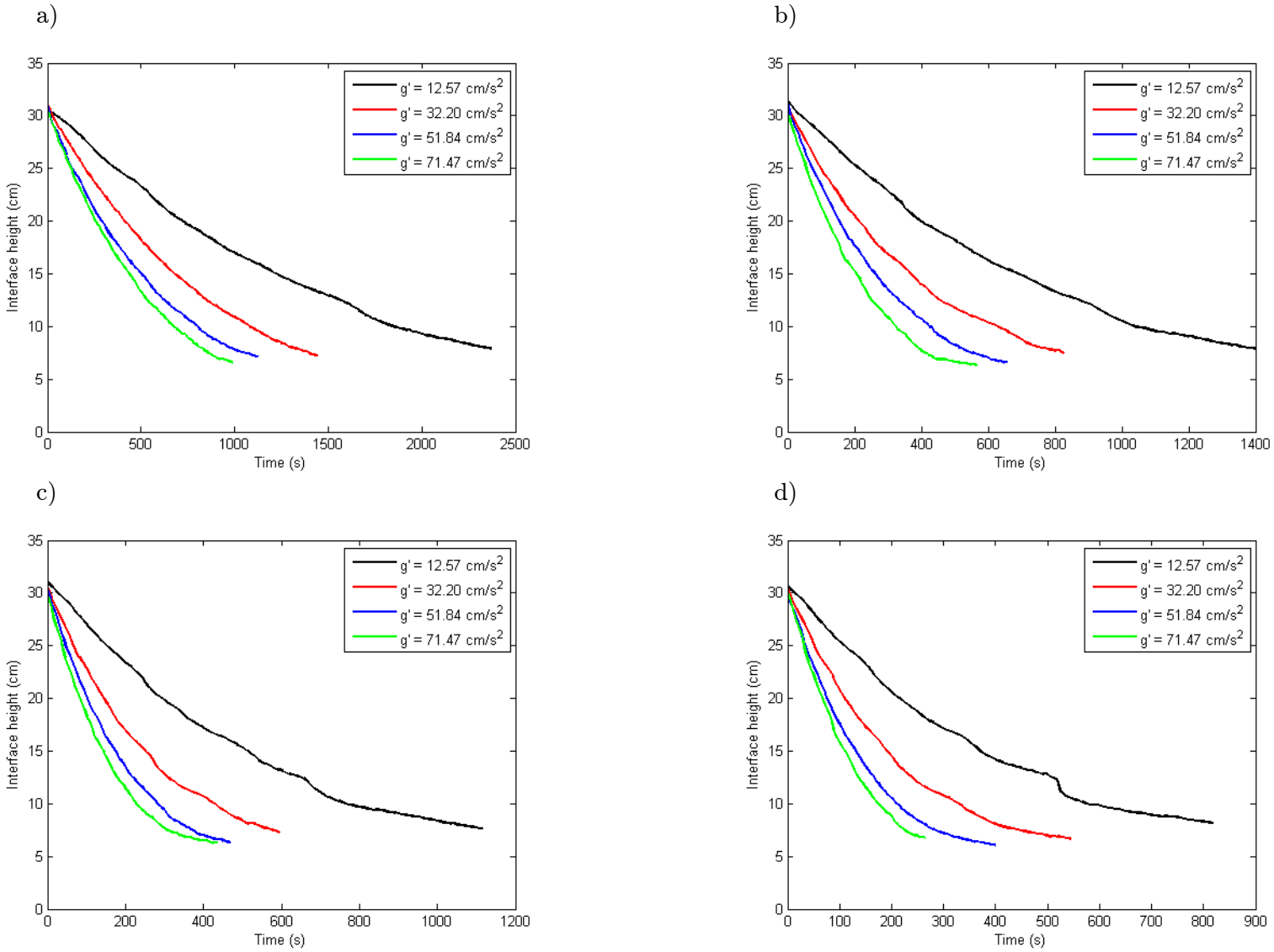

Figure B-2: [color] As in figure B-1, but with $d = 0.32$ cm.

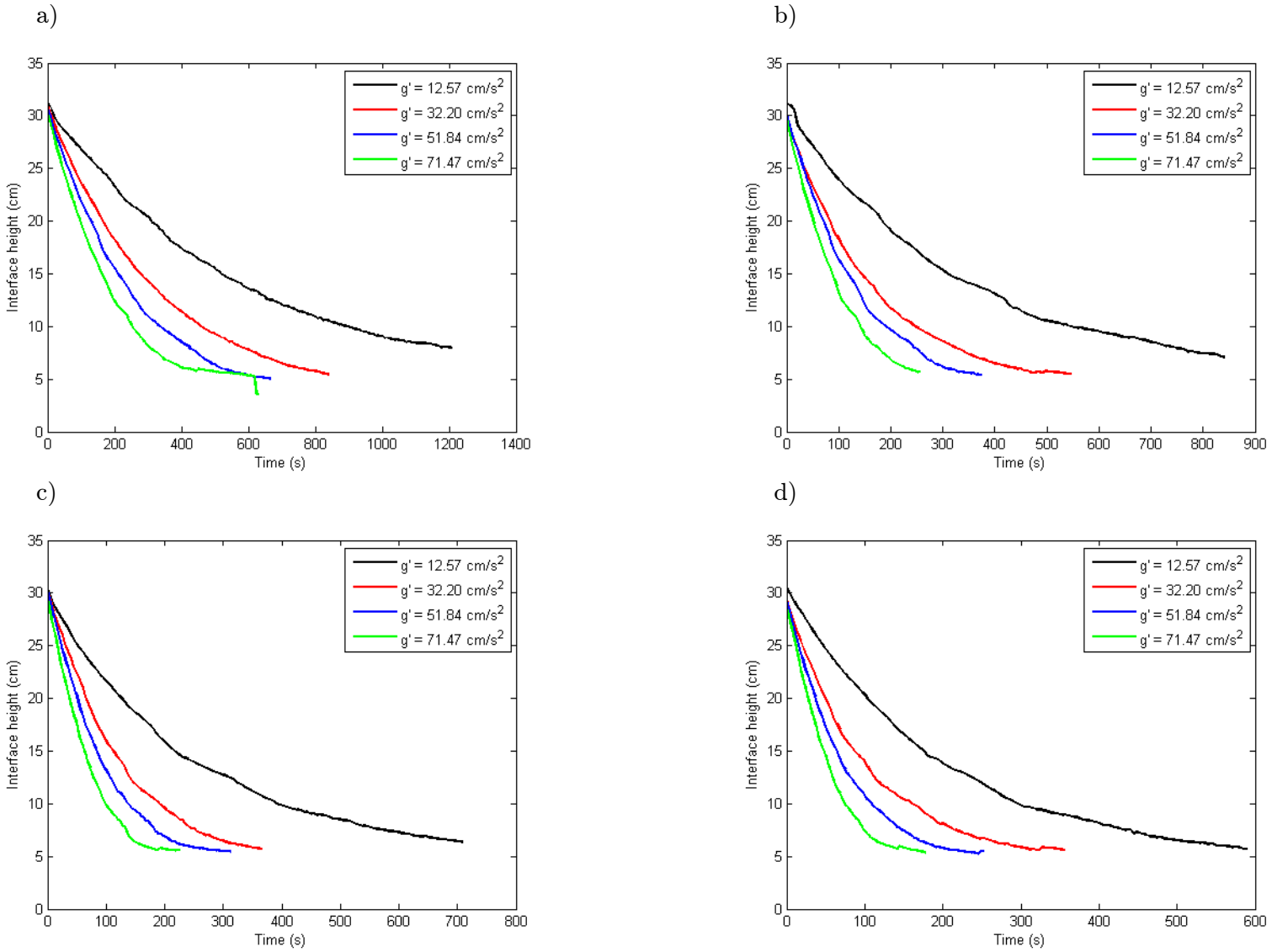

Figure B-3: [color] As in figure B-2, but with $d = 0.48$ cm.

B.1.2 Filling box

Table B-1: The non-dimensional interface height $\xi = h/H$ for the order-1-Re line source for $Q_o = 0.1$ mL/s.

	$g'(cm/s^2)$				
M	**12.57**	M	**42.02**	M	**71.47**
3	0.94±0.02	**2**	0.91±0.02	**2**	0.90±0.02
4	0.87±0.02	**4**	0.81±0.02	**4**	0.78±0.02
6	0.78±0.02	**6**	0.73±0.02	**6**	0.70±0.02
8	0.66±0.02	**8**	0.65±0.02	**8**	0.61±0.02

Table B-2: As in table B-1, but with an order-100-Re point source.

		$g'\ (cm/s^2)$					
		12.57	**42.02**	**71.47**	M		
$Q_o\ (mL/s)$	**1.0**	0.78±0.02	0.78±0.02	0.54±0.02	**2**	**0.48**	$d\ (cm)$
		0.46±0.02	0.58±0.02	0.31±0.02	**4**		
		0.32±0.02	0.40±0.02	0.22±0.02	**6**		
		0.22±0.02	0.26±0.02	0.14±0.02	**8**		
	2.0	0.85±0.02	0.72±0.02	0.69±0.02	**2**		
		0.57±0.02	0.47±0.02	0.44±0.02	**4**		
		0.37±0.02	0.34±0.02	0.36±0.02	**6**		
		0.23±0.02	0.26±0.02	0.28±0.02	**8**		
	1.0	0.93±0.02	0.92±0.02	0.84±0.02	**2**	**0.32**	
		0.72±0.02	0.72±0.02	0.82±0.02	**4**		
		0.58±0.02	0.60±0.02	0.62±0.02	**6**		
		0.48±0.02	0.48±0.02	0.50±0.02	**8**		
	2.0	1.00±0.02	0.93±0.02	0.85±0.02	**2**		
		0.89±0.02	0.80±0.02	0.79±0.02	**4**		
		0.69±0.02	0.66±0.02	0.74±0.02	**6**		
		0.58±0.02	0.57±0.02	0.56±0.02	**8**		

Experiments pertaining to $g' = 12.57$ cm/s^2 and $g' = 27.29$ cm/s^2 for $Q_o =$ 2.5 mL/s were never completed due to the thick lower layer depths that would have been realized. Thus the dense layer would have overflowed through the upper openings of the research box.

Table B-3: As in table B-2, but with an order-500-Re point source and $d = 0.32$ cm.

		g' (cm/s^2)					
		12.57	**27.29**	**42.02**	**56.75**	**71.47**	M
Q_o (mL/s)	**1.0**	0.88±0.02	0.83±0.02	0.84±0.02	0.79±0.02	0.69±0.02	**2**
		0.70±0.02	0.64±0.02	0.65±0.02	0.56±0.02	0.53±0.02	**4**
		0.57±0.02	0.53±0.02	0.48±0.02	0.48±0.02	0.39±0.02	**6**
		0.50±0.02	0.43±0.02	0.42±0.02	0.40±0.02	0.38±0.02	**8**
	1.5	0.90±0.02	0.89±0.02	0.83±0.02	0.83±0.02	0.81±0.02	**2**
		0.67±0.02	0.67±0.02	0.63±0.02	0.63±0.02	0.60±0.02	**4**
		0.52±0.02	0.55±0.02	0.49±0.02	0.53±0.02	0.51±0.02	**6**
		0.46±0.02	0.47±0.02	0.42±0.02	0.43±0.02	0.37±0.02	**8**
	2.0	1.00±0.02	0.99±0.02	0.98±0.02	0.97±0.02	0.87±0.02	**2**
		0.77±0.02	0.73±0.02	0.75±0.02	0.76±0.02	0.68±0.02	**4**
		0.64±0.02	0.60±0.02	0.61±0.02	0.70±0.02	0.53±0.02	**6**
		0.53±0.02	0.49±0.02	0.53±0.02	0.53±0.02	0.42±0.02	**8**
	2.5	-	-	1.00±0.02	0.92±0.02	0.89±0.02	**2**
		-	-	0.75±0.02	0.75±0.02	0.73±0.02	**4**
		-	-	0.65±0.02	0.62±0.02	0.59±0.02	**6**
		-	-	0.56±0.02	0.54±0.02	0.51±0.02	**8**

B.2 Error

The major source of experimental error occurs in the determination of the interface height h by the MATLAB sub-routines discussed in §4 and presented in Appendix D. Here, measurements are complicated by interfacial diffusion between the fresh and salt water layers. According to Kaye et al. (2010), who studied filling box flows in the absence of a porous medium, this diffusion is counterbalanced, at steady state, by entrainment into the plume. Because the entrainment velocity varies with the vertical coordinate, so too must the interface thickness. This observation is consistent with the experimental results presented above. More specifically, we find that, in general the interface thickness is larger at lower values of the interface height h and smaller at higher values of h.

Using the sub-routines in §4 we estimated h, shown in red in figure B-4, and the thickness of the interface, shown in yellow, for various values of M. We then added and subtracted, respectively, the upper and lower bounds of the interface thickness to/from h to determine the positive and negative error. Due to the extensive amounts of data collected, it was impractical to perform this type of analysis in every instance and so we instead focused our attention on various representative experiments from which estimates of the average interface thickness were obtained. In this spirit, the positive and negative errors were individually averaged for all representative images over the range of applicable M. On this basis, we estimate that our measurements of h are accurate to within $\pm$ 0.7 cm. By extension and incorporating this information into (2.24), the error associated with our estimates for k_f/ϕ is calculated to be 5×10^{-5} cm^2.

Similarly to Kaye et al. (2010), our error estimates vary with M and by extension, x.

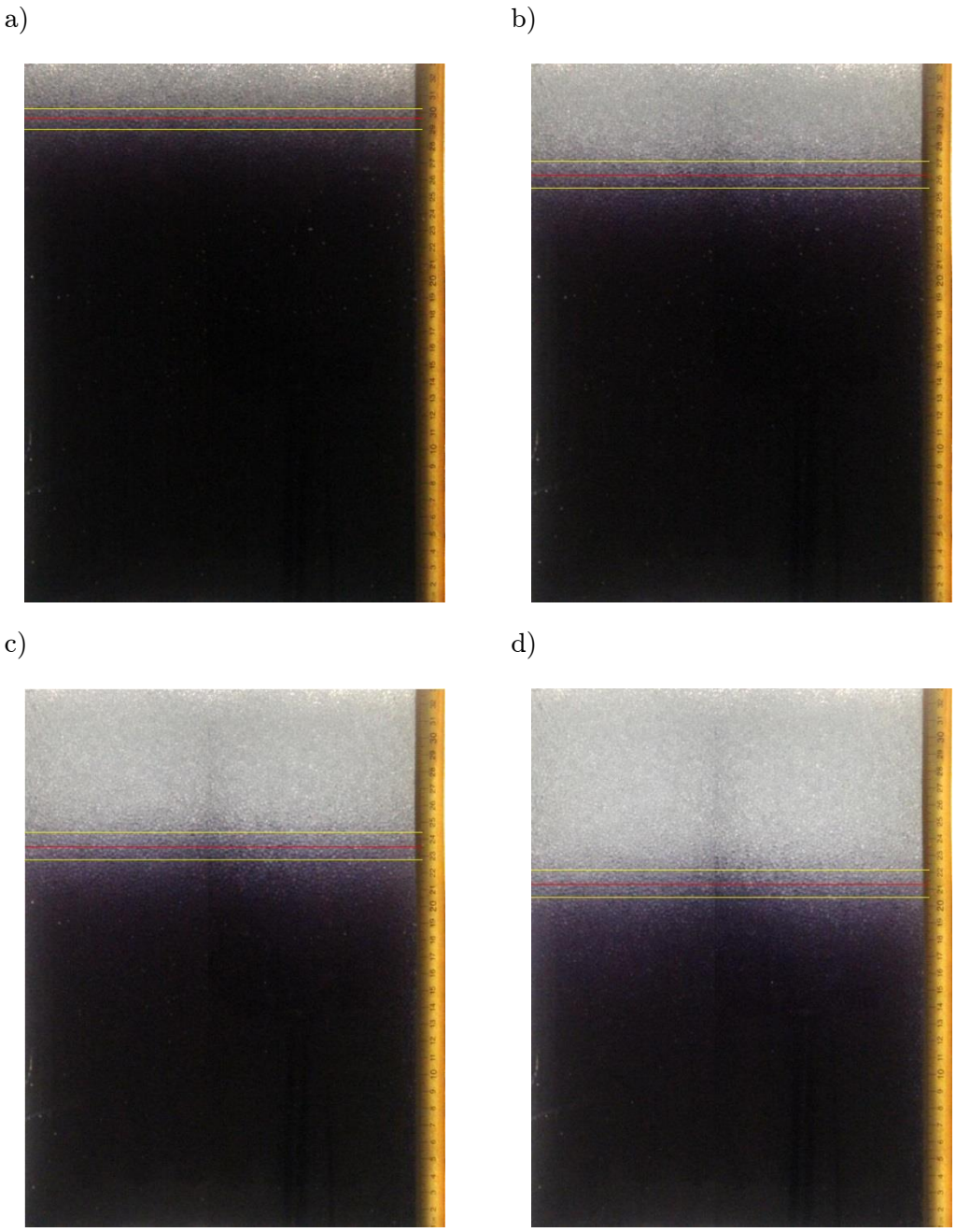

Figure B-4: [color] The estimated interface height h shown in red and the estimated interface thickness shown in yellow. Here the experimental parameters are Q_o = 0.1 mL/s, d_{bead} = 0.3 cm, d = 0.14 cm and (a) M = 2; (b) M = 4; (c) M = 6; and (d) M = 8.

B.3 Calibration

The flow meter described in §3.2 contained equidistant gradations R_f on the side that were previously calibrated for pure water. A calibration needed to be completed for a denser fluid so that a volumetric flow rate corresponding to the appropriate reading could be ascertained. The measurement instruments used for calibration that were not previously described in §3.2.1 include an Acculab digital balance with a resolution of 0.01 g, a PT Fitness digital stopwatch with a resolution of 1 ms and an empty plastic bottle that had a dry mass m_b of 13.15 g. Three measurements were performed for three values of ρ_c. The bottle was thoroughly washed and dried after each measurement.

The flow meter reading was kept constant and fluid was collected in the plastic bottle over approximately 122 s. The flow meter reading was recorded, as was the time of collection t_c. The total mass of the bottle and collected fluid m_t were then measured using the digital balance and the density ρ_c of the collected fluid was measured using the densitometer (§3.1). From m_t, m_c, ρ_c and Δt_c, a flow rate $\dot{Q}_c$ could be calculated using

$$\frac{(m_t - m_c)}{\rho_c t_c} = \dot{Q}_c \,. \qquad \text{B.1}$$

The readings could then be associated with $\dot{Q}_c$ for a specific ρ_c. The results are shown in table B-4.

Table B-4: Calibration measurements for the flow meter.

$(m_t - m_c)\ (g)$	$\rho_c\ (g/L)$	$t_c\ (s)$	$Q_c\ (mL/s)$	R_f
12.28±0.01	1.0112±0.0001	122.66±0.01	0.10±0.01	0.7±0.1
11.21±0.01	1.0111±0.0001	121.85±0.01	0.09±0.01	0.7±0.1
12.49±0.01	1.0112±0.0001	122.34±0.01	0.10±0.01	0.7±0.1
12.52±0.01	1.0413±0.0001	122.66±0.01	0.10±0.01	0.8±0.1
11.70±0.01	1.0412±0.0001	122.09±0.01	0.09±0.01	0.8±0.1
12.67±0.01	1.0410±0.0001	122.91±0.01	0.10±0.01	0.8±0.1
12.42±0.01	1.0709±0.0001	122.13±0.01	0.10±0.01	0.9±0.1
12.30±0.01	1.0711±0.0001	122.21±0.01	0.09±0.01	0.9±0.1
13.54±0.01	1.0710±0.0001	122.73±0.01	0.10±0.01	0.9±0.1

B.4 Salt table

Table B-5 was used to determine the mass of salt, in grams per litre of solution that was needed to achieve a desired saline density. It has been adapted from the Haynes (2011).

Table B-5: Salt table displaying concentration of salt required to obtain the respective saline density.

$\rho_s\ (g/cm^3)$	$C\ (g/L)$	$\rho_s\ (g/cm^3)$	$C\ (g/L)$
0.9989	1.0	1.0333	50.6
0.9997	2.0	1.0340	51.7
1.0004	3.0	1.0355	53.8
1.0011	4.0	1.0369	56.0
1.0018	5.0	1.0384	58.1
1.0025	6.0	1.0398	60.3
1.0032	7.0	1.0413	62.5
1.0039	8.0	1.0427	64.6
1.0046	9.0	1.0442	66.8
1.0053	10.1	1.0456	69.0
1.0060	11.1	1.0471	71.2
1.0068	12.1	1.0486	73.4
1.0075	13.1	1.0500	75.6
1.0082	14.1	1.0515	77.8

Table B-5: Continued.

$\rho_s\ (g/cm^3)$	$C\ (g/L)$	$\rho_s\ (g/cm^3)$	$C\ (g/L)$
1.0089	15.1	1.0530	80.0
1.0096	16.2	1.0544	82.2
1.0103	17.2	1.0559	84.5
1.0110	18.2	1.0574	86.7
1.0117	19.2	1.0588	88.9
1.0125	20.2	1.0603	91.2
1.0132	21.3	1.0618	93.4
1.0139	22.3	1.0633	95.7
1.0146	23.3	1.0647	98.0
1.0153	24.4	1.0662	100.2
1.0160	25.4	1.0677	102.5
1.0168	26.4	1.0692	104.8
1.0175	27.5	1.0707	107.1
1.0182	28.5	1.0744	112.8
1.0189	29.5	1.0781	118.6
1.0196	30.6	1.0819	124.4
1.0203	31.6	1.0857	130.3
1.0211	32.7	1.0894	136.2
1.0218	33.7	1.0932	142.1
1.0225	34.8	1.0970	148.1
1.0232	35.8	1.1008	154.1
1.0239	36.9	1.1047	160.2
1.0246	37.9	1.1085	166.3
1.0254	39.0	1.1162	178.6
1.0261	40.0	1.1240	191.1
1.0268	41.1	1.1319	203.7
1.0275	42.1	1.1398	216.6
1.0282	43.2	1.1478	229.6
1.0290	44.2	1.1558	242.7
1.0297	45.3	1.1640	256.1
1.0304	46.4	1.1721	269.6
1.0311	47.4	1.1804	283.3
1.0318	48.5	1.1887	297.2
1.0326	49.6	1.1972	311.3

*Pure water at 20 ˚C has a density of 0.9982 g/cm^3

Appendix C

Nozzle schematics & discussion

The three nozzles that are discussed in §3.1.4 and are shown in figure 3-8 were designed with special consideration regarding the conditions at which the saline fluid exited the nozzle.

The first nozzle used in experiments was the order-500-Re point source (see figures C-1 to C-5 of §C.1 below) where the design, see figure C-1, was adapted from the nozzle discussed by Hunt and Linden (2001). As indicated by figure C-2, a throat of diameter 0.2 cm is used to reduce the inertia of the incoming saline fluid which then enters the lower vertical cylindrical chamber of diameter 1.0 cm and height 3.4 cm. From the lower chamber, the fluid exits the nozzle through a hole of diameter 0.5 cm in the 'screw-on' bottom component shown in figure C-5. The inside of this bottom component contains a #60 aluminum mesh to filter out any unwanted particles that may be inadvertently supplied from the overhead reservoir. The assembled nozzle (figure C-3) was connected together by mating the bottom component (figure C-5) and the top component (figure C-4) and locking the bottom component in place by turning it clockwise approximately 30°. With a bead diameter d_{bead} of 0.5 cm and the range of

source volume fluxes Q_o shown in table B-3, the Reynolds number Re, defined by,

$$Re = \frac{Q_o d_{bead}}{\nu A_{slit}}, \tag{3.1}$$

associated with this nozzle ranges from 255 to 637.

The second nozzle was the order-100-Re line source (see figures C-6 to C-10 of §C.2 below) which was smaller than the order-500-Re point source e.g. it had a comparable throat of diameter 0.2 cm and a lower horizontal cylindrical chamber of diameter 0.9 cm and length 7.1 cm, that spanned the depth of the research box (figure C-7). Inside the chamber was a plastic drinking straw cut to size and wrapped in #60 aluminum mesh. The straw and mesh were used to filter out particles and distribute the incoming fluid laterally so the exiting fluid would form a uniform line plume along the 7.1 cm long and 0.1 cm wide opening. The assembled nozzle (figure C-8) was constructed by gluing the main and secondary components, shown in figure C-9 and C-10 respectively, together using plastic cement. Re for this nozzle ranges from 70.4 to 141 using d_{bead} of 0.5 cm and the multiple values of Q_o shown in table B-2.

Lastly, the third nozzle was the order-1-Re line source (see figures C-11 to C-17 of §C.3 below) and is slightly more complex in its function. The main purpose of this nozzle was to minimize the Re as much as possible while maintaining a uniform flow from the nozzle. Similar to the previous two nozzles, the order-1-Re line source contains a cylindrical chamber of diameter 0.5 cm and length 7.1 cm. As shown in figure C-12, a rectangular slit that is 0.8 cm long and 0.15 cm wide connects the neck of the nozzle to the bottom of the chamber. This design allows for the

incoming saline fluid to enter the nozzle and feed into the bottom of the chamber. Here, as the chamber continuously fills, the fluid flows laterally until it overflows. A similar slit that is 7.1 cm long and 0.15 cm wide connects the top of the chamber to the 7.1 cm long and 0.4 cm wide rectangular opening by which overflowing saline fluid from the chamber exits the nozzle. A small 0.5 cm by 0.5 cm by 7.1 cm strip from a dish sponge was inserted in the exit opening and used to filter out particles and act as a diffuser; to ensure that the plume volume flux was uniform along its length. The top component was assembled by mating the male and female teeth of the main top component (figure C-14) and the secondary top component (figure C-16). The bottom component was assembled by, again, mating the teeth of the main bottom component (figure C-15) and secondary bottom component (figure C-17). The final product (figure C-13) was then constructed by gluing the top and bottom components with plastic cement. This nozzle was used with smaller beads of d_{bead} 0.3 cm and the resulting $Re = 1.06$ when $Q_o = 0.1$ mL/s.

C.1 Order-500-*Re* point source

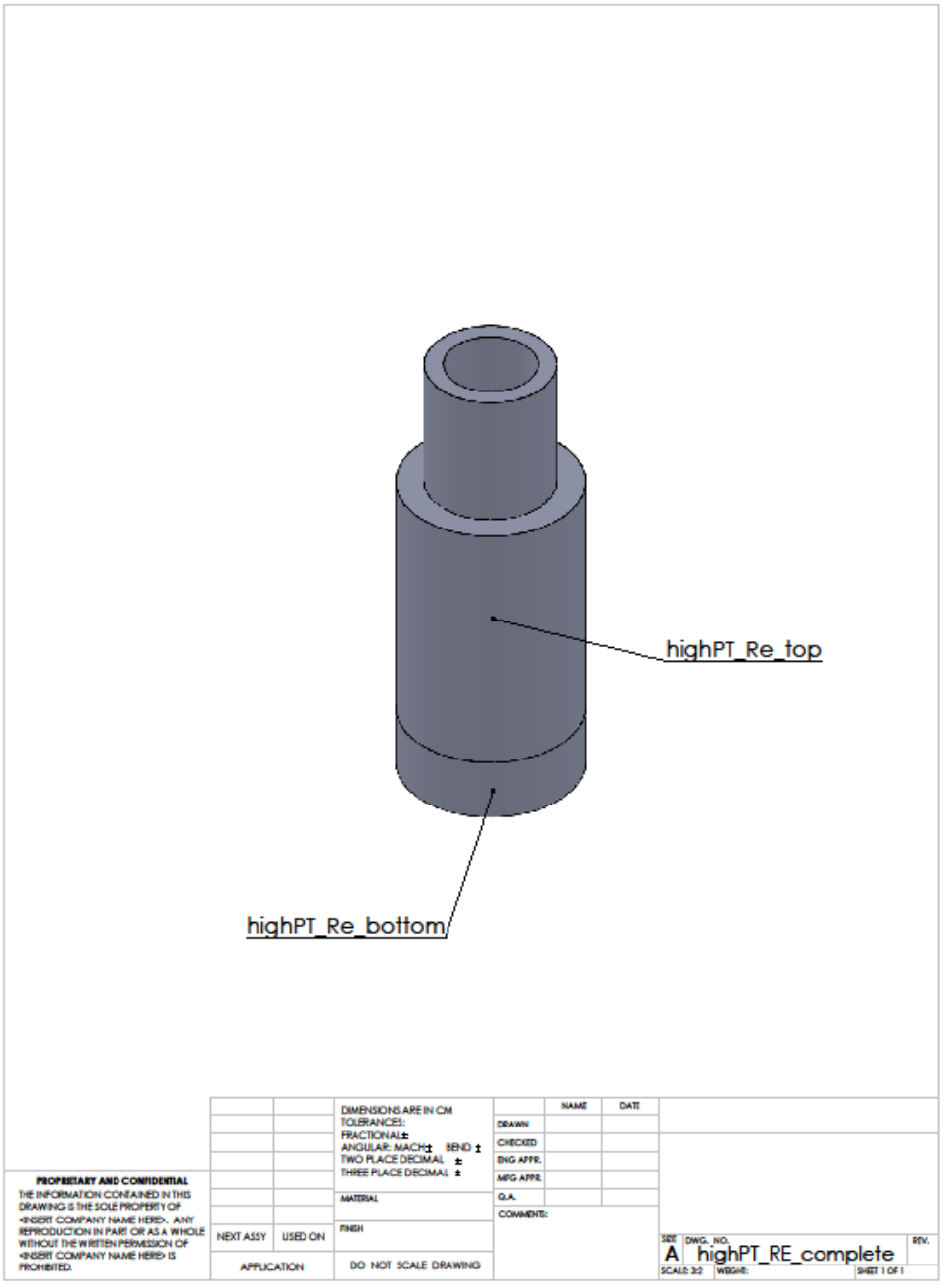

Figure C-1: Isometric assembly drawing of the order-500-*Re* point source containing identification of the individual parts.

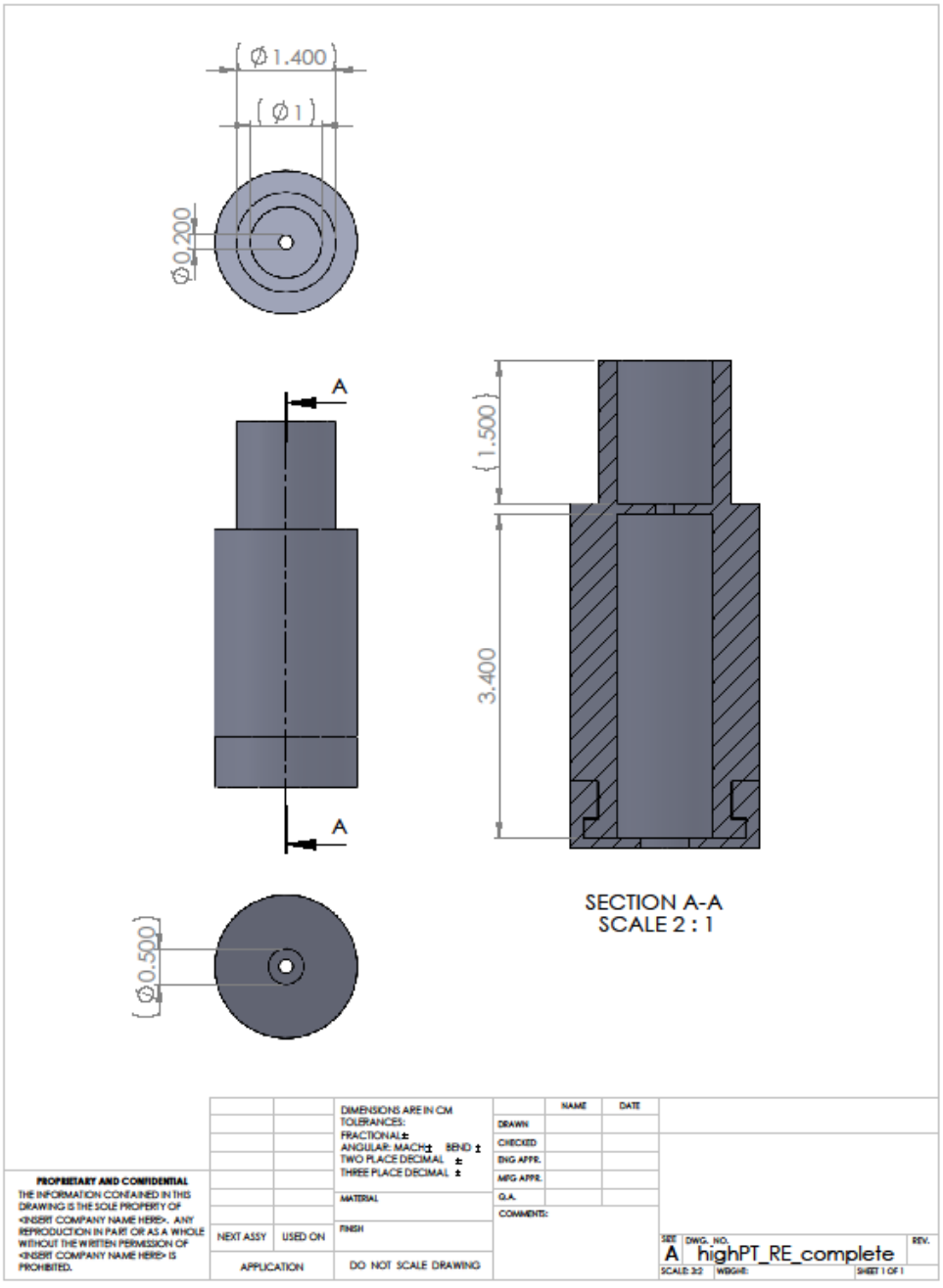

Figure C-2: Front, top and bottom view of the order-500-*Re* point source displaying dimensions and a section view of important features.

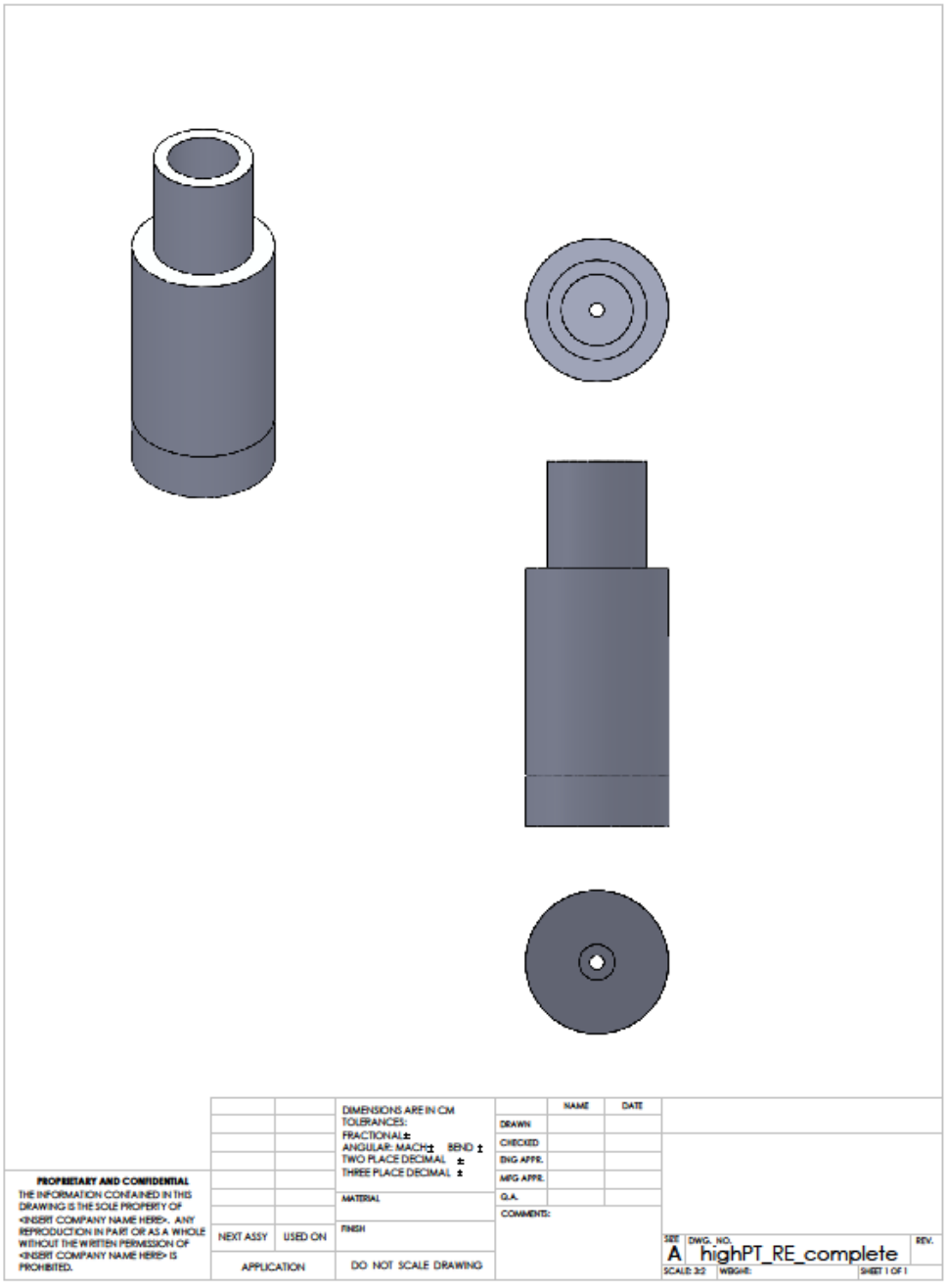

Figure C-3: Front, top, bottom and isometric view of the fully assembled order-500-Re point source.

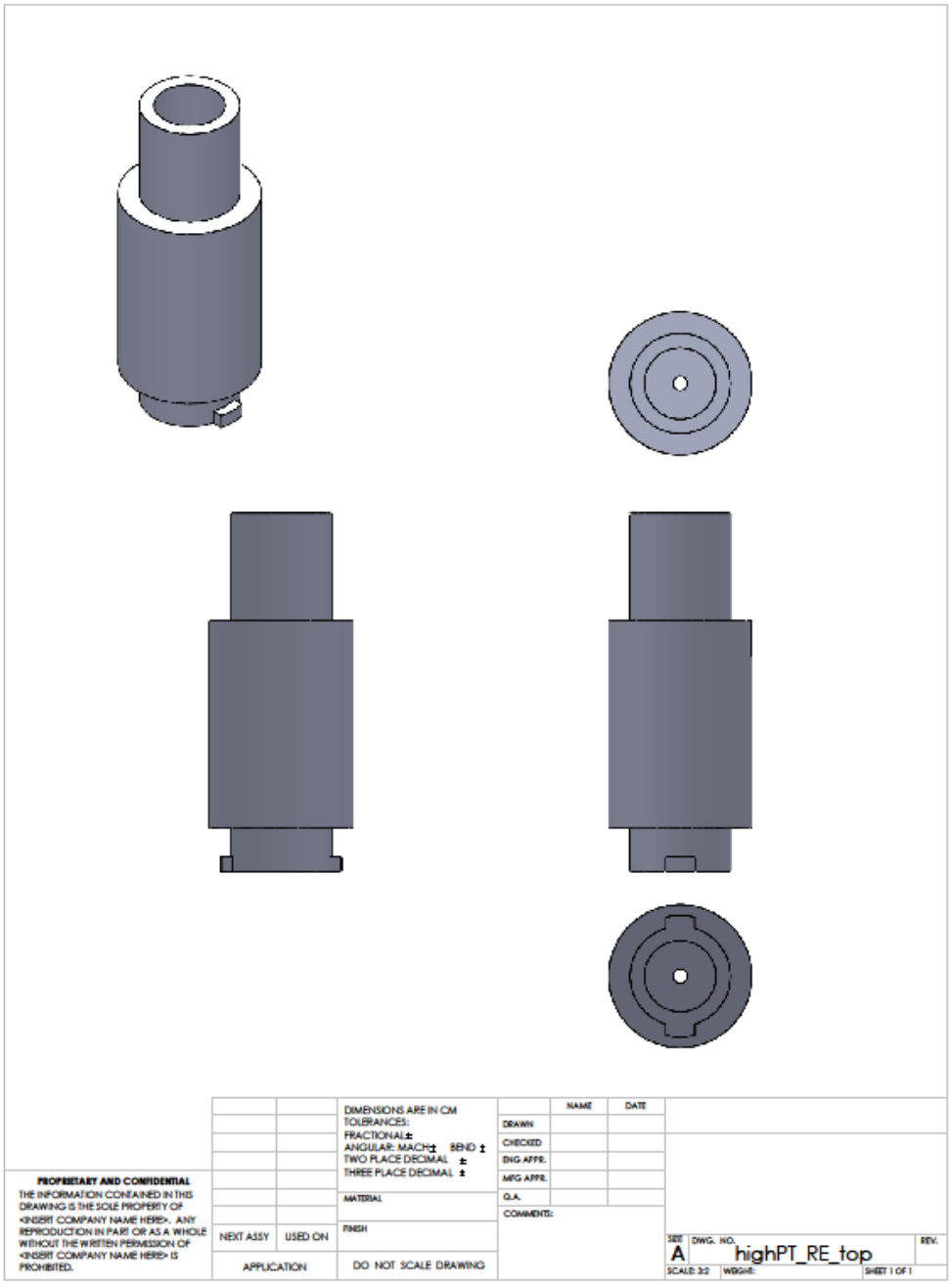

Figure C-4: Front, top, bottom and isometric view of the main top component of the order-500-Re point source. Dimensions for the notches used to attach the main bottom component, shown in figure C-5, were omitted because the method used to connect the main top and main bottom component was not essential to the nozzle's functionality.

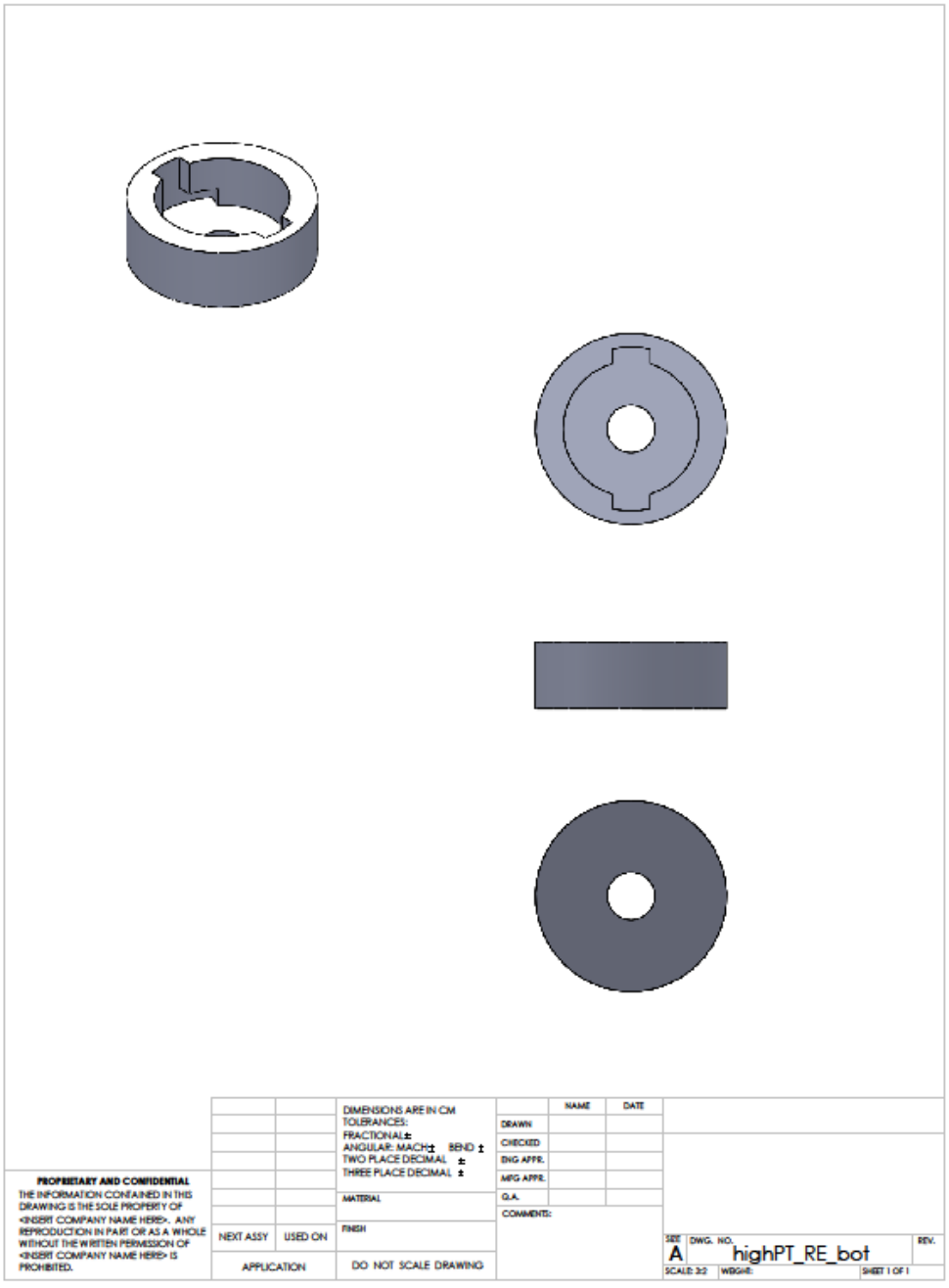

Figure C-5: Front, top, bottom and isometric view of the main bottom component of the order-500-Re point source.

C.2 Order-100-*Re* line source

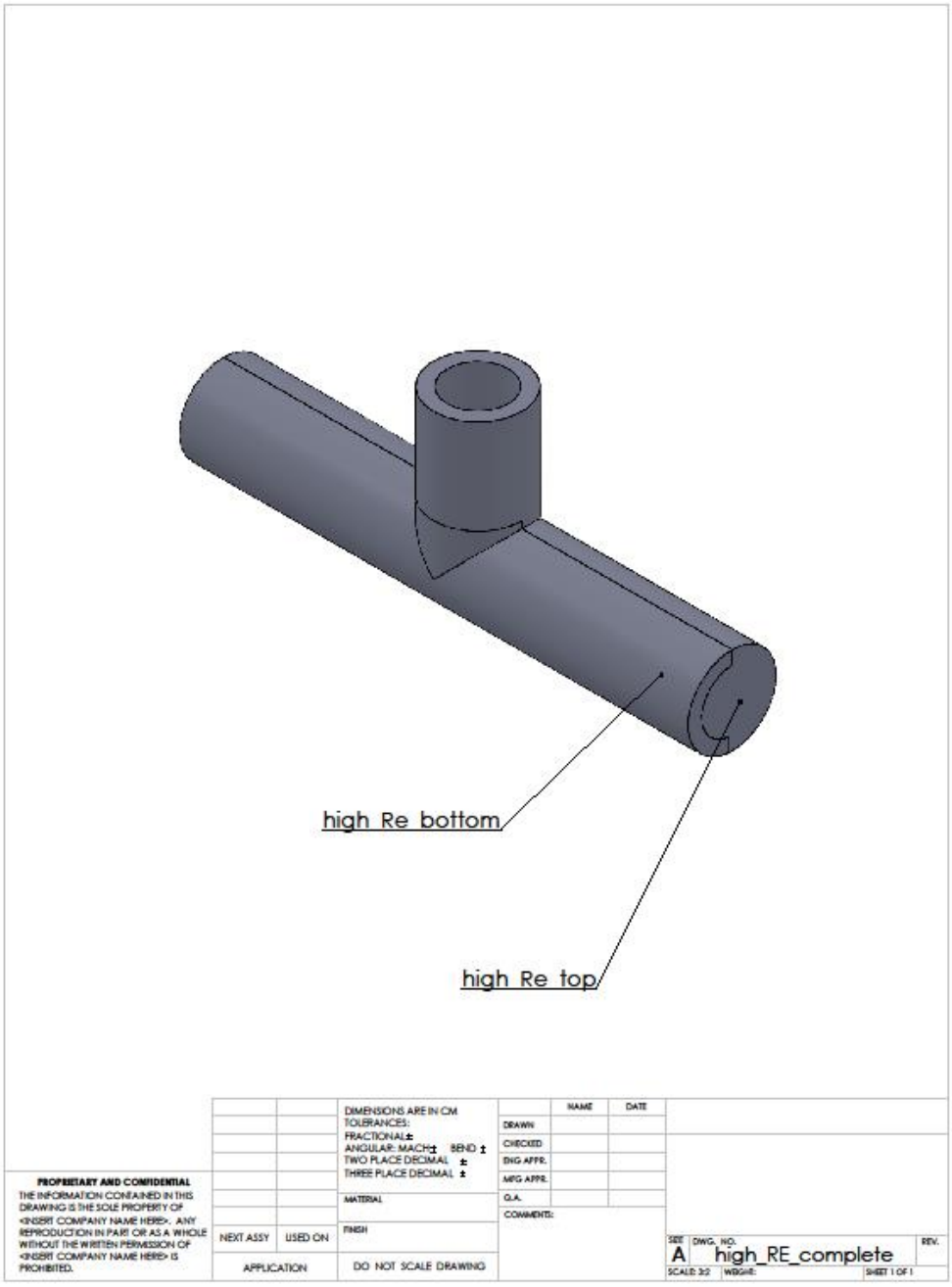

Figure C-6: Isometric assembly drawing of the order-100-*Re* line source containing identification of the individual parts.

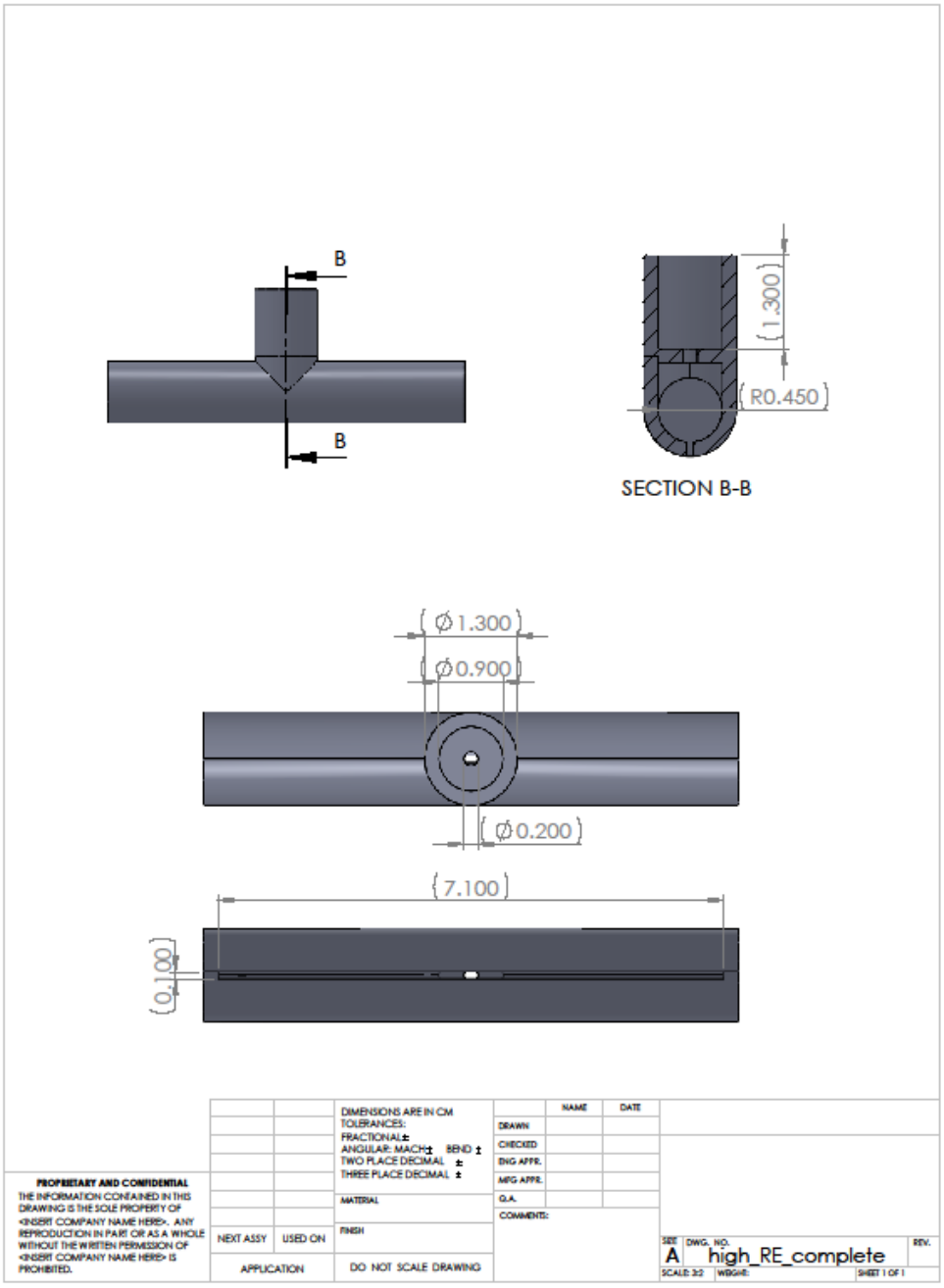

Figure C-7: Front, bottom and side view of the order-100-*Re* line source displaying dimensions and a section view of important features.

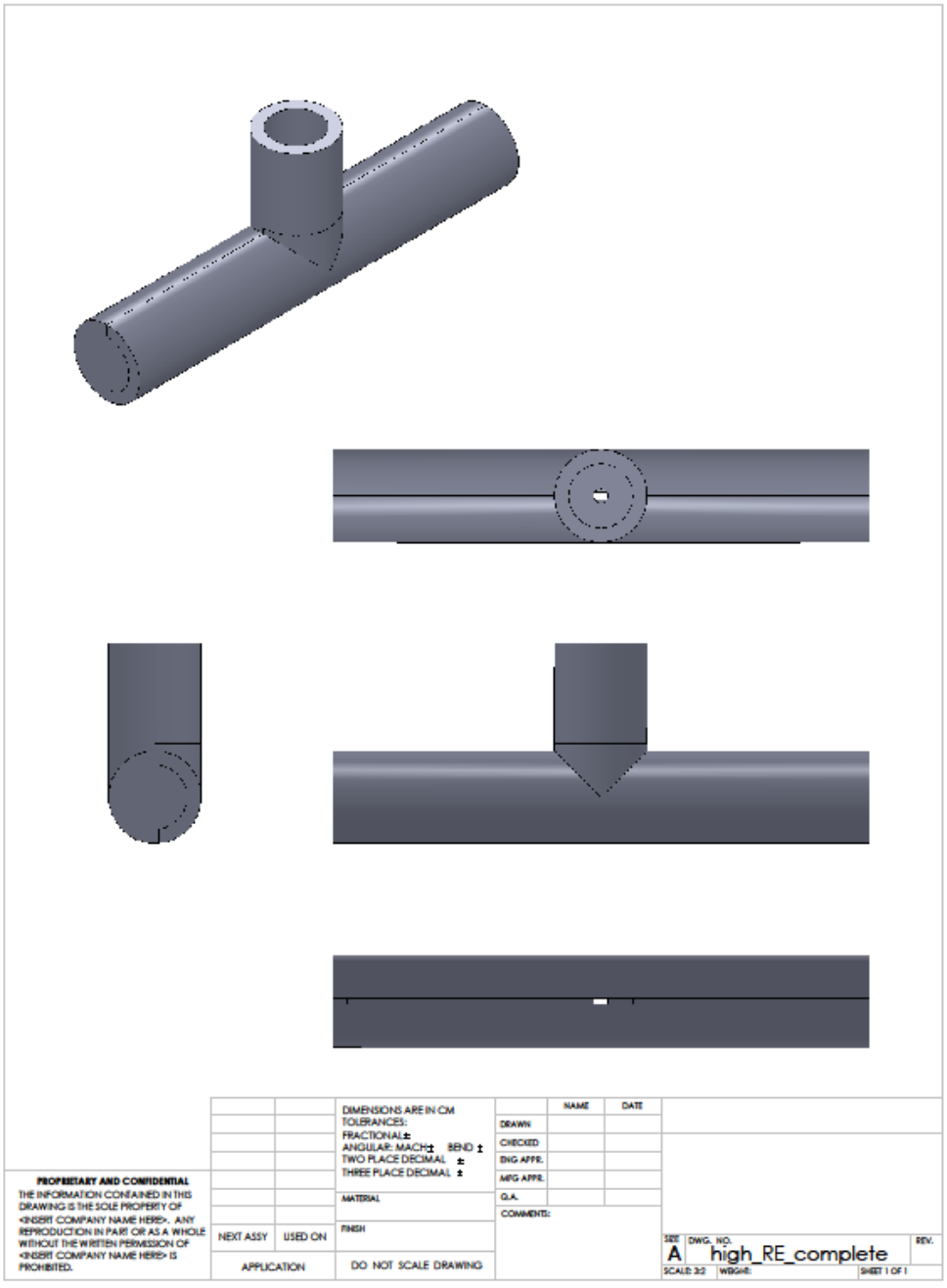

Figure C-8: Front, top, bottom, side and isometric view of the fully assembled order-100-*Re* line source.

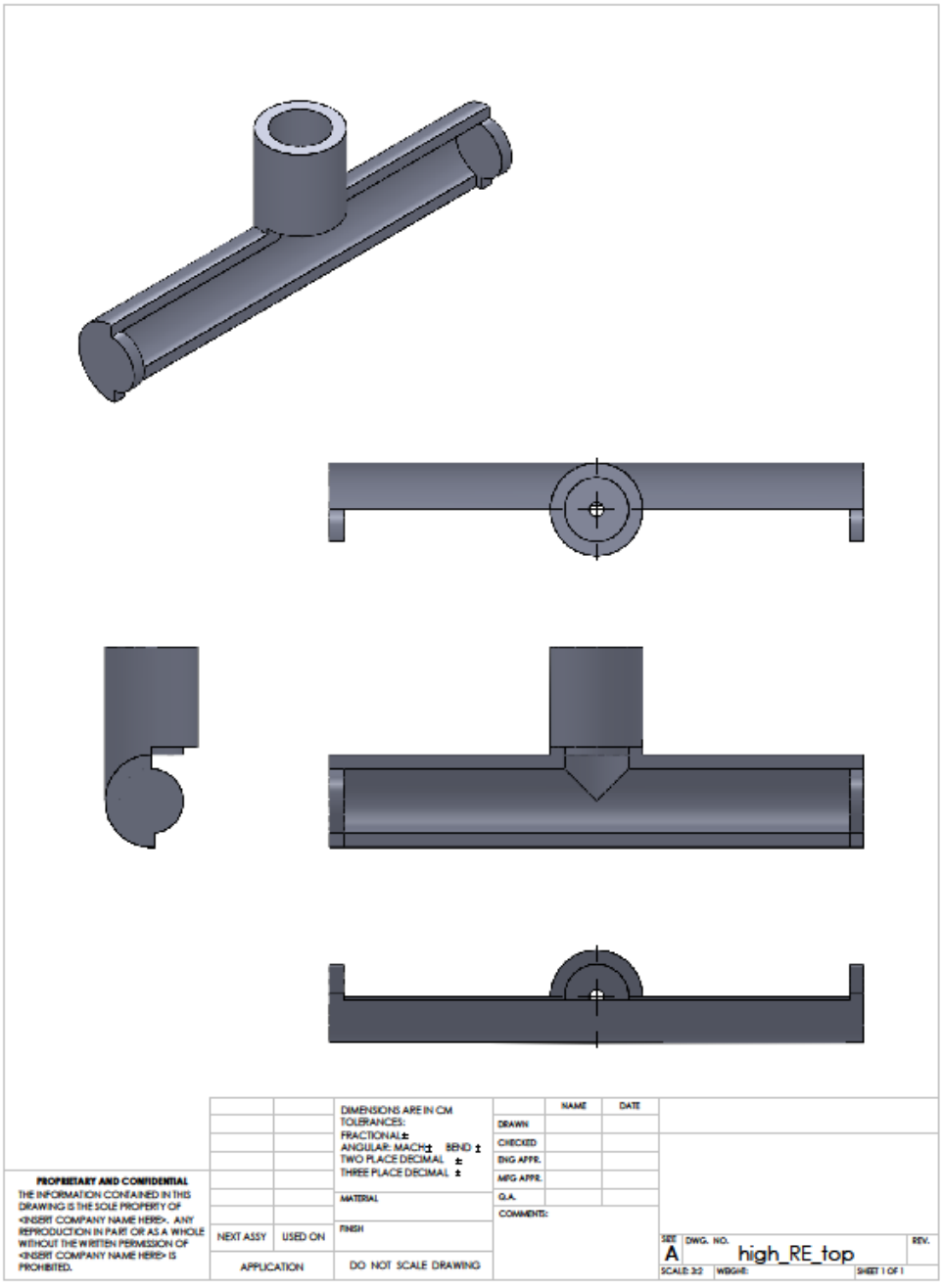

Figure C-9: Front, top, bottom, side and isometric view of the main component of the order-100-Re line source.

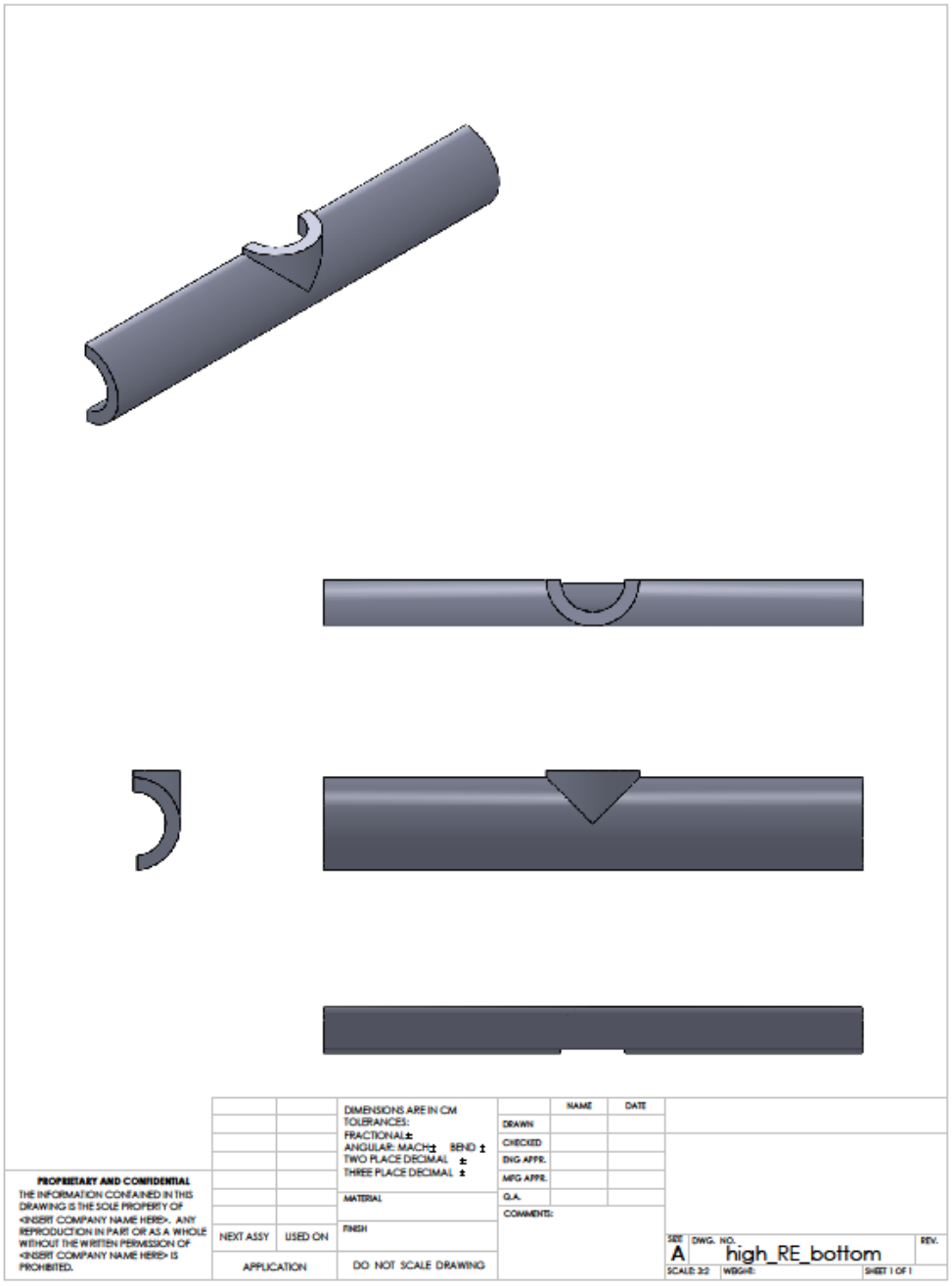

Figure C-10: Front, top, bottom, side and isometric view of the secondary component of the order-100-Re line source.

C.3 Order-1-*Re* line source

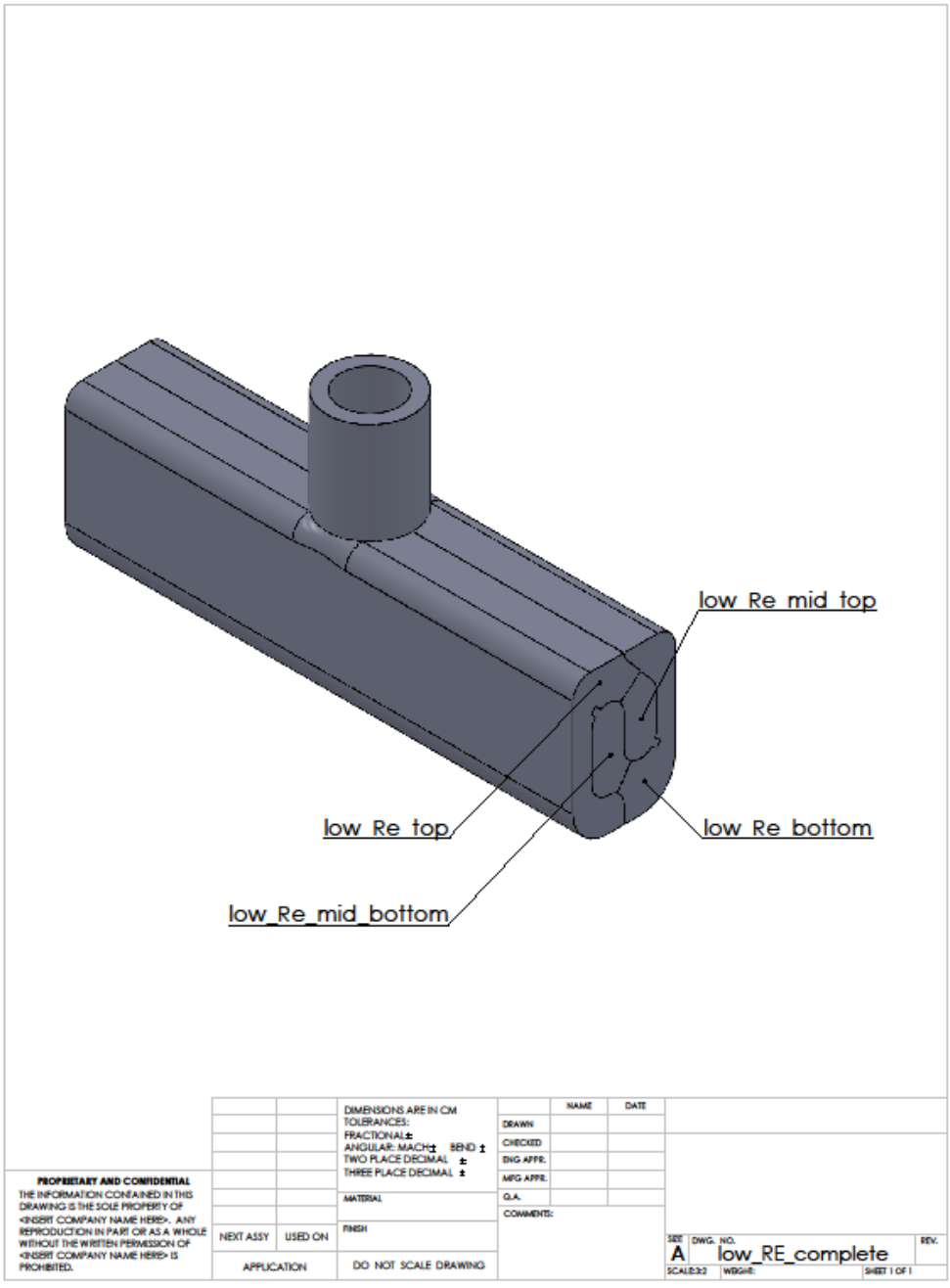

Figure C-11: Isometric assembly drawing of the order-1-*Re* line source containing identification of the individual parts.

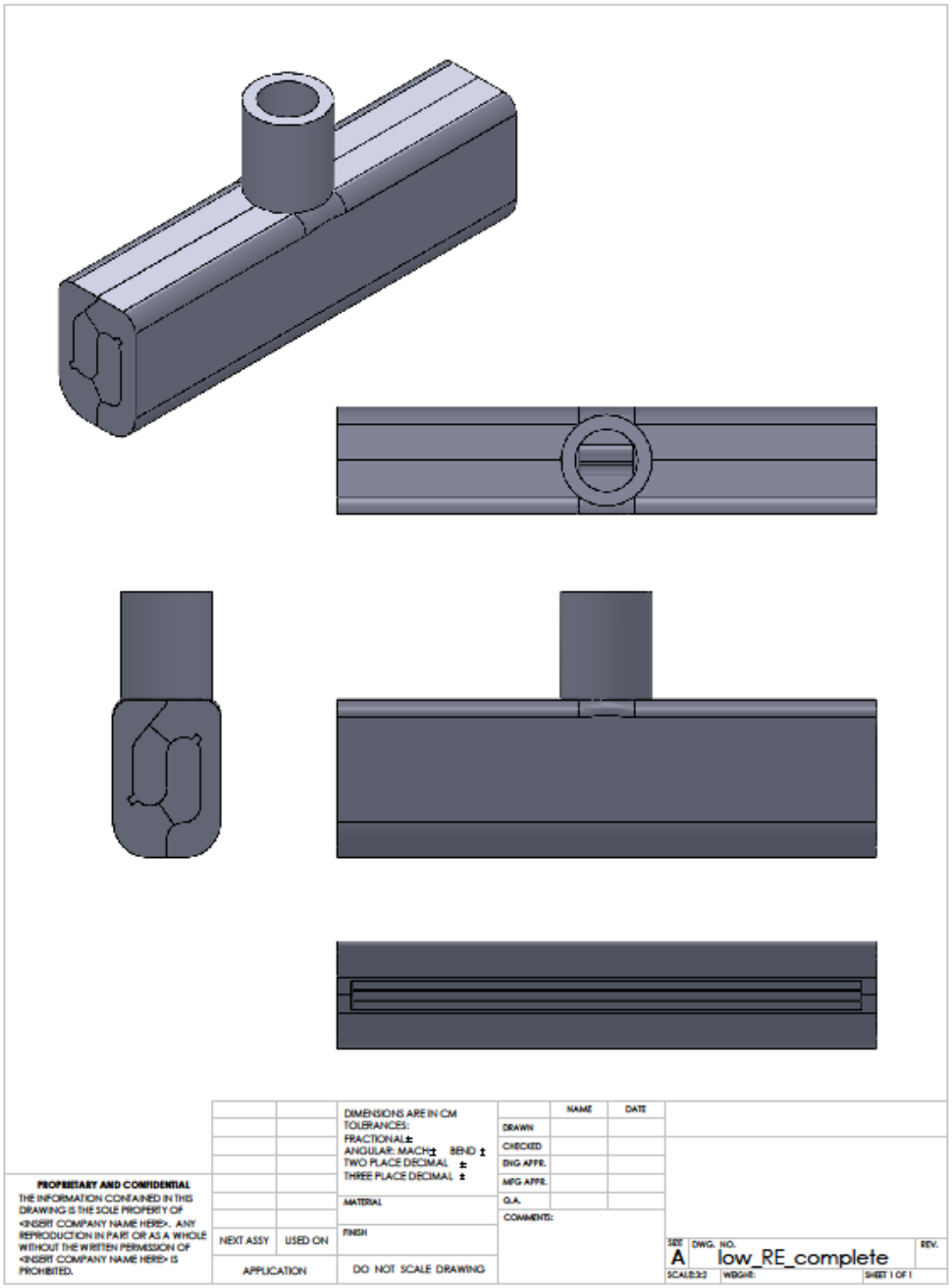

Figure C-12: Top, bottom and side view of the order-1-Re line source displaying dimensions and a section view of important features.

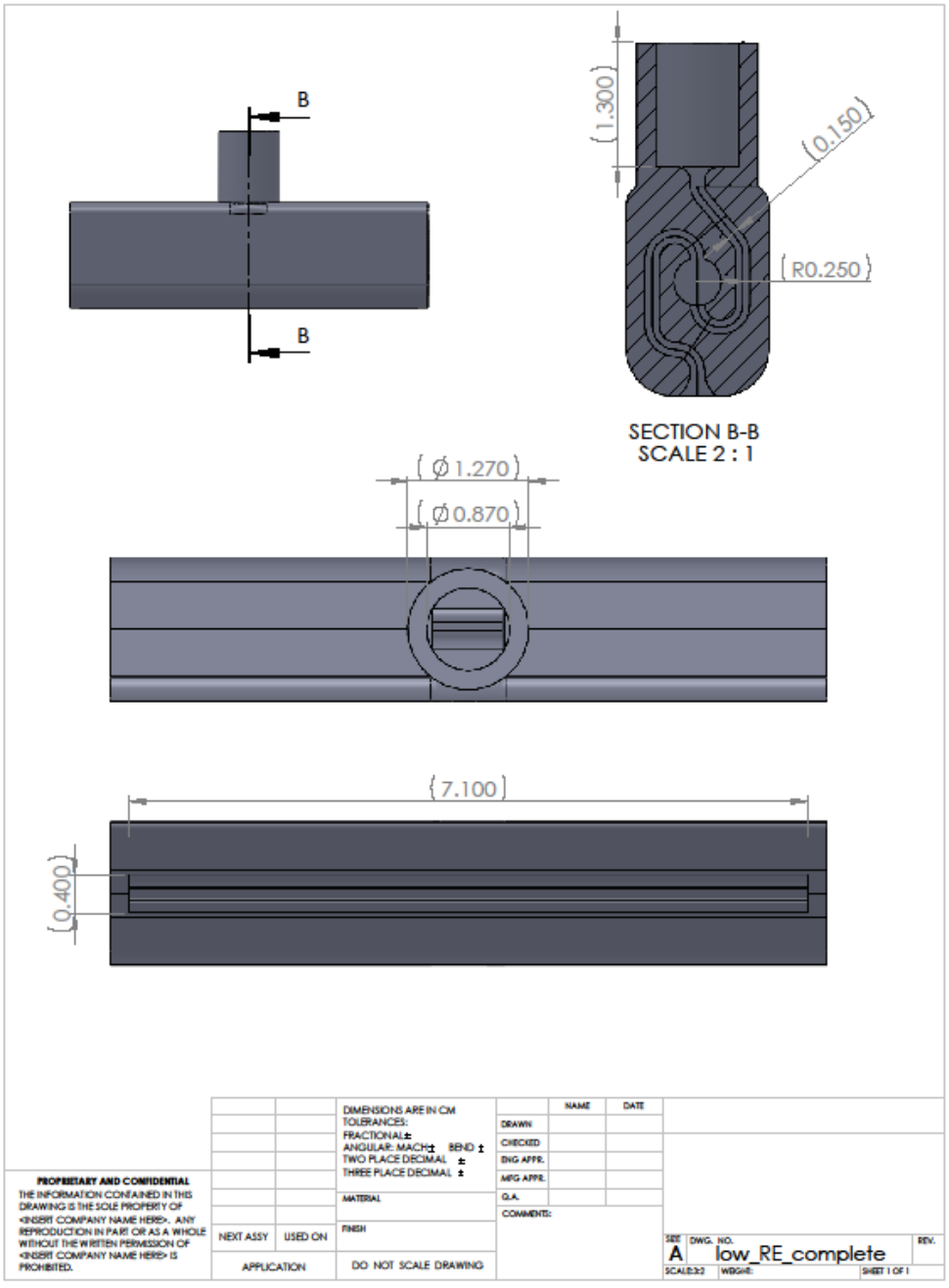

Figure C-13: Front, top, bottom, side and isometric view of the fully assembled order-1-*Re* line source. The strip of foam sponge was inserted into the bottom slit of the nozzle to help maintain a span-wise uniform exit velocity.

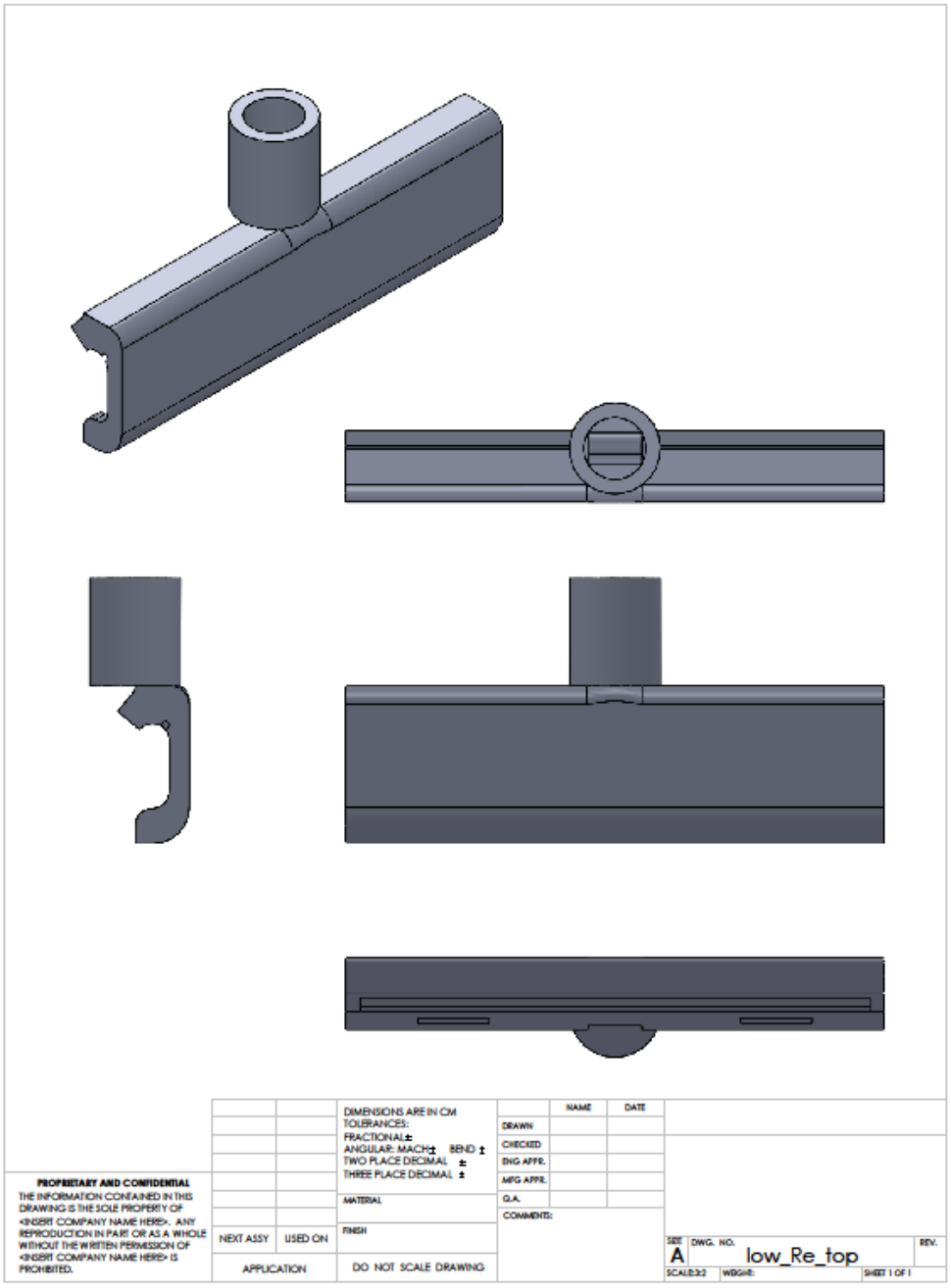

Figure C-14: Front, top, bottom, side and isometric view of the main top component of the order-1-*Re* line source.

Figure C-15: Front, top, bottom, side and isometric view of the main bottom component of the order-1-*Re* line source.

Figure C-16: Front, top, bottom, side and isometric view of secondary top component which is connected to the main top component shown in figure C-14.

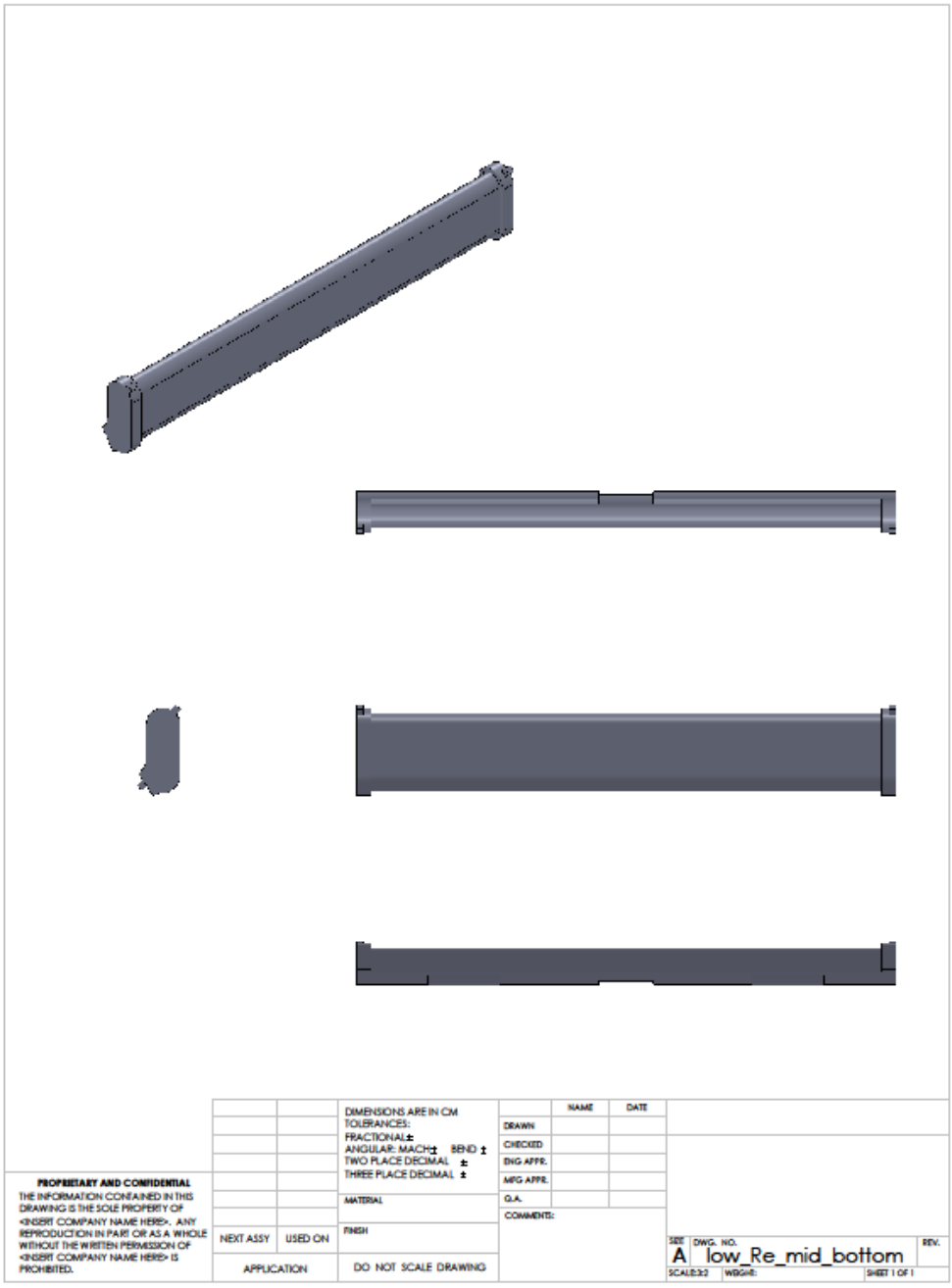

Figure C-17: Front, top, bottom, side and isometric view of secondary bottom component which is connected to the main bottom component shown in figure C-15.

Appendix D

MATLAB code

The following section contains the MATLAB algorithms used when post-processing images and is divided into three sub-sections. Section D.1 is the alteration sub-routine which was discussed in more detail in §4.1. Section D.2 is the estimation and detection sub-routine discussed in §4.2 and §4.3. Lastly, D.3 is the fissure permeability sub-routine discussed in §4.4.

D.1 Alteration sub-routine

```
function FBLine_AlterImage(folder, name)
%This function imports and crops an image. It removes the
%environmental details that are irrelevant to the determination
of the
%interface height. This function is the sub-routine discussed in
§4.1.

    %% This section imports an image in MATLAB for cropping.
    directory = ['C:\Documents and
Settings\mroes\Desktop\Research\Pictures\', folder, '\'];
    excel_name = ['Crop Values.xls'];
    excel_string = [directory, excel_name];
    resize_percent = 0.25;
    image_name = [directory, 'IMG_', name, '.JPG'];
    temp_image = imread(image_name);
    temp_image = im2double(temp_image);
    temp_image = imresize(temp_image, resize_percent);
```

```
    temp_image = imrotate(temp_image, 90);

    total_width = size(temp_image,2);
    total_height = size(temp_image,1);
    rgb = size(temp_image,3);

    %% This section determines if the image is a reference image
or
    %% experimental image. It gets the user-defined coordinates
of the plume
    %% and environmental details to be cropped out. It then saves
them to
    %% an Excel file.
    if name == '0'
        imshow(temp_image);
        [x] = ginput(2);

        cutout_x_pos = floor(x(1,1));
        cutout_x_width = floor(x(2,1) - x(1,1));
        cutout_y_pos = 1;
        cutout_y_height = total_height;
    else
        values = xlsread(excel_string);

        cutout_x_pos = values(1);
        cutout_x_width = values(2);
        cutout_y_pos = values(3);
        cutout_y_height = values(4);
    end

    %% This section removes the nozzle plume.
    for i = cutout_y_pos:cutout_y_height
        for j = (cutout_x_pos + 1):(cutout_x_pos + cutout_x_width
- 1)
            for k = 1:rgb
                temp_image(i,j,k) = 1;
            end
        end
    end

    %% This section combines the section of the image to the left
and to the
    %% right of the nozzle plume in to one continious image.
    left_width = cutout_x_pos;
    right_width = (total_width - (cutout_x_pos +
cutout_x_width));
    for i = cutout_y_pos:cutout_y_height
        for j = cutout_x_pos:(cutout_x_pos + right_width)
            for k = 1:rgb
                temp_image(i,j,k) = temp_image(i,(j +
cutout_x_width),k);
                temp_image(i,(j + cutout_x_width),k) = 1;
            end
        end
    end
    cutout_y_height = total_height;
```

```
    for i = 1:cutout_y_height
        for j = 1:(left_width + right_width)
            for k = 1:rgb
                temp_image(i,j,k) = temp_image(i,j,k);
            end
        end
    end

    image = zeros(floor(cutout_y_height),left_width +
right_width,rgb);

    for i = 1:cutout_y_height
        for j = 1:(left_width + right_width)
            for k = 1:rgb
                image(i,j,k) = temp_image(i,j,k);
            end
        end
    end

    %The following reads or writes the user-defined coordinates,
from above,
    %based on whether the image is a reference image or
experimental image.
    if name == '0'
        imshow(image);
        [x] = ginput(2);

        height = floor(x(2,2) - x(1,2));
        width = floor(x(2,1) - x(1,1));
        crop_topleft_x = floor(x(1,1));
        crop_topleft_y = floor(x(1,2));

        text = {num2str(cutout_x_pos), 'cutout_x_pos';
        num2str(cutout_x_width), 'cutout_x_width';
        num2str(cutout_y_pos), 'cutout_y_pos';
        num2str(cutout_y_height), 'cutout_y_height';
        num2str(height), 'height';
        num2str(width), 'width';
        num2str(x(1,1)), 'crop_topleft_x';
        num2str(x(1,2)), 'crop_topleft_y'};

        xlswrite(excel_string, text);
    else
        values = xlsread(excel_string);

        height = values(5);
        width = values(6);
        crop_topleft_x = values(7);
        crop_topleft_y = values(8);
    end

    %% This section crops out the environmental details around
the research
    %% box and saves the new image.
```

```
    image = imcrop(image, [crop_topleft_x crop_topleft_y width
height]);

    image_string = [directory, 'IMG_', name, '.JPG'];
    imwrite(image,image_string,'jpg')
    imshow(image)
    string = ['IMG_', name, ' cropped...'];
    disp(string);
end
```

D.2 Estimation & detection sub-routine

```
function y_height = DetermineInterfaceHeight(folder,
reference_image, comparitive_image, display_plot, height_unit,
debug)
%This function subtracts two images (reference and experimental)
from each
%other in order to analyze and determine an initial and final
prediction of
%the interface height, h. It contains sub-routines discussed in
§4.2 and §4.3.

    close all

    global rulervalue_top
    global rulervalue_bot

    directory = ['C:\Documents and
Settings\mroes\Desktop\Research\Pictures\', folder, '\'];

    % The following is the reference image being imported.
    ref_name = [directory, 'IMG_', reference_image, '.JPG'];
    ref_image = imread(ref_name);
    ref_image_rgb = im2double(ref_image);
    ref_image = rgb2gray(ref_image_rgb);
%   figure; imshow(ref_image); %Displays the experimental image.

    % The following is the experimental image being imported.
    comp_name = [directory, 'IMG_', comparitive_image, '.JPG'];
    comp_image = imread(comp_name);
    comp_image_rgb = im2double(comp_image);
    comp_image = rgb2gray(comp_image_rgb);
%   figure; imshow(comp_image); %Displays experimental image.

    image = (ref_image - comp_image); %'image' is the subtracted
image.

%   figure; imshow(image); %Displays the subtracted image.

    %% This section is the definition of variables used in this
function.
    width_pixel_group_size = 10; %Pixel group width
    height_pixel_group_size = 10; %Pixel group height
    row_avg = 1;
    screensize = get(0,'ScreenSize');

    height = size(image,1); %Height of the subtracted image.
    width = size(image,2); %Width of the subtracted image.
    ruler_width = 30;
    overlap = 5;
    x = (1:width-ruler_width+overlap)';
    u = 0;
    max_val = 0;
```

```
    degree = 10;
    buffer_percent = 0.15;
    buffer_range = 150;

    vec_height = row_avg*floor(height/row_avg);
    vec0 = zeros(height,1); %Gradient row vector of averaged
entire un-pixelated image
    vec1 = zeros(ceil(height/height_pixel_group_size)-1,1);
%Gradient row vector of averaged entire pixelated image
    vec2 = zeros(ceil(height/height_pixel_group_size)-1,1);
%Difference between n+1 and n values of vec1

    %% This section, discussed in §5.2, pixelates the whole image
into
    %% pixelated group of height and width defined above and
determines an
    %% intial estimation of the interface height (y_initial).
    for i = 1:height
        avg_inten = 0;
        for j = 1:width-ruler_width
            avg_inten = avg_inten + image(i,j);
        end
        vec0(i,1) = avg_inten/(width-ruler_width);
    end

    for i=1:width_pixel_group_size:width-ruler_width-1
        for j=1:height_pixel_group_size:height
            if ((height-j) >= height_pixel_group_size) &&
(((width-ruler_width)-i) >= width_pixel_group_size)       %A&B
                intensity = 0;

                for k=0:width_pixel_group_size-1
                    for l=0:height_pixel_group_size-1
                        intensity = intensity + image(j+l,i+k);
                    end
                end
                intensity =
intensity/(height_pixel_group_size*width_pixel_group_size);

                for k=0:width_pixel_group_size-1
                    for l=0:height_pixel_group_size-1
                        image(j+l,i+k) = intensity;
                    end
                end
            elseif ((height-j) >= height_pixel_group_size) &&
(((width-ruler_width)-i) < width_pixel_group_size)    %B
                intensity = 0;

                for k=0:width-ruler_width-i-1
                    for l=0:height_pixel_group_size-1
                        intensity = intensity + image(j+l,i+k);
                    end
                end
                intensity = intensity/((width-ruler_width-
i)*(height_pixel_group_size));
```

```
                for k=0:width-ruler_width-i-1
                    for l=0:height_pixel_group_size-1
                        image(j+l,i+k) = intensity;
                    end
                end
            elseif ((height-j) < height_pixel_group_size) &&
(((width-ruler_width)-i) >= width_pixel_group_size)    %A
                intensity = 0;

                for k=0:width_pixel_group_size-1
                    for l=0:height-j
                        intensity = intensity + image(j+l,i+k);
                    end
                end
                intensity =
intensity/((width_pixel_group_size)*(height-j+1));

                for k=0:width_pixel_group_size-1
                    for l=0:height-j
                        image(j+l,i+k) = intensity;
                    end
                end
            else
%!(A&B)
                intensity = 0;

                for k=0:width-ruler_width-i-1
                    for l=0:height-j
                        intensity = intensity + image(j+l,i+k);
                    end
                end
                intensity = intensity/((width-ruler_width-
i)*(height-j+1));

                for k=0:width-ruler_width-i-1
                    for l=0:height-j
                        image(j+l,i+k) = intensity;
                    end
                end
            end
        end
    end
%   figure; imshow(image); title('Pixelated Image'); %Displays
the pixelated image.

    for i = 1:floor(height/height_pixel_group_size)
        avg_inten = 0;
        for j = 1:floor((width-
ruler_width)/width_pixel_group_size)
            avg_inten = avg_inten +
image(i*height_pixel_group_size,j*width_pixel_group_size);
        end
        avg_inten = avg_inten/floor((width-
ruler_width)/width_pixel_group_size);
        vec1(i,1) = avg_inten;
```

```
    end


    for i = 1:row_avg:size(vec1,1)
        if (size(vec1,1)-i) >= (row_avg-1)
            avg_inten = 0;
            for j = 0:row_avg-1
                avg_inten = avg_inten + vec1(i+j,1);
            end
            avg_inten = (avg_inten/row_avg);
            for j = 0:row_avg-1
                vec1(i+j,1) = avg_inten;
            end
        elseif (size(vec1,1)-i) == 0
            vec1(i,1) = vec1(i,1);
        else
            avg_inten = 0;
            for j = 0:size(vec1,1)-i
                avg_inten = avg_inten + vec1(i+j,1);
            end
            avg_inten = (avg_inten/(size(vec1,1)-i));
            for j = 0:size(vec1,1)-i
                vec1(i+j,1) = avg_inten;
            end
        end
    end

    for i = 1:size(vec1,1)
        if i < size(vec1,1)
            vec2(i,1) = vec1(i,1) - vec1(i+1,1);
        else
            vec2(i,1) = 0;
        end
    end

    y_initial = ((find(vec2 == min(vec2)) -
1)*height_pixel_group_size); + 1; %Initial interface height
estimation.

    %% This section, discussed in §5.3, analyses the row-averaged
pixel
    %% intensity data and determines the final estimation for the
interface
    %% height (y_final).
    y_lower = y_initial - buffer_range;
    y_upper = y_initial + buffer_range;

    if y_lower < 1
        y_lower = 1;
    end
    if y_upper > height
        y_upper = height;
    end

    y_diff = y_upper - y_lower;
```

```
    vec3 = zeros(y_diff,1); % Weighted averages of vec1
    vec4 = zeros(y_diff-1,1); % Difference between n+1 and n
values of vec3

    weighted_below = 0.25;
    weighted_middle = 0.50;
    weighted_above = 0.25;

    for i = y_lower:y_upper
        if i == 1
            vec3(i-y_lower+1,1) = weighted_middle*vec0(i,1) +
weighted_above*vec0(i+1,1);
        elseif i == height
            vec3(i-y_lower+1,1) = vec3(i-y_lower,1);
        else
            vec3(i-y_lower+1,1) = weighted_below*vec0(i-1,1) +
weighted_middle*vec0(i,1) + weighted_above*vec0(i+1,1);
        end
    end

    for i = 1:size(vec3,1)-1
        vec4(i,1) = vec3(i+1,1) - vec3(i,1);
    end

    y = find(vec4 == max(vec4)) + y_lower - 1;

    z = (1:size(vec3,1))';
    z = z/max(z);
    yfit = polyval(polyfit(z,vec3,degree),z);

    fit_buffer = ceil(buffer_percent*size(yfit,1));

    vec4 = zeros(size(yfit,1),1);
    for i=1 + fit_buffer:size(yfit,1) - fit_buffer
        vec4(i,1) = yfit(i+1,1) - yfit(i,1);
    end

    vec5 = zeros(size(vec4,1),1);
    for i=1 + fit_buffer:size(vec4,1) - fit_buffer - 1
        vec5(i,1) = vec4(i+1,1) - vec4(i,1);
    end

    y_final = find(vec4 == max(vec4)) + y_lower; %Final interface
height estimation.

    %% This section is used for debugging purposes only.
    if debug
%         for i = 1:(width - ruler_width)  %Creates a white line
across the image for debug purposes
%             comp_image_rgb(y_final,i) = 1.5;
%         end
        directory = ['C:\Documents and
Settings\mroes\Desktop\Research\Pictures\', folder, '\Debug\'];
        if str2num(comparitive_image) < 10
           zpad = '00';
```

```
        elseif str2num(comparitive_image) < 100 &&
str2num(comparitive_image) >= 10
           zpad = '0';
        end
        image_string = [directory, 'Debug_', zpad,
comparitive_image, '.JPG'];
        imwrite(comp_image_rgb,image_string,'jpg')
        disp(['Debug: ', zpad, comparitive_image]);
        imshow(comp_image_rgb);
    end

    %% This section visually displays the estimated interface
height on the
    %% RGB (color) image, discussed in §5.3.
    if height_unit == 'cm'
        xls_details = xlsread([directory, 'Crop Values.xls']);
        y_height = rulervalue_top - (rulervalue_top -
rulervalue_bot)/xls_details(5)*y_final;
    elseif height_unit == 'px'
        y_height = y_final;
    else
        disp('Invalid height unit (cm|px)');
    end

    if display_plot == 'Y'
        fig1 = figure; hold on; title('Intensity Gradient');
        plot(z,vec3);
        plot(z,yfit,'r-')
        hold off;
        set(fig1,'Position', [25 screensize(4)-400 width+150
300])

        fig2 = figure; imshow(comp_image_rgb); hold on;
title('Interface Height');
        plot(x(:),y_initial,'g-');
        plot(x(:),y_final,'r-'); %Maximum 1st derivative.
        hold off
        set(fig2,'Position', [25 screensize(4)-585-height
width+150 height+100])
    end

end
```

D.3 Fissure permeability sub-routine

```
function k_f = DFPermeability()

    %% Global variables needed to solve equation 5.2 of §4.4.
    global M
    global vent_dia
    global nu
    global b
    global phi
    global W
    global lambda
    global txt
    global interval_time
    global rho_s
    global rho_a
    global g

    %% Attempts to determine fissure permeability
    fs=12;
    gprime = g*(rho_s - rho_a)/rho_a;

    %% This section applies a linear best fit and uses (5.2) of
§5.4 to
    %% solve for k_f/phi.
    m = Linear0Intercept(txt(:,3),txt(:,2));
    k_f = m/((M*pi*vent_dia^2.0*gprime)/(4*nu*b*W*lambda));
    figure; hold on
    yfit = m.*txt(:,3);
    plot(txt(:,3),txt(:,2),'b-');
    plot(txt(:,3),yfit,'r-');
    xlabel('Time (s)');
    ylabel('ln(h0+b/h+b)');
    titlestring = ['\rho_s = ', num2str(rho_s), ' g/ccm, \Deltat
= ', num2str(interval_time), ' sec, M = ', num2str(M)];
    title(titlestring);
    text(100,0.5,sprintf('kf/phi=%7.6f',k_f),'fontsize',fs)
    legend('Data', 'PolyFit','Location','Northwest');

    hold off
    fprintf('%12.10f',k_f)
end
```

Appendix E

Analytical details

The following section contains the analytical details that were omitted from §2 for the sake of brevity. Here, §E.1 contains the details for the line source whereas §E.2 is dedicated to the point source details.

E.1 Line source

The momentum equations (2.2) and (2.3) can be combined so as to eliminate the fluid pressure whence

$$\frac{\nu}{k}\left(\frac{\partial u}{\partial y}-\frac{\partial v}{\partial x}\right)=\frac{g}{\rho_a}\frac{\partial \rho}{\partial y}. \tag{E.1}$$

We now apply the boundary layer approximation (2.6) and introduce a stream-function ψ, defined so that

$$u=\frac{\partial \psi}{\partial y}\,, \qquad v=-\frac{\partial \psi}{\partial x}\,.$$

Equations (2.1) is then automatically satisfied whereas (E.1) and (2.4) become, respectively,

$$\frac{\partial^2 \psi}{\partial y^2} = \frac{g\beta k}{\nu}\frac{\partial S}{\partial y}, \tag{E.2}$$

and

$$\frac{\partial \psi}{\partial y}\frac{\partial S}{\partial x} - \frac{\partial \psi}{\partial x}\frac{\partial S}{\partial y} = D\phi\,\frac{\partial^2 S}{\partial y^2}. \tag{E.3}$$

We look for a self-similar solution to (E.2) and (E.3) of the form

$$\psi = A^* x^{1/3} f(\eta), \qquad S = \frac{B^*}{x^{1/3}} f'(\eta)\,, \tag{E.4}$$

Where the prime indicates differentiation with respect to η, which is itself defined by

$$\eta = \frac{y}{x^{2/3}}\left[\frac{F_o k}{(D\phi)^2 \Lambda \nu}\right]^{1/3},$$

The constants A^* and B^* are determined shortly.

Applying (E.4) and (E.2) allows us, after some algebra, to write B^* in terms of A^*, i.e.

$$B^* = \frac{A^* \nu}{g\beta k}\left[\frac{F_o k}{(D\phi)^2 \Lambda \nu}\right]^{1/3}. \tag{E.5}$$

Meanwhile, applying (E.4) in (E.3) yields,

$$\left(\frac{D\phi F_o k}{\Lambda \nu}\right)^{1/3} f''' + \frac{1}{3} A^* (f f')' = 0\,. \tag{E.6}$$

This result motivates us to define A^* as

$$A^* = \left(\frac{D\phi F_o k}{\Lambda \nu}\right)^{1/3} \quad \rightarrow \quad B^* = \frac{1}{g\beta}\left(\frac{F_o^2 \nu}{\Lambda^2 D\phi k}\right)^{1/3}, \tag{E.7}$$

where (E.5) has been applied. Integrating (E.6) recognizing that f' must vanish in the far-field where $S = 0$ yields

$$f' = \frac{1}{6}(c^2 - f^2)\,, \tag{E.8}$$

which has as its solution

$$f = c\tanh\left(\frac{1}{6}c\eta\right). \tag{E.9}$$

The constant of integration, c, is determined by recalling that the buoyancy flux, F_o, is independent of the vertical coordinate, x, provided the ambient is unstratified. In mathematical terms,

$$F_o = \Lambda \int_{-\infty}^{\infty} ug'dy\,, \tag{E.10}$$

where the integrand is evaluated at arbitrary x. Here the reduced gravity is defined by

$$g' = g\left(\frac{\rho - \rho_a}{\rho_a}\right) = g\beta S\,, \tag{E.11}$$

the latter equality following from the equation of state (2.5). Applying this definition in (E.10) and recalling that $u = \partial\psi/\partial y$ yields, after some helpful cancellation of terms, $c = (9/2)^{1/3}$. With the solution (E.9) now unambiguously specified, the plume volume flux can be straightforwardly determined from

$$Q = \Lambda \int_{-\infty}^{\infty} udy = \Lambda[\psi]_{-\infty}^{\infty}\,, \tag{E.12}$$

where ψ is given in terms of f by (E.4a). Applying the previous results yields (2.7) from which (2.8) follows.

E.2 Point source

Whereas Appendix E.1 considered a plume issuing from a line source, we now study the axisymmetric flow that results from flow stemming from a point source. In this case, it is helpful to introduce a Stokes stream-function, ψ_s, defined as

$$u_r = -\frac{1}{r}\frac{\partial \psi_s}{\partial x}, \qquad u_x = \frac{1}{r}\frac{\partial \psi_s}{\partial r},$$

where r and u_r denote, respectively, the radial coordinate and velocity. Equations (E.2) and (E.3) are then expressed as

$$\frac{\partial}{\partial r}\left(\frac{1}{r}\frac{\partial \psi_s}{\partial r}\right) = \frac{g\beta k}{\nu}\frac{\partial S}{\partial r}, \tag{E.13}$$

and

$$\frac{1}{r}\frac{\partial \psi_s}{\partial r}\frac{\partial S}{\partial x} - \frac{1}{r}\frac{\partial \psi_s}{\partial x}\frac{\partial S}{\partial r} = \frac{D\phi}{r}\frac{\partial}{\partial r}\left(r\frac{\partial S}{\partial r}\right). \tag{E.14}$$

respectively. Just as before, a self-similar solution is sought, now of the form

$$\psi_s = \check{A}xF(\eta), \qquad S = \frac{\check{B}}{x}G(\eta), \tag{E.15}$$

where

$$\eta = \frac{r}{D\phi x}\sqrt{\frac{F_o k}{2\pi\nu}},$$

(c.f. equations 7.5.24 and 7.5.25 of Phillips 1991). Applying these results in (E.12) yields

$$G = \frac{1}{\eta}F', \tag{E.16}$$

provided $\check{B}$ is defined so that

$$\check{B} = \frac{F_o \check{A}}{2\pi g\beta (D\phi)^2}. \tag{E.17}$$

Meanwhile, (E.13) can be reduced to

$$-F'(G\eta)' - G'(F - F'\eta) = \frac{D\phi}{\check{A}}(G'\eta)', \tag{E.18}$$

which motives us to set $\check{A} = D\phi$. Having done so, analytical solutions of (E.15) and (E.17) may be readily derived whereby

$$\psi_s = \frac{3D\phi x\eta^2}{8 + \frac{3}{4}\eta^2}, \qquad S = \frac{3F_o}{8\pi g\beta D\phi x\left(1 + \frac{3}{32}\eta^2\right)^2}. \tag{E.19}$$

Consistent with the earlier discussion, the numerical values of parameters in the previous expressions are determined by requiring that the buoyancy flux, defined as

$$F = 2\pi \int_0^\infty ug'rdrd\theta, \tag{E.20}$$

is independent of the vertical coordinate, i.e. $F = F_o$ for all x. Thereafter, the plume volume flux can be straightforwardly computed from

$$Q = 2\pi \int_0^\infty urdr\,. \tag{E.21}$$

In this way, (3.1) may be derived.